AFRL-RI-RS-TR-2009-180
Final Technical Report
July 2009

QUANTUM LIDAR - REMOTE SENSING AT THE ULTIMATE LIMIT

Louisiana State University Baton Rouge

Sponsored by
Defense Advanced Research Projects Agency
DARPA Order No. AJ11/00

AIR FORCE RESEARCH LABORATORY
INFORMATION DIRECTORATE
ROME RESEARCH SITE
ROME, NEW YORK

NOTICE AND SIGNATURE PAGE

Using Government drawings, specifications, or other data included in this document for any purpose other than Government procurement does not in any way obligate the U.S. Government. The fact that the Government formulated or supplied the drawings, specifications, or other data does not license the holder or any other person or corporation; or convey any rights or permission to manufacture, use, or sell any patented invention that may relate to them.

This report was cleared for public release by the 88th ABW, Wright-Patterson AFB Public Affairs Office and is available to the general public, including foreign nationals. Copies may be obtained from the Defense Technical Information Center (DTIC) (http://www.dtic.mil).

AFRL-RI-RS-TR-2009-180 HAS BEEN REVIEWED AND IS APPROVED FOR PUBLICATION IN ACCORDANCE WITH ASSIGNED DISTRIBUTION STATEMENT.

FOR THE DIRECTOR:

/s/
DONALD J. NICHOLSON
Work Unit Manager

/s/
EDWARD J. JONES, Deputy Chief
Advanced Computing Division
Information Directorate

This report is published in the interest of scientific and technical information exchange, and its publication does not constitute the Government's approval or disapproval of its ideas or findings.

REPORT DOCUMENTATION PAGE

Form Approved
OMB No. 0704-0188

1. REPORT DATE *(DD-MM-YYYY)*	2. REPORT TYPE	3. DATES COVERED *(From - To)*
JULY 2009	Final	July 2007 – December 2008

4. TITLE AND SUBTITLE

QUANTUM LIDAR – REMOTE SENSING AT THE ULTIMATE LIMIT

5a. CONTRACT NUMBER
N/A

5b. GRANT NUMBER
FA8750-07-2-0214

5c. PROGRAM ELEMENT NUMBER
61101E

6. AUTHOR(S)

Jonathan P. Dowling

5d. PROJECT NUMBER
AJ11

5e. TASK NUMBER
QU

5f. WORK UNIT NUMBER
LI

7. PERFORMING ORGANIZATION NAME(S) AND ADDRESS(ES)
Louisiana State University Baton Rouge
Hearne Institute for Theoretical Physics
Department of Physics and Astronomy
202 Nicholson Hall, Tower Drive
Baton Rouge, LA 70803

8. PERFORMING ORGANIZATION REPORT NUMBER
N/A

9. SPONSORING/MONITORING AGENCY NAME(S) AND ADDRESS(ES)

DARPA
3701 North Fairfax Drive
Arlington, VA 22203-1714

AFRL/RITC
525 Brooks Rd.
Rome NY 13441-4505

10. SPONSOR/MONITOR'S ACRONYM(S)
N/A

11. SPONSORING/MONITORING AGENCY REPORT NUMBER
AFRL-RI-RS-TR-2009-180

12. DISTRIBUTION AVAILABILITY STATEMENT
APPROVED FOR PUBLIC RELEASE; DISTRIBUTION UNLIMITED. PA# 88ABW-2009-3282 Date Cleared: 18-July-2009

13. SUPPLEMENTARY NOTES

14. ABSTRACT
The Louisiana State University (LSU) led team carried out an exhaustive study of a two-mode quantum optical sensor. The classical baseline of comparison was a standard two-mode coherent Light Detection and Ranging (LIDAR) system. The LSU quantum LIDAR system has many of the same features of the classical system, with the critical exception that the photon source and detection scheme were treated quantum mechanically and the complete analysis of loss was carried out in a quantum optical setting. A critical deliverable or our Phase I also is to provide a complete quantum theory and analysis of the performance of what is typically known as classical coherent LIDAR. A crucial point to realize here is that there is no such thing as classical LIDAR. The standard laser beam used in classical LIDAR is a quantum coherent state of light whose properties set the limits to resolution and sensitivity. Hence the classical baseline is in fact a quantum baseline, in this sense.

15. SUBJECT TERMS
Remote Sensing; Lidar; Radar; Synthetic Aperture Radar (Sar); Sensors Using Photons In A Non-Classical State; Eg Squeezed, Entangled

16. SECURITY CLASSIFICATION OF:			17. LIMITATION OF ABSTRACT	18. NUMBER OF PAGES	19a. NAME OF RESPONSIBLE PERSON
					Donald J. Nicholson
a. REPORT	b. ABSTRACT	c. THIS PAGE			19b. TELEPHONE NUMBER (*Include area code*)
U	U	U	UU	97	N/A

TABLE OF CONTENTS

LIST OF FIGURES

1.0 EXECUTIVE SUMMARY

1.1 Technical

During the 18-month period of performance, the Louisiana State University (LSU) led team carried out an exhaustive study of a two-mode quantum optical sensor. The classical baseline of comparison was a standard two-mode coherent Light Detection and Ranging (LIDAR) system, shown schematically in Fig.2. The LSU quantum LIDAR system, indicated in Fig.1, has many of the same features of the classical system, with the critical exception that the photon source and detection scheme were treated quantum mechanically and the complete analysis of loss was carried out in a quantum optical setting. A critical deliverable or our Phase I also is to provide a complete quantum theory and analysis of the performance of what is typically known as classical coherent LIDAR. A crucial point to realize here is that there is no such thing as classical LIDAR. The standard laser beam used in classical LIDAR is a quantum coherent state of light whose properties set the limits to resolution and sensitivity. Hence the classical baseline is in fact a quantum baseline, in this sense.

It is the conclusion of our Phase I study that a quantum coherent LIDAR system, coupled with a number-resolving detection scheme, meets all the criteria and metrics for a successful Phase I study. As we will detail below, the primary result is that such a combination of a coherent quantum state propagation, plus number resolving detection, supports a ten-fold improvement of resolution of the target with no worse than the equivalent classical sensitivity (shot-noise) of a traditional classical coherent LIDAR.

The primary conclusion is that by using a coherent state of light in an active sensor, which is as classical as you can get, we avoid the super-Beer's law absorption effect which has been show to rapidly degrade super-resolving quantum entangled states of light as they propagate through absorbing and scattering media. The trick is to employ a novel quantum detection scheme, using newly available number-resolving detectors, to extract far more information from the coherent state than is possible with simple "classical" homodyne detection schemes. Essentially a two-mode coherent state contains super-resolution information, which if properly extracted, can be used to provide sub-Rayleigh resolution with sensitivity no worse than shot noise.

We summarize our results against the Defense Advanced Research Projects Agency (DARPA) Quantum Sensors Program (QSP) requirements:

The following conditions must be simultaneously satisfied:

1) The photons' interaction with a target doesn't cause the non-classical state to be entirely lost.

The primary conclusion of our Phase I is that a coherent state is in fact non-classical and this non-classicality can be exploited in the detection process. However, since the coherent state is "as classical as you can get" the photon interaction with the target follows typically coherent state rules for attenuation and scattering. That is a coherent state becomes another coherent state of smaller amplitude but of the same *photon number* statistics.

2) The quantum sensor can resolve two targets at a closer spacing than is possible with a classical sensor.

This is accomplished, as we shall outline below, by extracting the N00N and higher-order components of the two-mode coherent state and extracting the sub-classical resolution in the number resolving detection process. A proper post-processing of the phase information in the photon number basis allows us to beat the classical Rayleigh diffraction limit by a factor of ten.

3) The energy that travels between the quantum sensor and the target propagates at the single-photon wavelength.

This is accomplished in our modeling by assuming coherent states propagating at approximately the 1.5 micron wavelength, a water vapor window in the atmosphere, and then by extracting the $N = 10$ N00N components and higher to get an effective resolution of 150 nanometers (vacuum ultraviolet).

4) The quantum sensor suffers a loss of sensitivity and resolution that is no worse than the loss suffered by a classical sensor under all of the following conditions:

a. The transmission medium between the sensor and the target absorbs or diffusely scatters photons.

b. The target is in a 300K (Radio Frequency (RF) sensors) or daylight (optical sensors) environment.

c. The target absorbs some incident photons.

d. The target scatters incident photons non-uniformly over 4π steradians.

These are all accomplished by propagating coherent states of light, which are the states used in classical sensors, and then by extracting super-resolution only at the end in the detection process in the number basis. Hence by definition, the propagation of the light in our quantum sensor exactly matches the properties of an ordinary sensor. By counting all photons at the detector we ensure super-quantum-resolution at no worse than classical shot-noise sensitivity.

The Phase I Program Metrics defining a successful Phase I are as follows:

1. The quantum sensor concept has been shown to simultaneously satisfy all of the four conditions listed above.

2. The quantum sensor concept has been shown to support at least a 10x improvement in resolution over the Rayleigh limit in the presence of 3 dB of transmission medium loss with a signal to noise ratio (SNR) of 26 dB.

Our Phase I works support successful progress against both Phase I metrics, as outlined above, and detailed below. Again the key point is that a coherent state LIDAR system, which transmits "classical" states through the atmosphere can meet all the DARPA requirements, provided it is augmented with a quantum number resolving detection scheme. Processing the photon number in detection allows for ten-fold super resolution, and processing all the photons in detection allows for no worse than the classical shot noise of the equivalent classical sensor. The primary idea is that there is super-resolution resolution available in a number-resolving quantum detection scheme that is not available in the typical, classical, intensity measurement scheme employed in classical coherent LIDAR, even when classical coherent states are propagated through the atmosphere. The super-resolving scheme is able to discriminate against a background with over 40dB SNR, as we shall prove below.

1.2 Administrative

This work was carried out by Jonathan P. Dowling (professor), Hwang Lee (assistant professor), Tae-Woo Lee (research staff), Christoph Wildfeuer (postdoc) and Sean Huver (graduate student), at Louisiana State University (LSU), as well as by Ulvi Yurtsever (principal scientist) at MathSense Analytics (MSA) and Steven Wilkinson (senior program manager) at Raytheon Corporation. The original proposal contained a subcontract with the National Aeronautics and Space Administration (NASA) Jet Propulsion Laboratory (JPL) that proved contractually untenable. This JPL work was recontracted through an addendum to the original proposal to Dr. Tae-Woo Lee (research staff) at the LSU Center for Computation and Technology (CCT). Unfunded collaborators included Prof. Georgios Veronis (associate professor) at the Electrical and Computer Engineering (ECE) Department of LSU and Dr. Dmitry Uskov (research staff) at the Physics Department of Tulane University. Deliverables include a number of scientific preprints and reprints that are attached in the Appendix of this report. The work was completed on schedule, as the rate charged by Dr. T.W. Lee was increased so his project would end simultaneously with all the others on 31DEC08. At this time we are still awaiting one final invoice from Raytheon Corporation, and also are processing some final travel paperwork. We are on time and anticipate being on budget.

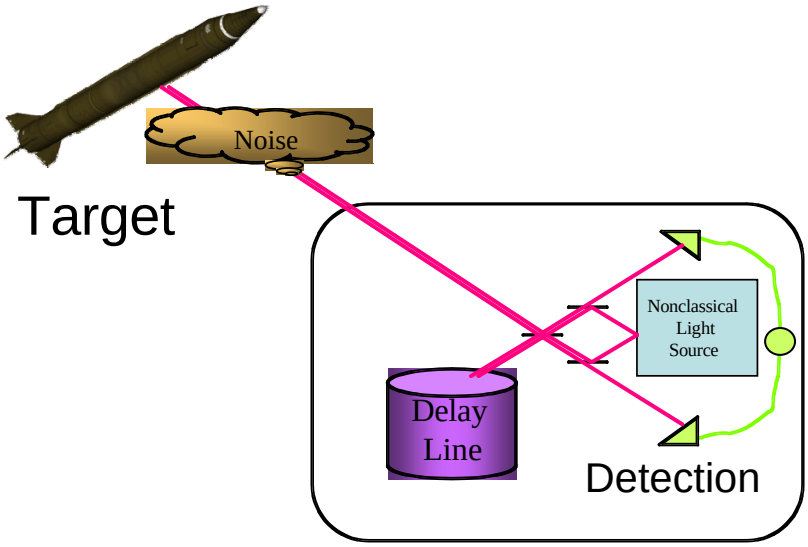

Figure 1: LSU Quantum LIDAR Concept

2.0 INTRODUCTION

2.1 Overview and Summary

In a classical coherent LIDAR system, Fig.2, the optical radiation propagates at the single photon wavelength, the resolution is typically the Rayleigh limit of $\lambda/2$, and the phase sensitivity is given by the shotnoise $\Delta\varphi = 1/\sqrt{\bar{n}}$, where $\bar{n}$ is the mean number of photons that is proportional to the intensity [Dowling2008]. It is this restriction to the Rayleigh resolution that we will overcome with a quantum approach. It is typical in such a classical coherent LIDAR scheme to perform difference intensity detection, as indicated in Fig.2. For such a scheme the relevant expectation of the appropriate quantum operator gives,

$$M(\varphi) \equiv I_D - I_C = I_A \cos(\varphi). \tag{1}$$

Since $\varphi/2 = kx/2 = \pi x/\lambda$, we can solve to get $\Delta x = \lambda/2$ for the peak-to-peak spacing, which is the Rayleigh limit. Simple linear error propagation theory then gives the shot-noise sensitivity [Gerry2005],

$$\Delta\varphi_{\mathrm{SNL}} = \frac{\Delta M}{\partial M / \partial \varphi} = \frac{\Delta M}{\sqrt{I_A}} \propto \frac{1}{\sqrt{\bar{n}}}. \tag{2}$$

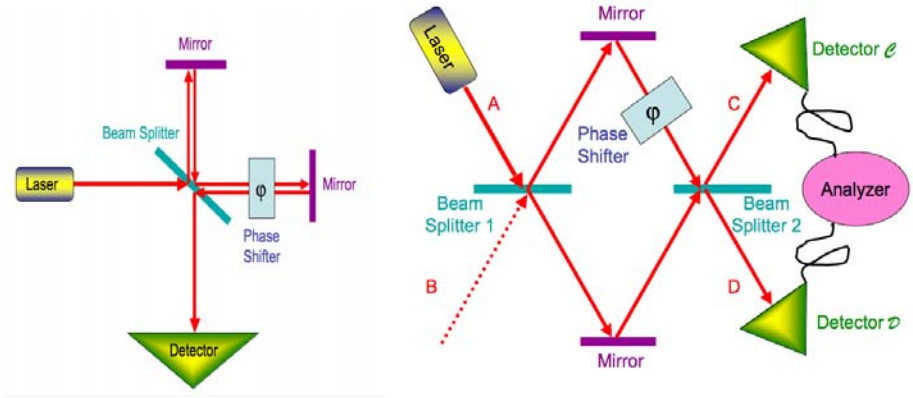

Figure 2: Classical Michelson and Mach-Zehnder Interferometer

To again clarify the terminology, which is now standard in quantum metrology, *quantum super-resolution* is defined as an interference period shorter than 2π in Eq.1 and *quantum super-sensitivity* is defined as a scaling law that beats the shot-noise limit scaling with intensity of Eq.2. The origin of the relation between intensity uncertainty and phase uncertainty is quantum mechanical in nature [Gerry2005, Dowling2008], but can be illustrated simply in Fig.3.

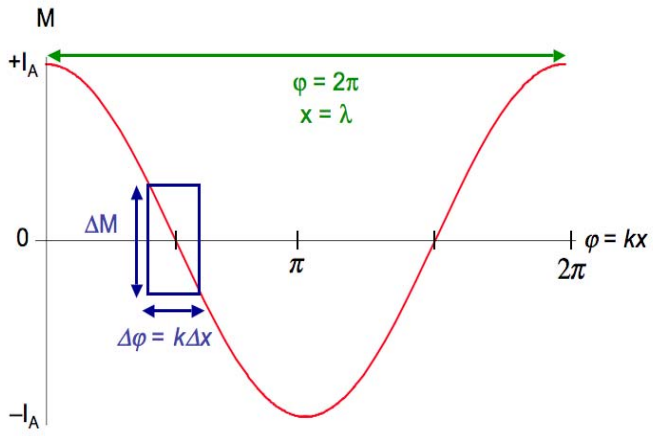

Figure 3: Classical Interferogram

Our team initiated the concept of quantum remote sensing with a paper in 2000, indicating theoretically that the classical Rayleigh diffraction limit in resolution could be beaten by exploiting entangled photons [Boto2000, Kok2001]. This effect is now universally known as quantum super-resolution. We also pointed out in subsequent papers that a similar strategy could beat the classical shotnoise limit to sensitivity, in what is known as quantum super-sensitivity [Lee2002, Kok2002, Lee2002, Kok2004, Dowling2008]. Base on our ideas, the concept of super-resolution was demonstrated in a series of experiments [Mitchell2004, Walther2004, Sun2006, Resch2007, Kawabe2007, Sciarrino2008, Liu2008]. Super-sensitivity has also now been demonstrated as well [Nagata2007, Okamoto2008, Higgens2007]. Most of these strategies invoked the production and measurement of the so-called N00N states, also invented by our team, which have the form,

$$\left|N::0\right\rangle_{AB}^{\varphi} \equiv \left|N\right\rangle_A\left|0\right\rangle_B + e^{iN\varphi}\left|0\right\rangle_A\left|N\right\rangle_B, \qquad (3)$$

where *A* and *B* refer to the two optical modes in Fig.4, the *N* is the number of photons in the state, and φ is the phase shift to be measured, that is proportional to the arm path-length difference.

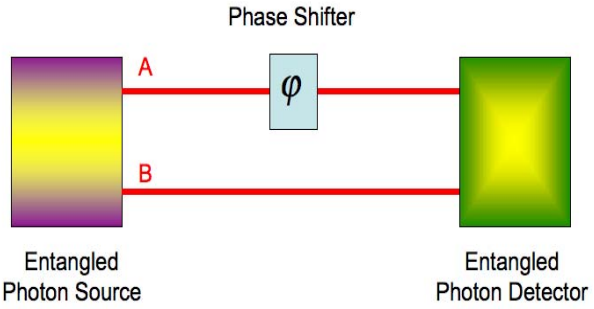

Figure 4: Schematic of Quantum Sensor Model

We can see in Eq.3 that according to the phase factor of $N\varphi$ that the phase difference between the two arms of the interferometer oscillates with a period that is N times faster than the classical interference pattern of Eq.1, as shown in Fig.5. In the absence of photon loss, a suitable number counting detection scheme produces an interference prediction of [Dowling2008],

$$M_{\mathrm{NOON}}(\varphi) = I_A \cos(N\varphi), \tag{4}$$

where the N-fold improvement in oscillation period is apparent in Eq.4 when compared to Eq.1. For $N = 10$, there is a 10-fold improvement in quantum super-resolution, which automatically meets QSP resolution improvement metric, *in the absence of loss.* The higher frequency oscillations are also the origin of the improved quantum super-sensitivity. Consider Fig.5 where we show the oscillations of the classical interferometer against those of the N00N interferometer, for the case of $N = 4$.

In Fig.5 it is apparent that the N00N-state interferogram has a slope that is N-times steeper than the classical curve. Hence it is much easier to tell if the green fringe moves compared to the red curve, indicating a reduced phase uncertainty $\Delta\varphi$. Note this comes about at a result of increased intensity uncertainty ΔM, in accordance with the quantum number-phase Heisenberg uncertainty principle [Dowling2008]. A rigorous analysis, including the effects of counting the photons N at a time in the quantum interferometer, indicates an over all improvement of,

$$\Delta\varphi_{\mathrm{N00N}} = \frac{\Delta M_{N00N}}{\partial M / \partial\varphi} = \frac{\Delta M_{N00N}}{I_A} \propto \frac{1}{N}, \tag{5}$$

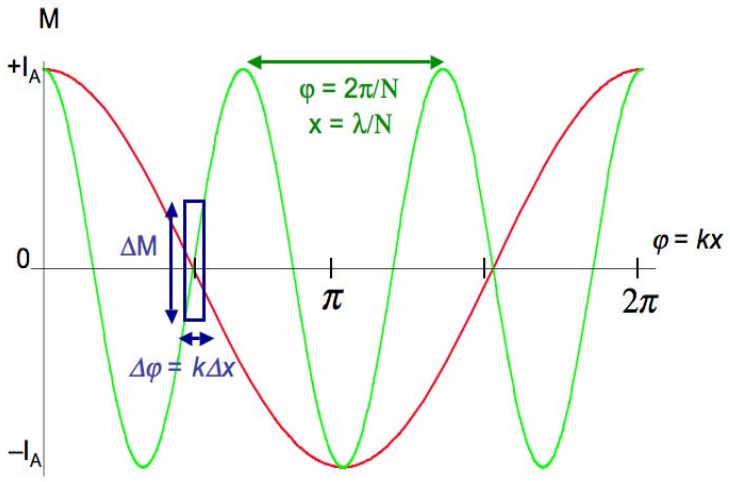

Figure 5: Classical Interferogram (Red) Versus the Quantum Interferogram (Green) for a N00N State with N = 4

Note this is a quadratic improvement over the shot-noise limit (SNL) of the classical interferometer, Eq.2. The N00N state actually saturates the Heisenberg uncertainty principle, in the determination of local phase measurement [Durkin2007], and hence this *1/N* behavior is called the Heisenberg limit (HL). Our team now has interlocking numerical and analytic proofs that the N00N-state approach is optimal for achieving super-resolution and local super-sensitivity *in the absence of loss.* Hence the N00N state interferometer serves as an important benchmark in any modeling of an interferometric sensor scheme in that: (1) it serves as a starting point for quantum states to test for super-resolution; and (2) any new theory or numerical approach that includes loss must recover the N00N result when the loss is turned off. Let us recall that the QSP metrics state we are to achieve ten-fold resolution with no worse than classical sensitivity. Hence, it the conclusion of our Phase I that ten-fold super-resolution is possible with no worse than the SNL in signal to noise, and we will outline how we achieve this below.

It is now well known that the N00N state approach degrades extremely rapidly in the presence of photon loss, a fact that is easy to calculate, and which we now refer to as super-Beer's law [Rubin2007, Gilbert2008a, Gilbert2008b]. What is trickier to understand is why N00N states perform so poorly, which we have done as part of this Phase I [Huver2008]. For this work we define photon loss to include photons, which are absorbed or scattered out of the modes of interest but otherwise do not reach the detector. In fact, as we shall see, we model absorption loss by using beam splitters to randomly scatter out photons from the modes of interest, which we prove in Sec.9.0, below, reproduces Beer's law for classical, linear loss. We now understand that the N00N susceptibility and consequent super-Beer's law is a consequence of the which-path information available to the environment. Hence, we were able to mitigate (somewhat) the effects of photon loss by erasing the which-path information using the M&M states [Huver2008]. Our computer optimization confirms that N00N states are optimal for zero loss and M&M states are optimal for low loss, say 3dB to 6dB. For the high loss regime of concern to the DARPA QSP program, our analytical and numerical results have converged on a QSP Type-II sensor approach, which transmits classical coherent states through the atmosphere to the target, but then extracts super-resolution in the number basis in the detection using number resolving detectors.

First let us see why N00N states are so susceptible to loss. Consider Fig.6 where we show the interferogram for a coherent state (red) and a N00N state (green) in the presence of 3dB of loss. While super-resolution is still apparent in the N00N state curve, the visibility of the N00N state degrades like $exp(-N\beta L)$ as a function of distance L, absorption coefficient β, and photon number N. This is to be compared to the "classical" or coherent state, which degrades only like $exp(-\beta L)$. Hence the N00N state obeys a *super-exponential decay law or super-Beer's law.*

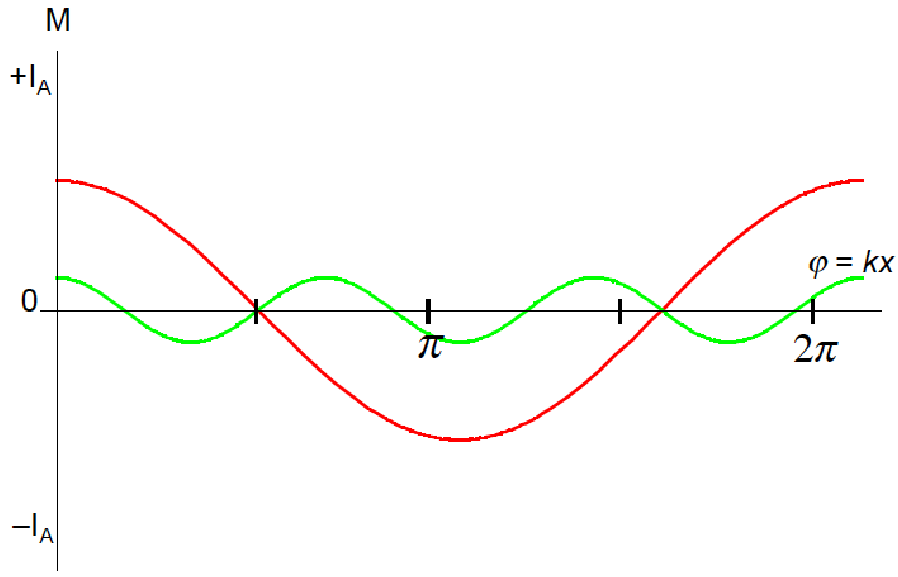

Figure 6: The Interferogram of a Classical Coherent State (Red) Against an N = 4 N00N State in the Presence of 3dB Total Loss

While the N00N state still shows super-resolution in the presence of loss, the sensitivity, which depends on the maximum slope of the curve via Eq.5, can be see to be equal to that of the classical coherent state for this loss. Hence while still super-resolving, the N00N state quickly losses its super-sensitivity, which is its ability to beat the shot-noise limit. For sufficiently high loss the N00N state actually has worse than shot-noise sensitivity, as the slope of the curve becomes very small compared to the coherent state [Rubin2007, Gilbert2008a, Gilbert2008b, Huver2008]. The graphic gives a simple intuitive means of understanding this effect.

In our recent work, supported by this grant, we not only confirmed that N00N states do poorly in the presence of loss but also have developed an simple means to understand why they do so bad. As outlined below in the Appendix [Huver2008], we can understand that the zero component of a N00N state provides complete which-path information to the environment. Hence the effects of loss can be mitigated (somewhat) by replacing N00N states with the so-called M&M states of the form

$$\left|M :: M'\right\rangle_{AB}^{\varphi} \equiv \left|M\right\rangle_A \left|M'\right\rangle_B + e^{i(M-M')\varphi} \left|M'\right\rangle_A \left|M\right\rangle_B, \qquad (6)$$

where $N = M - M'$ is the super-resolving factor, as before, but now the state no longer hits the Heisenberg limit (HL) in sensitivity, but rather is between the SNL and HL in the absence of loss, as discussed below. Nevertheless for loss in the range of 3dB to about 6dB this state outperforms the N00N state in terms of super-resolution and super-sensitivity. The idea is that by putting some extra photons where only vacuum was before we erase the which-path information available to the environment, and mitigate the effects of loss, somewhat. However the M&M state still suffers from a super-Beer decay law and for the large loss regime, greater than 6dB, this scheme also begins to degrade rapidly.

As we proposed, and we discuss in detail in Secs. 6.0 and 7.0 below, we have developed a detailed computational modeling framework for the design and optimization of a simple two-mode quantum sensor with loss. This code recovers our analytical results in the low-loss regime. That is the code finds the optimal state in the 0dB–3dB range is the N00N state, and in the 3dB–6dB range the M&M state. What is of most interest to our successful Phase I is the result that the code always finds that a two-mode coherent state, coupled with a sum of number-resolving-detectors scheme, always is optimal in the high loss regime of greater than about 6dB. Such a scheme can provide ten-fold improvement in resolution with no worse than shot-noise sensitivity in comparison to a classical scheme using coherent light and ordinary intensity difference detection. The super-resolution comes about from the ability of number resolving detectors to extract the high-frequency oscillations of the individual number components of the two-mode coherent state. The loss is no worse than ordinary Beer's law, as ordinary coherent classical states propagate to the target and through the delay line. No worse than the SNL in sensitivity is achieved by counting all the available photons. It is then our primary result that a classical coherent LIDAR system can be made into a simple quantum super-resolving sensor by simply replacing the classical intensity detection scheme with a quantum number-resolving scheme. As number-resolving detectors have been recently developed, primarily in the context of their use in linear optical quantum computing [Kok2007], we assert that a quantum sensor can be made from a classical one simply by altering the detection scheme. Our approach should be compared a competing approach, where also classical coherent light is propagated, but the detection scheme mixes the coherent light with squeezed light in homodyne detection to get super resolution. The number basis is quantum conjugate to the phase basis, and it is well known that phase information in the phase basis can be translated into the number basis by a rotation in the SU(2) group that is carried out by a simple 50:50 beam splitter [Yurke1986]. Hence our approach

can be viewed as complementary to that of the squeezed-state approach, but like the squeezed-states approach all the action takes place in the quantum detection scheme, putting our scheme squarely in the QSP Type-II sensor domain — only classical coherent light is propagated to the target. Let us see how this all works.

The classical two mode coherent state inside the classical coherent baseline LIDAR interferometer can be written in the photon number basis as,

$$|\alpha\rangle_{AB} = \left|\alpha/\sqrt{2}\right\rangle_A \left|\alpha/\sqrt{2}\right\rangle_B = e^{-\bar{n}/2} \sum_{n=0}^{\infty}\sum_{m=0}^{\infty} \frac{\left(\alpha/\sqrt{2}\right)^{n+m}}{\sqrt{n!m!}} |n\rangle_A |m\rangle_B , \tag{7}$$

where $\bar{n} = |\alpha|^2$ is the mean photon number proportional to the total intensity [Dowling2008]. What is remarkable is that even though each number component obeys a super-Beer decay law, these all cancel out in the sum, uniquely for the coherent state, so that we have in the case of equal loss βL in both arms,

$$\left|\alpha/\sqrt{2}\right\rangle_A \left|\alpha/\sqrt{2}\right\rangle_B \rightarrow \left|e^{-\beta L}\alpha/\sqrt{2}\right\rangle_A \left|e^{-\beta L}\alpha/\sqrt{2}\right\rangle_B , \tag{8}$$

which is the standard loss model of ordinary Beer's law for coherent LIDAR. Here it is critical to note that this Beer's law is not only a property of the state but also of the number-insensitive detection scheme shown in Fig.2. This leads us to our primary observation. The dual coherent state in Eq.7 contains highly oscillating super-resolving terms, which all tend to average out in a number-insensitive detection scheme. *Hence, by moving to a number-resolving detection scheme, we can exploit the higher harmonics in Eq. 7 and attain super-resolution, while suffering no worse than the classical Beer's law in loss.* This is essentially the experimental and theory result of the recent experiment by Andrew White's group at the University of Queensland, where six-fold super-resolution was observed using only classical light but exploiting a number resolving detection scheme [Resch2007]. A similar experiment using a Fabry-Perot interferometer, number resolving detectors, and classical coherent light was recently observed by our team in collaboration with the laboratory of Alan Migdall at National Institute of Standards and Technology (NIST) [Wildfeuer2008]. These results are discussed in detail below in Sec.8.0.

To see how the state of Eq.7 contains terms of ten-fold improved resolution, let us consider a simple detection operator, which is known to be optimal in the absence of loss with the use of N00N states [Kok2004],

$$O_{AB}^{N00N} = |0\rangle_A |N\rangle_B \langle N|_B \langle 0|_A + |N\rangle_A |0\rangle_B \langle 0|_B \langle N|_A , \tag{9}$$

which can be implemented with a number-resolving detector that detects only the photon number $n = N$. This so-called 0NN0-N00N operator picks out the N00N component of any two mode state. We take the expectation of this operator against the two-mode coherent state in Eq.7 to get,

$$M_N^{\bar{n}}(\varphi) = \bar{n}^N e^{-\bar{n}} \cos(N\varphi)/N! \qquad (10)$$

We see immediately that the quantum number resolving 0NN0-N00N operator picks out a super-resolving component of the dual-mode coherent state. Here we note $\alpha = e^{i\varphi}\sqrt{\bar{n}}$, where φ is the phase to be detected. We also have not yet included the effects of loss, which would produce an additional factor of $e^{-\beta L}$, which is the ordinary Beer's law factor, and can be included easily by *redefining* $\bar{n}$ *to be the normalized intensity at the detector rather than at the transmitter.* Hence, for example, if *N = 10,* then a ten-number resolving detector picks out only the ten-fold improved resolving component, which is the QSP metric for resolution. However, the naive scheme of Eq.10 is not super sensitive, and in fact has a sensitivity that is worse than shot noise, due to the degradation of the fringe visibility by the factor of $\bar{n}^N e^{-\bar{n}} N!$ This factor is plotted in Fig.7 below.

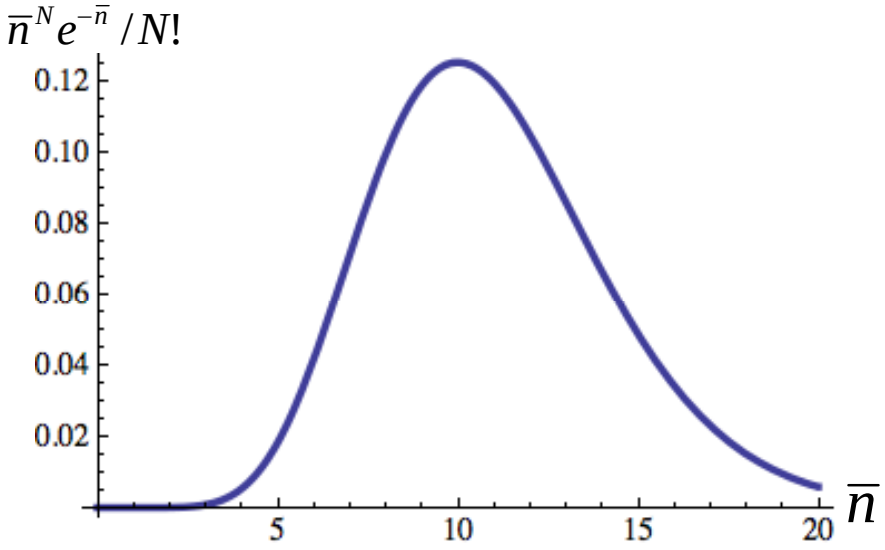

Figure 7: The Two Mode Coherent State Projected onto the N00N Basis Has a Weight Factor Of $\bar{n}^N e^{-\bar{n}}/N!$ for N = 10

We note that this function peaks at $\bar{n} = 10$, which suggests a strategy by which we adjust the initial amplitude of the coherent state such that the return intensity, now defined to be $\bar{n}$, has this value after loss so that the primary contribution is the ten-fold super-resolving term. The properly normalized N00N component expectation of Eq.10 is plotted in Fig.8 below, for $\bar{n} = N = 10$, as a function of the phase. It has a visibility of only 12% compared to the classical difference counting scheme shown in red in Fig.5. *However it has the desired ten-fold improved super resolution!* A simple calculation shows that the sensitivity is worse than the SNL for the equivalent coherent state, simply due to the fact that the single *N = 10,* 0NN0-N00N detection scheme of Eq.9, throws away too many photons by counting only the *N = 10* events.

As mentioned above, this naive approach of selecting only the N=10 term is too crude to give both ten-fold super-resolution and *no worse than* the SNL for an equivalent classical scheme (where intensity difference is used upon detection instead of 0NN0-N00N). This poor performance is due to the fact that a quantum detection scheme, which only counts $N = 10$, throws away too many photons, compared to the classical detection scheme, which keeps all of them. The quantum 0NN0-N00N scheme is optimal for a N00N state but clearly is not optimal for this dual coherent state protocol. Even if we optimize to $\bar{n} = 10$ in the return pulse, we have a Poisson distribution of coherent-state pulses that will contain many states with more or less than ten photons and will not be counted. Hence a smarter strategy is needed to attain both ten-fold super resolution and no worse than SNL sensitivity of the equivalent classical scheme, as required by the primary QSP metric.

Such as scheme is suggested by our computer optimization results, detailed in Secs. 6.0 and 7.0, below, which indicate a dual mode coherent state combined with a sum of number-resolving detections (NRD) provides the optimal phase information in the presence of large loss.

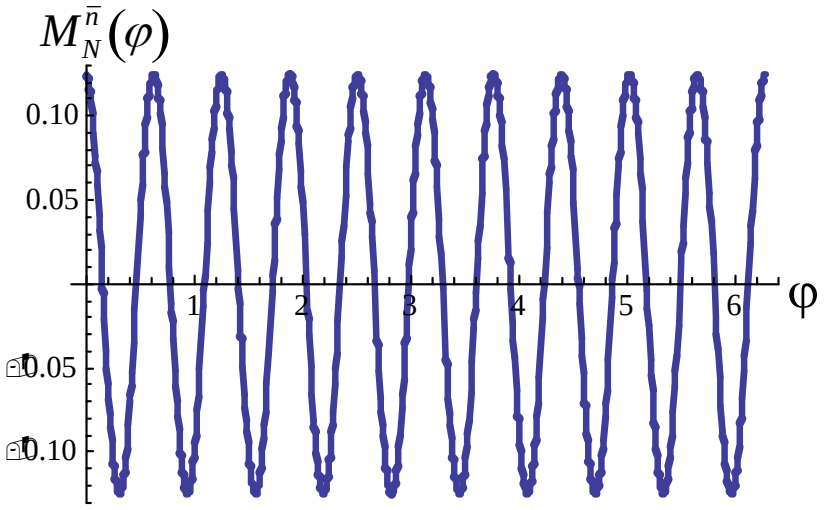

Figure 8: The 0NN0-N00N-Expectation Operator of Eq.10 For a Single Detection Event Corresponding to $\bar{n} = N = 10$ in a Two-Mode Coherent State

Such a smarter strategy is to recognize that number-resolving detectors (NRD) can in principal detect all photon numbers, not just $N = 10$. Current technology can efficiently detect in the range of 0 through 20 photons with 95% efficiency and virtually no dark counts (10^{-6} per second) [Lita2008]. Hence the NRD will produce a sequence of interference terms of the form of Eq.10, each with its own weight factor $Ne^{-\bar{n}}/N!$ and super-resolving phase factor, $\cos(N\varphi)$. The key idea is to treat each of these 20 or so terms as individual terms in a Fourier cosine series. We are then at liberty to sum the contributions from each of the N = 0 through N = 20 photons counted, while keeping a fixed $\bar{n} = 10$. This can all be carried out in post-processing of the data. Hence we define a new operator, the sum of 0NN0-N00N operators over N, as,

$$S_{AB}^{N00N} = \sum_{N=0}^{\infty} \left(|0\rangle_A |N\rangle_B \langle N|_B \langle 0|_A + |N\rangle_A |0\rangle_B \langle 0|_B \langle N|_A \right), \qquad (11)$$

where we have taken the sum to infinity, without loss of generality, to reflect that the probability of the large N terms contribution drops off exponentially for any $N >> \bar{n}$, as seen in Fig.7. Taking the expectation with respect to the operator of Eq.11 and the dual coherent state of Eq.7, we arrive at the expression,

$$M_{\Sigma}^{\bar{n}}(\varphi) \equiv e^{-\bar{n}} \sum_{N=0}^{\infty} \left[(\bar{n}/2)^N \cos(N\varphi)/N! \right] = 2e^{-\bar{n}\left[1/2+\sin^2(\varphi/2)\right]} \cos\left[\bar{n}\sin(\varphi)/2\right], \qquad (12)$$

where the infinite series, somewhat surprisingly, may be summed exactly to give the final expression. This is then the measurement outcome corresponding to applying a sum of 0NN0-N00N operators to the dual mode coherent state. In Fig.9, below, we plot the sum of 0NN0-N00N measurements (green, $\bar{n} = 10$), over the range from $-\pi$ to π. Here again we note that $\bar{n} = 10$ is tuned to be the number of photons on average arriving at the detector after loss.

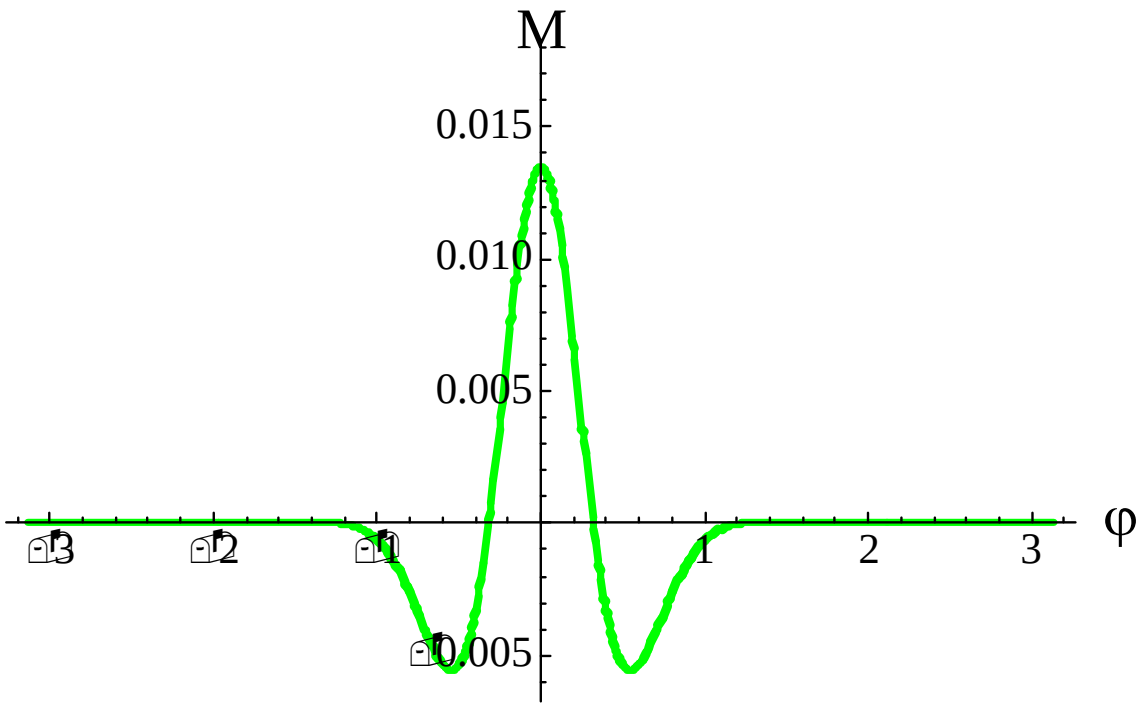

Figure 9: The Sum of All the 0NN0-N00N, for Eq.12 from the Number Resolving Detection of the Dual Coherent State With $\bar{n} = 10$

From Fig.9 we see that the sum of 0NN0-N00N strategy keeps a super-resolving central peak, but the fringes or side lobes in a single 0NN0-N00N term have washed out. Unfortunately a signal-noise-analysis shows that this detection scheme is also worse than the SNL, and again the culprit is that we have thrown out too many photons. The sum over the 0NN0-N00N terms are a sparse set in the entire dual mode coherent state. However, this result suggests what will be our final protocol. We will sum over all the photons in the dual-mode coherent state, in such a way that we keep all of the photons, but sum over the phase carrying off-diagonal terms in the two-mode density matrix for the dual-mode coherent state.

We define an off diagonal two mode Hermitian operator $\hat{\mu}$ based on the M&M states as,

$$\hat{\mu} \equiv \sum_{M,M'=0}^{\infty} |M\rangle_A |M'\rangle_B \, {}_A\langle M| \, {}_B\langle M'|, \tag{13}$$

which reduces to the sum of 0NN0-N00N operators when $M = N$ and $M' = 0$. It is easy to show that, due to symmetry of interchange of the summation indices, that $\hat{\mu}^\dagger = \hat{\mu}$ and hence the operator is Hermitian. The operator is idempotent, as is easy to show, and hence $\hat{\mu}^2 = \hat{I}$, the identity operator. It is easy to see that this operator is the sum of all the phase carrying off diagonal terms in the two-mode space of the dual mode coherent state, and the square of this operator is just the sum of the diagonal terms, which give the two-mode identity. With these properties we can now find the expectation value and the minimal detectible phase for the two-mode coherent state, Eq.7 as the remarkably simple expressions,

$$\langle \hat{\mu} \rangle = {}_{AB}\langle \alpha | \hat{\mu} | \alpha \rangle_{AB} = e^{-2n\sin^2(\varphi/2)}, \tag{14}$$

and

$$\Delta\varphi^2 = \frac{e^{4\bar{n}\sin^2(\varphi/2)} - 1}{\bar{n}^2 \sin^2(\varphi)} \tag{15}$$

In Fig.10, below, we plot together the coherent state with classical detection (red) the single *N = 10* N00N component (purple) and the expectation of the $\hat{\mu}$ operator with $\bar{n} = 10$ (blue) and $\bar{n} = 100$ (green).

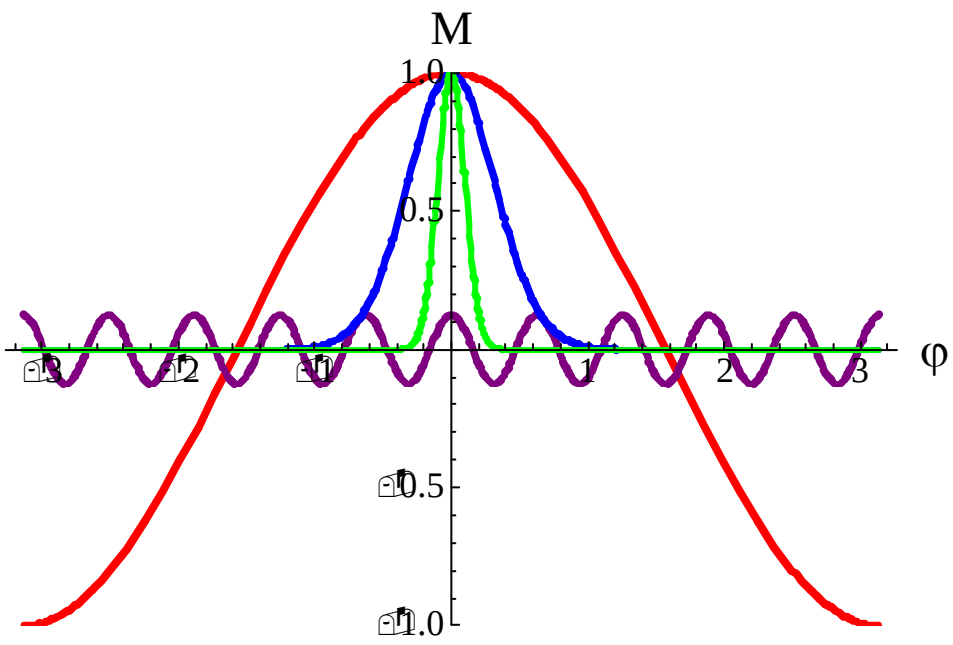

Figure 10: The Classical State (Red), the Single 0NN0-N00N Term (Purple), and the Sum of All the Off Diagonal M&M Terms with $\bar{n}=10$ (Blue) $\bar{n}=100$ (Green)

We see that the blue and green curves are both super-resolving, but it takes a return power of $\bar{n}=100$ now to get ten-fold super-resolution, instead of the $\bar{n}=10$ required of the 0NN0-N00N schemes. This is easy to see analytically in that Eqs.14 and 15 may be expanded in a Taylor series around $\varphi=0$ to get,

$$\langle\hat{\mu}\rangle \cong e^{-\bar{n}\varphi^2/2}, \tag{16}$$

and

$$\Delta\varphi \cong 1/\sqrt{\bar{n}}\ . \tag{17}$$

We can see from Eq.16 that signal is approximately a Gaussian of width given by Eq.17. Hence the signal to noise is exactly the SNL from Eq.17, but the signal is $\sqrt{\bar{n}}$ -fold super-resolving. The cost of adding more photons in the detection scheme to achieve the SNL is that a higher return power is required to achieve 10-fold super-resolution; that is $\bar{n}=100$.

Remarkably, the green interferogram of Fig.10 also illustrates a solution to a problem that has plagued N00N-state metrology in the absence of loss. Recall that a pure N00N state with a single 0NN0-N00N detection, depicted in Fig.5, has the *N*-fold increased oscillation period, which is the hallmark of the N00N state scheme. This super-resolution allows for improved *local* phase sensitivity, which requires that one have a priori information about which fringe you are on [Durkin2007]. Without this a priori information, one must use too many photons to decide which fringe one is at before one can take advantage of the *N*-fold steeper slope, and hence the N00N state scheme performs much worse for global

phase measurement, typically only at the SNL. For some applications, such as Doppler velocity measurements, the need is only to have the ability to tell with high precision if any given fringe moves by a small amount. For such applications the over-all phase or global phase is not important; one just locks to the side of one fringe not caring which fringe it is. For other applications, such as LIDAR Mie scattering measurements, the absolute phase provides absolute information on aerosol particle diameter [Higgens2007], and here it is important to have global phase. Shapiro suggested an approach to global phase measurement using a coherent sum of N00N states, reducing the multiple fringes to a single narrow fringe in the range $-\pi$ to π [Shapiro1993, Shapiro1995]. Here we achieve the same effect not by transmitting a weighted superposition of N00N *states*, which would be rapidly attenuated by absorption and scattering, but rather by transmitting a dual mode coherent state, which suffers no worse absorption and scattering than classical light, and then executing a weighted superposition of phase carrying off-diagonal M&M *detection operators*. We have moved all of the "quantum" of the quantum sensor from the source to the detection, again putting us squarely in DARPA QSP Type-II. It also can be shown that the operator $\hat{\mu}$ of Eq.13 is closely related to the parity operator, discussed in Refs. Chiruvelli2008a, Gao2008, and Chiruvelli2008b. The parity operator can be implemented without NRDs, by using single-photon detectors, which can distinguish between zero or one or more photons. Such detectors are readily available and operate at much higher temperatures than the NRDs. This connection is a topic of ongoing research, but we feel that super-resolution with no worse than SNL sensitivity is well within reach of a realistic QSP Phase II statement of work.

We can estimate the signal to noise associated with the green interferogram in Fig.10. The curve has a non-zero minimum value at the point $\varphi = \pi$. Here we may evaluate the expression of Eq.12 to obtain,

$$\mathrm{SNR}_{\varphi=\pi}^{\bar{n}=100} \equiv 10\log\left(\frac{\left\langle \hat{\mu}_{\varphi=0}^{\bar{n}=100} \right\rangle}{\hat{\mu}_{\varphi=\pi}^{\bar{n}=100}}\right) = 869\mathrm{dB}, \tag{18}$$

which corresponds to the separation in signal at $\varphi = 0$ and noise at $\varphi = \pi$. If we instead average the signal over this range, vis,

$$\mathrm{SNR}_{\mathrm{AVG}}^{\bar{n}=100} \equiv 10\log\left(\frac{\left\langle \hat{\mu}_{\varphi=0}^{\bar{n}=100} \right\rangle}{\frac{1}{2\pi}\int_{-\pi}^{\pi}\left\langle \hat{\mu}_{\varphi}^{\bar{n}=100} \right\rangle}\right) = 14\mathrm{dB}, \tag{19}$$

still provides a huge separation for the signal at $\varphi = 0$ and the average signal over the 2π range.

To summarize, we have discovered numerically, and then provided analytical reasoning, that the optimal quantum LIDAR (QuLidar) scheme in the presence of high loss (greater than 6dB) is to use a dual-mode coherent state, which suffers only the classical Beer's law for loss due to attenuation and scattering. Then in the number resolving detector we project out this essentially classical state into the quantum M&M basis and *then* sum over all *M*. Such a quantum detection scheme is radically different than typical intensity differencing. The terms in the sum near $\bar{n} = N = 100$ add constructively to give the well defined, super-resolving peak, with unit visibility, indicated in Fig.10 (green), that is separated by 869dB from the minimal background and by 14dB from the average count. The point then is that by using "classical" coherent light in propagation, we do not suffer the super-Beer loss associated with propagating quantum states, putting our proposed scheme firmly in QSP Type-II quantum sensor, defined as where only classical light propagates to the target. However a "classical" coherent state *is* a quantum state. We exploit this in the quantum detection scheme with number resolving detectors to project out the super-resolving terms, and the sum them so that we do no worse than shot-noise in sensitivity while maintaining ten-fold super resolution. In addition the connection between the sum of the M&M operator and the parity operator $(-1)^{\hat{n}}$ opens the door for not using NRD at all but instead the much more commonly available single-photon counters, which need only distinguish between zero and more photons [Chiruvelli2008a, Gao2008, Chiruvelli2009]. Such a single-photon detection scheme is quantitatively the same as a similar result arrived at independently by Tsang [Tsang2009].

In the following we will provide more details of the work supported by this DARPA QSP grant but the above summary is our primary conclusion. Our proposed dual coherent state scheme with number-resolving detectors meets all of the DARPA QSP metrics for a successful Phase I. What is especially appealing about our proposal for the quantum LIDAR is that it does not require squeezed light, only number resolving detectors, which are now becoming widely available due to development for quantum information processing tasks. In Sec.8.0 below we illustrate a proof of principal experiment, performed in collaboration with Dr. Alan Migdall at NIST, which illustrates the super-resolving phase components for each photon number in a coherent state interferometer [Wildfeuer2008].

In the Appendix we will recap the M&M state results [Huver2008], which are optimal for low loss, and also include a discussion of a high flux M&M and N00N generation schemes [Glasser2008, Cable2009]. In Secs. 6.0 and 7.0 we will discuss the results of the numerical code and optimization. In Sec.8.0 we will discuss the number-resolving detection experiment [Wildfeuer2008]. In the Appendix we present our work on a unified measurement scheme for N00N state interferometry and the investigation of another type of "optimal" state interferometry in the presence of loss [Gao2008, Chiruvelli2008a, Chiruvelli2008b]. In Sec.9.0 we discuss the quantum derivation of Beer's and super-Beer's laws, discuss a class of entangled states that obey ordinary Beer's law, and then finally in Sec.10.0 we discuss the Raytheon models of atmospheric loss and turbulence we plan to utilize for Phase II. Given that our plans for Phase II amount to coherent state propagation, the other great thing about our proposal is that we do not need to adapt the atmospheric codes to propagate quantum states. They can be used as is.

2.2 Summary of Deliverables

Deliverables Theory Base:

- Theory and models of Type-I and Type-II spontaneous parametric down conversion (SPDC), optical parametric amplifier (OPA), optical parametric oscillator (OPO), and entangled-photon Laser (EPL) sources of bright squeezed and entangled light sources for QuLidar A & B. (Completed except for the EPL source, which we decided was too weak and too fragile for practical Type II LIDAR.)
- Theoretical comparison of the performance such bright sources of squeezed and entangled light sources in the QuLidar A & B configurations, with respect to a 10-fold resolution and 26 dB signal to noise improvement in a 3 dB noise environment (completed).
- Theoretical models of noise degradation in QuLidar A & B systems due to photon losses (completed).
- Theory and models of noise and loss mitigation through decoherence-free subspace approaches (completed).
- Theory and models of quantum-enhanced timing and ranging (completed).
- Theory and models of dispersion cancellation in QuLidar A & B systems (in progress).
- Provide technical reports and systems engineering analysis to determine military utility, mission control operations (CONOPS), and viable concept designs for quantum-sensor applications (completed).

Publications and Preprints Produced:

[Cable2009] Cable, H; Vyas, R; Singh, S; Dowling, JP; Theoretical investigation of a non-degenerate optical parametric oscillator as a high-flux source for quantum lithography, in preparation (to be submitted to Physical Review).

[Chiruvell2008] Chiruvelli, A; Lee, H; Parity Measurements in Quantum Optical Metrology; arXiv:0901.4395 (to be submitted to Physical Review).

[Chiruvell2009] Chiruvelli, A; Lee, H; Canonical Phase Measurements in the Presence of Photon Loss; arXiv:0811.2780 (to be submitted to Physical Review).

[Dowling2008] Dowling, JP; Quantum optical metrology — the lowdown on high-N00N states; CONTEMPORARY PHYSICS, 49 (2): 125-143 2008.

[Gao2008] Gao, Y; Lee, H; Sub-shot-noise quantum optical interferometry: a comparison of entangled state performance within a unified measurement scheme; JOURNAL OF MODERN OPTICS, 55 (19-20): 3319-3327 2008.

[Gao2009] Gao, Y; Wildfeuer, CF; Lee, H; Dowling, JP; Super-Resolution at the Shot-Noise Limit with Coherent States and Photon-Number-Resolving Detectors, in preparation (to be submitted to Physical Review).

[Glasser2008] Glasser, RT; Cable, H; Dowling, JP; Entanglement-seeded, dual, optical parametric amplification: Applications to quantum imaging and metrology; PHYSICAL REVIEW A, 78 (1): Art. No. 012339 JUL 2008.

[Huver2008] Huver, SD; Wildfeuer, CF; Dowling, JP; Entangled Fock states for robust quantum optical metrology, imaging, and sensing; PHYSICAL REVIEW A, 78 (6): Art. No. 063828 Part B DEC 2008.

[LeeTW2009] Lee, TW; Huver, SD; Lee, H; Kaplan, L; McCracken, SB; Min, C; Uskov, D; Wildfeuer, CF; Veronis, G; Dowling JP; Optimization of quantum interferometric metrological sensors in the presence of photon loss, in preparation (to be submitted to Physical Review).

[Sciarrino2008] Sciarrino, F; Vitelli, C; De Martini, F; et al., Experimental sub-Rayleigh resolution by an unseeded high-gain optical parametric amplifier for quantum lithography, PHYSICAL REVIEW A, 77 (1): Art. No. 012324 JAN 2008.

Invited Talks:

"Quantum Technologies — The Second Quantum Revolution," Jonathan P. Dowling, US Army Emerging Technologies Seminar, 6–9 October 2008, McLean, Virginia (invited).

"Quantum Technologies — The Second Quantum Revolution," Jonathan P. Dowling, US Army Future Technology Seminar, 19–21 August 2008, Portsmouth, Virginia (invited).

"Linear Optical Quantum Computing, Imaging, and Sensing," Jonathan P. Dowling, Asia Pacific Conference on Quantum Information Science, 2–5 July 2008, Cairns, Australia (invited).

"What's New with N00N States?" Jonathan P. Dowling, SPIE Photonics West: Quantum Electronics Metrology, 19–24 January 2008, San Jose, California (invited).

"Quantum Sensors: The Lowdown on High-N00N", Jonathan P. Dowling, 38th Winter Colloquium on The Physics of Quantum Electronics, 6–10 January 2008, Snowbird, Utah (plenary).

"Quantum Optical Metrology," Christoph F. Wildfeuer and Jonathan P. Dowling, Conference: IV workshop ad memoriam of Carlo Novero, Advances in Foundations of Quantum Mechanics and Quantum Information with Atoms and Photons, 19–23 May 2008, Turin, Italy (invited).

"Metrology with a Fabry-Perot interferometer and entangled states of light," Christoph F. Wildfeuer, Sean D. Huver, and Jonathan P. Dowling, SPIE Photonics West, San Jose, CA, 24–29 January 2009 (invited).

"Density Matrix Formalism for Heisenberg-Limited Interferometry," Hwang Lee, SPIE Photonics West 2009, San Jose, CA, January 24–29, 2009 (invited).

"Heisenberg-Limited Optical Interferometry: A Universal Detection Scheme," Hwang Lee, 17th International Laser Physics Workshops, Trondheim, Norway (June 30–July 4, 2008, (invited).

"Quantum Sensors in a Lossy Medium," Hwang Lee, SPIE Defense and Security Symposium, Orlando, FL, March 16–20, 2008 (invited).

"The effect of path absorption on phase sensitivity with entangled states" Yang Gao and Hwang Lee, SPIE Photonics West 2008, San Jose, CA, January 19–24, 2008 (invited).

"Sub-Shot-Noise Optical Interferometry," Hwang Lee, 38th Winter Colloquium on the Physics of Quantum Electronics, Snowbird, UT, January 6–10, 2008 (invited).

2.3 Intellectual Property

The information in Sec. 7.0 is Raytheon proprietary information and should not be distributed outside of the US Government.

2.4 Discussion of Proposer's Previous Accomplishments

Previous Accomplishments, Theory Base (LSU, MSA, Raytheon):

The LSU activity has spearheaded the use of squeezed and entangled states of both light and atoms in the use of quantum sensors. In particular the PI (Dowling) has investigated the use of squeezed and entangled sources in sensors for over 15 years (while at LSU, NASA JPL, and US Army Aviation & Missile Command) including work on the phase sensitivity of atom gyros [Scully1993, Dowling1998], quantum-optical states of ultimate phase resolution [Schleich1991, Dowling1991], quantum imaging and lithography [Boto2000, Strekalov2002], and quantum sensors [Kapale2005]. In fact, in the paper of Boto, *et al.*, our team first pointed out the sub-Rayleigh diffraction effect of entangled photons for quantum imaging. Consequently, our team has led the way in the study and efficient generation of N00N and related states for quantum imaging and metrology [Lee2002a, Lee2002b, Kok2002, Kok2004, Durkin2006, Wildfeuer2006, VanMeter2006]. In addition, LSU and MSA have collaborated over the past seven years on quantum sensor projects under the auspices of the National Reconnaissance Office (NRO) Director's Innovation Initiative (DII). These projects have included quantum-entangled gravity gradiometers and gyroscopes [Dowling1998, Yurtsever2003], magnetometers, and clock-synchronization protocols [Jozsa2000, Yurtsever2002]. Dowling (LSU) and Yurtsever (MSA) have also collaborated on a previous DARPA project on entangled gravity gradiometers. Dowling is currently working on Department of Defense (DoD)-funded projects in optical quantum information processing and quantum imaging. Raytheon is a defense contractor that is well familiar with the requirements of a DoD remote-sensing system, and Wilkinson (Raytheon) has many years experience in optical remote sensing, as well as quantum optics theory and experiment, having done his PhD work with Prof. Marlan Scully.

2.5 Description of the Facilities

Dowling and H. Lee mentor a large number of postdocs (3), graduate (8), and undergraduate students (3) in the Quantum Science and Technologies (QST) group of the Hearne Institute for Theoretical Physics (HITP) and the Physics & Astronomy (P&A) department, working on projects related to quantum-optical information processing. These projects include quantum imaging, optical quantum computing, quantum sensing, and the theory and modeling of photonic crystals. The QST group has four, networked, Dell workstations for computational modeling and design theory. Tae-Woo Lee holds a staff position at the Center for Computation and Technology (CCT), and in particular has access to the supercomputing facilities there. T.W. Lee has world-class expertise in the numerical modeling of linear and nonlinear optical devices. LSU also has access to very good library resources and Dowling has access to the NASA Jet Propulsion Laboratory (JPL) online library system as well. Drs. H. Lee and T.W. Lee, are part of a LSU-wide quantum optics and microphotonics strategic hiring initiative that Dowling leads at LSU, which is joint with CCT, HITP, Physics & Astronomy (P&A), ECE, and Math Departments — encompassing the CCT and the Colleges of Basic Science, Engineering, and Arts & Science. This LSU-

funded microphotonics initiative forms the core of personnel and facilities for this proposal — leveraging funding from the State of Louisiana. The Hearne Institute is funded by a donation of two endowed chairs by Horace Hearne Jr. and the State of Louisiana, as well as additional grants from a variety of national and international granting agencies. It currently has as co-directors the LSU Flagship Faculty members, Profs. Jonathan Dowling and Jorge Pullin. The institute hosts faculty, postdoctoral researchers, students — as well as long- and short-term visitors — who conduct research on quantum technologies and on gravitational physics. The Hearne Institute also sponsors international workshops on quantum information theory, quantum technologies, relativity, and quantum gravity.

The Center for Computation & Technology, or CCT, is an interdisciplinary research center located on the campus of LSU in Baton Rouge, Louisiana. The CCT advances the LSU Flagship Agenda and promotes economic development for the state by using computational applications to aid research and develop solutions that benefit academia and industry. CCT is an innovative research environment, advancing computational sciences, technologies and the disciplines they touch. Researchers at CCT use the advanced cyber-infrastructure — high-speed networks, high-performance computing, advanced data storage and analysis and hardware and software development — available on campus to enable research in many different fields. By uniting researchers from diverse disciplines, ideas and expertise are disseminated across LSU departments to foster knowledge and invention. The CCT has an annual budget from the state of Louisiana of $9M/year. For example, one of the super computers available for this project is a 50.7 TFlops Peak Performance, 680 node, 2 Quad-Core processor Red Hat Enterprise Linux (RHEL) v4 cluster from Dell with 2.33 GHz Intel Xeon 64bit processors and 8 GB RAM per node. Another is a 15.322 TFlops Peak Performance, 360 node, 2 Dual-Core processor Red Hat Enterprise Linux v4 cluster from Dell with 2.66 GHz Intel Xeon 64bit processors and 4 GB RAM per node. There are many others included those networked to the Louisiana Optical Network Initiative (LONI). These resources were be used in addition to the HITP mini-cluster of Dell workstations, to be purchased on this grant. The mini-cluster was be dedicated to this project.

2.6 Formal Teaming Agreements

2.6.1 Programmatic Relationship of Team Members

Professor Jonathan Dowling of LSU was the team lead, who has coordinated the activities on a weekly basis through email, teleconferences, and site visits. Dowling (LSU) has a close working relationship with all team members, and historically this team has worked well on quantum sensor and related projects in the past. Yurtsever worked closely with the LSU teams by telecom and with Raytheon regularly on site visits due to collocation. The CCT and LSU personnel met weekly and Raytheon and MathSense participated by telecon.

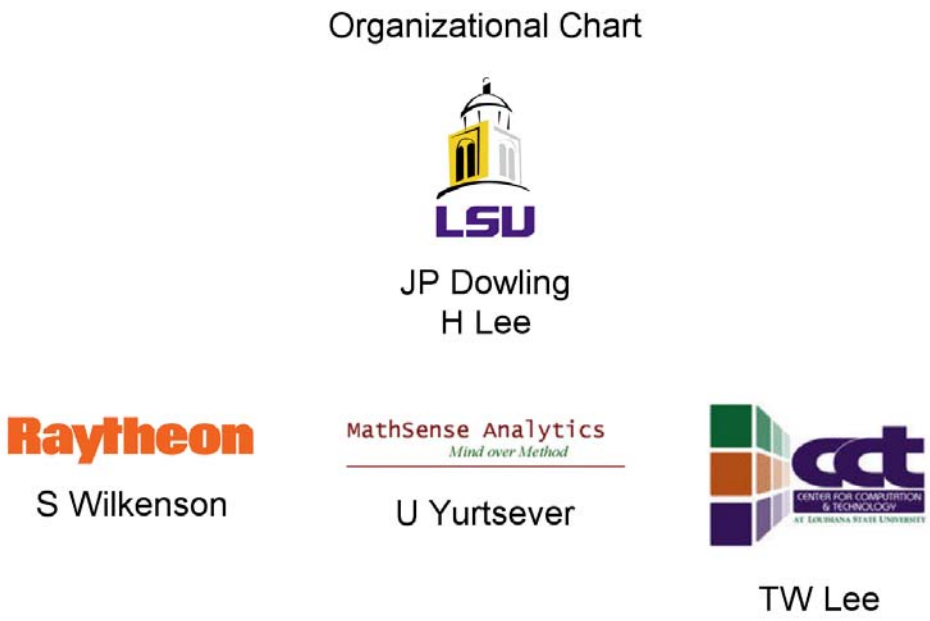

Figure 11: Organizational Chart

2.6.2 Unique Capabilities of Team Members

Dowling at LSU was lead theorist, whose background in quantum sensors and sub-Rayleigh-diffraction-limited lithography played a key role in evolving the theory base. H. Lee at LSU provides quantum optics analytical expertise. Yurtsever at MSA has a unique background in analytic and theoretical physics techniques in quantum sensors, and brought formidable analytical capabilities to bear on the project. T.W. Lee at LSU-CCT has extensive experience in the computational modeling of quantum sensors, and formed the information-technology base of the team. Wilkinson at Raytheon has wide-ranging experience in the theory and experiment of quantum-optical systems, and has a unique ability as a prime defense contractor, well experienced in remote sensing for the DoD, and so brings the systems-engineering skills that will become a critical component as our team advances to Phase II and beyond.

2.6.3 Task Responsibilities of Team Members

Dowling (LSU) simultaneously served as team leader (PI) and the theory base leader, jointly in the latter role with H. Lee (HITP-LSU) and Yurtsever at (MSA), who coordinated the Los Angeles theory and modeling activities. T.W. Lee (CCT-LSU) acted as the point of contact on numerical simulations, while Yurtsever and Dowling provided the analytical models to be used in the computer codes. Wilkinson (Raytheon) worked on the development of systems engineering and design tools to facilitate the Phase I transition into a high-performance DoD system, particularly the atmospheric modeling. The key goal of the theory base was to develop realistic models of noise and loss in the proposed quantum-lidar systems, and particularly to find a new class of super-resolution and super-sensitivity quantum states that have similar performance as N00N states, but are much more robust against loss, which we have done as outlined above.

2.6.4 Key Personnel & Amount of Effort

Amount of Effort — Theory Base: Prof. Jonathan Dowling (PI) is the Director of the Hearne Institute for Theoretical Physics (HITP) at LSU, and devoted one month per summer per year for two years full time to the project. He spent a portion of these summer months at MSA and Raytheon, in order to be better able to coordinate the theory base activities located in the Los Angeles area. In addition, Prof. Hwang Lee, also at LSU, who is the Deputy Director of the HITP, assisted Dowling. Dowling and Lee mentored an LSU postdoc, Dr. Wildfeuer, who was devoted full time to this project. Lee first developed the first linear-optical approach for N00N-state generation [Lee2002a, Kok2002], and was co-author on our recent paper on quantum sensors [Kapale2005]. Lee also devoted two months of his summer over two years to the project, while the postdoc was full time over the 18-month duration. Dr. Ulvi Yurtsever has collaborated for years with Dowling, T.W. Lee and H. Lee on the theory of quantum sensors and was the primary point of contact for the theory base effort. Yurtsever devoted 33% of his time over the 18-month period of effort. T.W. Lee carried out the simulation and modeling tasks at CCT-LSU in coordination with the rest of the theory base members and devoted 40% of his time to the task over his 15-month period of performance. (T.W. Lee started late due to the JPL contract issues.)

2.6.5 Biographies of Key Personnel

Jonathan P. Dowling (Principal Investigator, LSU): Prof. Dowling is the Horace C. Hearne Jr. Professor of Theoretical Physics and Director of the Hearne Institute for Theoretical Physics, Quantum Science and Technologies Group, Department of Physics and Astronomy, Louisiana State University, Baton Rouge, Louisiana. Prof. Dowling received his BS in physics (with honors) from the University of Texas at Austin. He then received his MS in applied mathematics, MS in physics, and PhD in mathematical physics, all from the University of Colorado at Boulder. He was a Visiting Research Scientist at the International Center for Theoretical Physics in Trieste, Italy; a Postdoctoral Research Scientist at the Max Planck Institute for Quantum Optics in Garching, Germany; and a National Research Council postdoctoral research associate in the Optical Science & Technology group at Army Aviation and Missile Command (AMCOM), Redstone Arsenal, Alabama. In he then joined AMCOM as a Research Physicist, where he won the Army Research, Development, & Achievement Award for his development of the theory of spontaneous emission in photonic crystals. He then left AMCOM to take a position as Research Scientist at the Senior Level in the Quantum Computing Technologies Group at JPL, where he was eventually promoted to Group Supervisor & Principal Scientist, before leaving to take the post in Louisiana. Dowling has over 130 published articles, and he holds eight US patents in the fields of nonlinear and quantum optics. He is a Fellow of the American Physical Society, the Institute of Physics, and the Optical Society of America, and has served on the editorial board of Physical Review, for the Journal of the European Optical Society, and for Concepts of Physics. He was awarded the Willis E. Lamb Medal for Laser Science and Quantum Optics (2002), a NASA Space Act Award (2002), and a US Army Research, Development, and Engineering Achievement Award (1996).

Hwang Lee (Co-Investigator, HITP & P&A, LSU): Prof. Hwang Lee is an Assistant Professor of Physics at Department of Physics and Astronomy, Louisiana State University. Lee received his PhD in Physics from Texas A & M University in 1998. He was a postdoctoral Research Associate in Department of Physics at Texas A & M University and also worked as a postdoc at NASA Jet Propulsion Laboratory under National Research Council Associateship Program (2000 to 2002). In 2002 he became a Senior-Level Research Scientist at the Jet Propulsion Laboratory in Exploration Systems Autonomy Section. He joined Louisiana State University in 2005. His research interests include high-precision optical interferometers and spectroscopy, single-photon generation, and optical quantum computing. He received the 2003 Outstanding Young Researcher Award from the Association of Korean Physicists in America for his contributions in quantum optics. He served as a program committee for Quantum Metrology session at the SPIE Photonics West Conference, Opto2008. Relevant Publications: [Wilde2008, Spedalieri2006, Florescu2005, LeeH2004b, LeeH2004a].

Tae-Woo Lee (Co-Investigator, CCT, LSU): Dr. Lee is an IT-consultant in the Center for Computation & Technology (CCT) at Louisiana State University, Baton Rouge, LA. Dr. Lee received his BS and MS degrees in physics from Inha University, Incheon, South Korea. During his MS degree in Inha University (1997), Dr. Lee worked on numerical modeling of high-field magnetization processes in rear-earth magnetic materials from which he has first gained research experiences in quantum mechanics areas. Then, Dr. Lee continued his study in Electrical and Computer Engineering at the University of Wisconsin-Madison, Madison, WI where he received the MS and Ph.D. degrees (2003). Major works during his Ph.D. dissertation involves with the development and application of numerical algorithms for modeling high-speed digital circuit interconnectors and linear and nonlinear photonic devices. Before Dr. Lee moved to Louisiana State University, he stayed at Argonne National Laboratory, Argonne, IL as a post-doctoral research associate where he focused his research on a nanophotonics area including plasmonic devices (2003 – 2007). Currently, Dr. Lee, as an IT-consultant at CCT, participates in various projects in collaborations with experimentalists and theoreticians. Dr. Lee's research areas include novel numerical approaches for nonlinear photonic system solvers, plasmonic bio-sensing devices and probes, and large-scale parallel computations. Relevant Publications: [LeeTW2001, LeeTW2004].

Steven R. Wilkinson (Co-Investigator, Raytheon): Dr. Wilkinson received a PhD with M.O. Scully in physics that specialized in the interaction of laser radiation with complex atomic systems. His PhD work was performed at Sandia National Labs that included both theoretical modeling and experimental verification. After a two year Post Doctoral Fellowship at the University of Texas, Dr. Wilkinson joined Hughes Aircraft that is now Space and Airborne Systems (SAS) Raytheon. While at Raytheon he has developed multidisciplinary system engineering expertise that covers a variety of platforms, air, ground, space, and sensors; including Radar, Electro-Optical/Infra-Red (EO/IR), Laser, and Passive RF. Three years ago Dr. Wilkinson initiated his current work to demonstrate the military utility of short pulse lasers. Previously he was investigating Air-Space integration of unmanned and reconnaissance systems for future missions. This investigation entails system-of-system analysis and development of requirements for the next generation of integrated systems. In addition to the Raytheon experience, prior to his PhD, he served in the Marine Corps with a primary responsibility in communications that involved limited Electronic Warfare and Signals Intelligence work.

Ulvi Yurtsever (Theory Base, Co-Investigator, MSA): Dr. Yurtsever brings a wide range of mathematical physics expertise to the project, including more than a decade of research experience in statistical physics, quantum field theory, foundations of quantum mechanics, and theoretical quantum optics. His current and recent research is focused on the development of novel information technologies inspired by the

interface between physics, information theory, and computation. His recently completed research projects involve quantum information theory and its applications to quantum sensors and quantum communications, including, as a Principal Research Scientist at NASA's Jet Propulsion Laboratory, research on the applications of quantum metrology to relativistic clock synchronization. Dr. Yurtsever is currently an independent Research Scientist at MathSense Analytics. Yurtsever received his PhD in Theoretical Physics in 1989 from the California Institute of Technology, and has authored over 40 articles in professional theoretical physics journals and conference proceedings.

2.7 Theory Base Statement of Work (SOW)

2.7.1 SOW Sensor Concept I — QuLidar-A

For the QuLidar-A Sensor Concept the Phase-I, Theory-Base Team developed models of noise and loss for the monostatic QuLidar system, where the sources to be analyzed and compared were all based on bright, Type-I, parametric-downconversion devices, typically from optically pumped nonlinear crystals with large $\chi^{(2)}$ optical behavior [Bialkowski1996]. The team developed models of such sources operated in the spontaneous parametric downconversion (SPDC) mode, the high-gain optical parametric amplifier (OPA) mode, the cavity resonant optical parametric oscillator (OPO) mode [Bialkowski1996, Kolobov1999], but not the newer cavity enhanced time-domain entangled photon laser (EPL) mode, which we ruled out as a viable approach early on [Lamas-Linares2001, Simon2003]. Each of these modes provides non-classical light with different brightness, spatio-temporal correlations, degrees of squeezing, and degrees of entanglement. Hence it was discovered, as expected that each source configuration had its own unique resolution and phase sensitivity characteristics, when operated as an interferometer. Nevertheless, the different sources all share sufficient commonalities to allow them to be analyzed, compared, contrasted, and modeled in a consistent theoretical and computational framework.

The theory team (LSU, MSA) developed noise and loss models to compare and contrast the different modes of operation and determine the degradation of the sensor system due to photon absorption and scattering between the source, target, and detector. The intent was to provide quantitative loss models that characterize the rollover of the non-classical resolution and sensitivity from the quantum into the classical domain, when compared with the equivalent coherent source operating at the same flux level. The modeling of the entire system was carried out on self-contained, modular computer codes (CCT-LSU), which will be interfaced as discussed in Sec.7.0, below. The goal was to specify QuLidar systems that give 10-fold resolution and 26 dB of signal to noise while operating with 3 dB of noise and photon loss.

A separate module for each of the different subsystems was designed and the modular format allowed different sources, imaging models, noise models, and detector schemes to be substituted without affecting the other modules. In this way the theory team rapidly explored trade-offs between source brightness, resolution enhancement, phase sensitivity, signal to noise, and robustness against noise. Dowling at LSU provided the underlying theory of the sources and imaging system. Yurtsever at MSA provided the underlying theory of the noise models and the detection schemes, utilizing input from the experimental options. T.W. Lee was tasked with developing the computer modules based on the theory and data provided. Wilkinson at Raytheon worked the rest of the theory team to extract design rules and perform a systems analysis of the most promising designs, with the goal integration into future DoD sensor prototypes, which in our final Type-II scheme simply involved modeling loss and scattering of coherent states in the atmosphere. The most promising systems were characterized and detailed and their performance metrics provided to DARPA. All of the Theory-Base Members devoted 50% of their time, of this project, on Sensor Concept I — QuLidar A.

• Months 1–6: Theory of QuLidar A sources, imaging systems, noise, and detection developed.
• Months 7–12: Theory integrated into computer modules for each of the four subsystems.
• Months 13–18: Loss data from experimental options inputted into computer simulations.
• Months 13–18: Target high performance sensor systems down selected.
• Months 13–18: Systems integration analysis performed.

2.7.2 SOW Sensor Concept II — QuLidar-B

Given that the Sensor Concept II — QuLidar B — is based on the replacement of Type-I with Type-II downconversion sources in the sensor system, the SOW for this concept is identical to that of QuLidar A with this replacement and a few modifications in the theory and simulations. (Note that Type-I and Type-II here refer to the polarization properties of the source and are not to be confused with Type-I, II, and III quantum sensors identification by DARPA based on entangled and non-entangled states.) An executive decision was made to split the concepts in this fashion, due to the different nonlinear optical crystals used in the two concepts, the different way these crystals are pumped and phase-matched, and the different way the polarization-entangled photons will have to be treated as far as the imaging system, the interaction with the target, and sources of noise. However, the research was parallel to the QuLidar A SOW and was carried out simultaneously by the Phase-I Theory-Base Researchers, so we have split their time between the two sensor concepts equally.

• Months 1–6: Theory of QuLidar-B sources, imaging systems, noise, and detection developed.
• Months 7–12: Theory integrated into computer modules for each of the four subsystems.
• Months 13–18: Loss data from experimental options inputted into computer simulations.
• Months 13–18: Target high performance sensor systems down selected.
• Months 13–18: Systems integration analysis performed.

For all of these interrelated tasks, a detailed description of the statistical and correlation properties of the signal is one of the first questions that need to be explored. Most standard signal-processing techniques rely on the known correlation properties of the optical signal and its accompanying noise. It is therefore imperative for imaging and ranging applications to develop a solid understanding of the foundations of entangled-light optics and the coherence properties of entangled light in optical media. Investigations of the behavior of entangled light in the presence of common optical elements (such as lenses, diffraction

gratings, beamsplitters, etc.) have barely begun, and so far have focused only on special configurations such as the light output by SPDC crystals [Abouraddy02]. We developed a general formalism to describe the optical behavior of many-photon-entangled light, such as focusing, diffraction, imaging and coherence.

2.8 Cost, Schedule, and Milestones: Theory Base

2.8.1 Sensor Concept I — QuLidar A

Month	Milestone	Approximate Expenditure
1–6	Theory of Sensor Components	$100K
7–12	Computer Module Development	$100K
13–18	Loss Data Integration	$50K
13–18	Down selection	$50K
13–18	Systems Analysis	$75K

2.8.2 Sensor Concept II — QuLidar-B

Month	Milestone	Approximate Expenditure
1–6	Theory of Sensor Components	$100K
7–12	Computer Module Development	$100K
13–18	Loss Data Integration	$50K
13–18	Down selection	$50K
13–18	Systems Analysis	$75K

3.0 QUANTUM THEORY OF LOSS IN QUANTUM LIDAR SENSOR

3.1 Introduction

This section summarizes how we treat quantum states of light propagating through a lossy medium and how we set up a theoretical framework that we used in our numerical codes. First, we developed a density-matrix formalism for a generic two-way interferometer, in which the amount of photon loss can be arbitrarily high. Then, for an arbitrary input state, each matrix element of the desired reduced density matrix was obtained explicitly after the propagation loss.

3.2 Loss Treatment

In quantum optics, the photon loss is typically modeled by a beam splitter [Loudon2000]. In doing so, we first need to enlarge the Hilbert space to include the modes that represent the scattered photons and then, after the scattering, trace out those modes. As a first step we extend the beam splitter model for loss to two propagating modes that represent the two paths in the optical interferometer. For the two input ports of an interferometer, any arbitrary pure-state input with *N* photons can be written as:

$$\left|\psi\right\rangle_{\text{input}} = \sum_{k=0}^{N} \alpha_k \left| N-k, k \right\rangle, \tag{20}$$

where the α_k are the probability amplitudes associated with that particular quantum state. The two numbers inside the brackets represent the number of photons in the upper path and the lower path, respectively. Almost all the input states proposed for the Heisenberg-limited interferometry—with a notable exception of the squeezed states—are described by Eq.20. Such a quantum state resides in a Hilbert space of *N+1* dimension.

The transformation of the quantum state by any passive lossless optical elements for an interferometer such as beam splitters, phase shifters, and mirrors can then be described by an *(N+1)* by *(N+1)* unitary matrix. Analysis of a lossless interferometer with the input state of Eq.20 can be as simple as following the rotation of the state vector in the *N+1* dimensional Hilbert space.

However, when the propagation channels suffer from photon losses, the state vector description of the quantum state of light is no longer possible. First of all, we need to consider the total density matrix that includes all the modes for the scattered photons. Then, we obtain the reduced density matrix for the two interferometer modes by tracing out the modes for those scattered photons. The reduced density matrix then necessarily becomes an object that lives in a much larger Hilbert space that covers smaller number of photons, *(N+1)(N+2)/2*, to be precise. Pictorially, we may view this process as depicted in Fig.12.

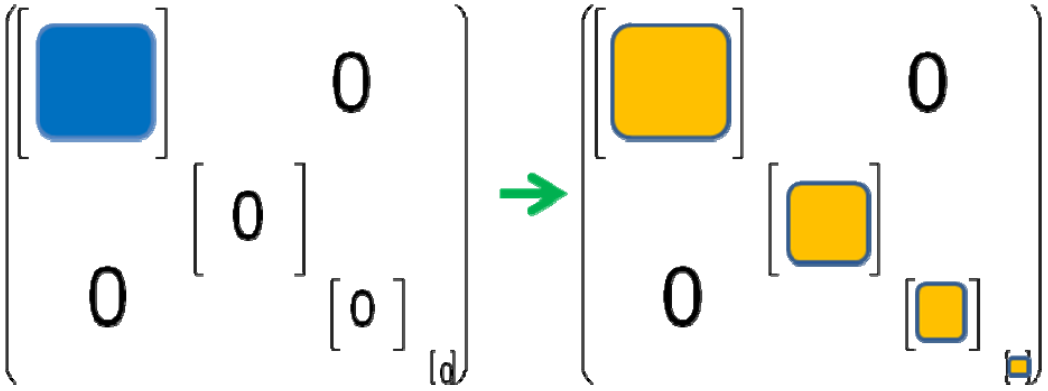

Figure 12: The Initial Density Matrix Before the Loss (Left) and the (Reduced) Density Matrix After the Loss (Right)

After passing through the two beam splitters — representing the two lossy channels in the two arms of the interferometer — the density matrix for the two main modes now consists of *N+1* different-size blocks. Each of these blocks (the boxes in the right of Fig.12) represents the corresponding number of photon lost. In other words, the quantum state of light ends up in the *N+1–L* dimensional Hilbert space if total of *L* photons are lost.

Now let us look at the $(i, j)^{\text{th}}$ component in the *L*-th block on the right hand side of Fig.12 *(L = 0, 1,⋯, N).* It corresponds to the density matrix element associated with the operator $|N-L-i,i\rangle\langle N-L-j,j|$ in the usual ket-bra notation. Our aim is to find the value of the density matrix element, if the input state α_k and the loss parameter are given. The beam splitter is typically described with a unitary transformation between the input and output modes [Scully1997, Loudon2000]:

$$\begin{pmatrix} \hat{a}_{out} \\ \hat{b}_{out} \end{pmatrix} = \begin{pmatrix} r & t \\ t & r \end{pmatrix} \begin{pmatrix} \hat{a}_{in} \\ \hat{b}_{in} \end{pmatrix}, \tag{21}$$

where $\hat{a}_{in}$, $\hat{b}_{in}$ ($\hat{a}_{out}$, $\hat{b}_{out}$) are the annihilation operators for the input (output) modes of the beam splitter, and *r* and *t* are the reflection and transmission coefficients, respectively.

The unitary (conservation of probability) condition provides the relations $|r|^2 + |t|^2 = 1$ and $r\,t^* + t\,r^* = 0$. For a 50-50 beam splitter, we follow the reciprocity convention of using $r = 1/\sqrt{2}$ and $t = i/\sqrt{2}$. Using the beam splitter model for loss, the probability for a single photon loss is given by the reflectivity $|r|^2$, which will serve as the loss parameter (the fraction of photons reflected into the environment and lost).

Let us look back to the density matrix element associated with $|N-L-i,i\rangle\langle N-L-j,j|$. Let us first look at the ket part $|N-L-i,i\rangle$. Now suppose the input state was $|N-k,k\rangle$. We are now going to construct the probability amplitude corresponding to the transition:

$$|N-k,k\rangle \Rightarrow |N-L-i,i\rangle . \tag{22}$$

If $N-k < N-L-i$, or $k < i$, the transition probability is zero, since the number of photons cannot be increased by a loss event. Hence, the *k* values are restricted as

$$i \le k \le i+L , \tag{23}$$

and the probability amplitude for a given transition can be written as:

$$A_k = F_{1k}\ {}_{N-k}C_{N-L-i}\, t^{N-L-i} r^{L+i-k}\, F_{2k}\ {}_{k}C_i\, t'^{i}\, r'^{k-i} , \tag{24}$$

where F_{1k} and F_{2k} are numerical factors representing the relation between the normalized number states and the creation operators given by $|n\rangle = (\hat{a}^{+})^n |0\rangle / \sqrt{n!}$. In this case they are given by

$$F_{1k} = \sqrt{(N-L-i)!(L-i-k)!} / \sqrt{(N-k)!} \tag{25a}$$

$$F_{2k} = \sqrt{i!\,(k-1)!} / \sqrt{k!} \tag{25b}$$

The usual binomial coefficients are denoted as ${}_{N-k}C_{N-L-i}$ and ${}_{k}C_i$, meaning that, in the upper path, among *N–k* photons we choose *N–L–i* photons to transmit through the beam splitter and the rest (*L+i–k* photons) are then reflected. Therefore, *N–L–i* and *L+i–k* appeared as the power to the transmission and reflection coefficients, respectively. The same are the factors $F_{2k}\ {}_{k}C_i\, t'^{i}\, r'^{k-i}$ for the lower path, where *r'* and *t'* are the reflection and transmission coefficients for the lower path. Taking the numerical factors F_{1k} and F_{2k} into account the transition probability amplitude takes the form:

$$A_k = \sqrt{{}_{N-k}C_{N-L-i}}\, t^{N-L-i} r^{L+i-k}\, \sqrt{{}_{k}C_i}\, t'^{i}\, r'^{k-i} . \tag{26}$$

Now let us turn to the bra part of the operator $|N-L-i,i\rangle\langle N-L-j,j|$. Similarly, we suppose the input state was $|N-k',k'\rangle$ and evaluate the probability amplitude $B_{k'}$ for the transition:

$$|N-k',k'\rangle \Rightarrow |N-L-j,j\rangle . \tag{27}$$

Noting that the only differences between Eq.27 and Eq.22 are $k \to k'$ and $i \to j$, we obtain the corresponding transition probability amplitude as

$$B_{k'} = \sqrt{{}_{N-k'}C_{N-L-j}}\, t^{N-L-j} r^{L+j-k'} \sqrt{{}_{k'}C_{j}}\, t'^{j}\, r'^{k'-j} \quad . \tag{28}$$

Basically, the resulting coefficient for $|N-L-i, i\rangle\langle N-L-j, j|$ component of the density matrix given the N-photon input state is given by the combination of A_k multiplied by $B_{k'}{}^*$. One crucial point here before we combine A_k and $B_{k'}{}^*$: Since the reduced density matrix (right in Fig.12) is obtained by tracing out the modes for the scattered photon, the number of reflected photon in the expression 25 and 27 should be the same for the upper path and the lower path, separately. That said, we now have two constrains from the number of photons reflected in the expression of A_k and $B_{k'}$, namely

$$L + i - k = L + j - k', \tag{29a}$$

$$k - i = k' - j\,. \tag{29b}$$

These turn out to be the same constraint. Therefore, for fixed parameters *L*, *i*, and *j*, we obtain the matching values of *k* and *k'* are:

$$(k,\, k') = (i,\, j),\, (i+1,\, j+1), \cdots, (i+L,\, j+L)\,. \tag{30}$$

Taking the input state of Eq.20 into account, the reduced density matrix element is obtained as:

$$\rho_{N,L,i,j} = \sum_{m=0}^{L} (\alpha_{i+m}\, \alpha_{j+m}{}^*)\, A_{i+m}\, B_{j+m}{}^*, \tag{31}$$

where α_k , A_k , and B_k are given by Eqs. 20, 26, 28. Note that, for the given number of photons N, the L value determines which block the reduced density matrix element $\rho_{N,L,i,j}$ is and the value *i* and *j* determines which component it is inside that block. It can be numerically checked that the sum of all the diagonal elements of the reduced density matrix is unity, i.e., $Tr(\rho) = 1$, as it should be [Lee2009]. The Eq.31 provides a complete description of the effect of loss for an arbitrary two-mode input state with fixed number of photons. Based on the analysis depicted here, we will further investigate an even more general description that can include the case where only the average number of photons is fixed.

3.3 Beam-Splitter Transformation

Given that the loss description is in hand, it is relatively simple to describe the lossless linear optical elements in the interferometers. For a generic Mach-Zehnder interferometer, we have two beam splitters, two mirrors, and a phase shifter that may mimic the acquired phase difference between the two arms. The whole description of the interferometer is, of course, well known. One only needs to extend the description of the linear optical elements to the density matrix formalism — that is not necessary for the lossless situation. Simply put, the transformation of the density matrix by a passive lossless linear optical element can be represented by a unitary matrix as:

$$\rho_{out} = U\,\rho_{in}\,U^{+}. \tag{32}$$

For the lossless case (as depicted on the left in Fig.12), the density matrix is *N+1* by *N+1*, there by the *U* matrix is *N+1* by *N+1*. The expression of the unitary matrix in this case is well documented in the literature, and the explicit evaluation of each element may be easier to obtain when using the Schwinger representation. The Schwinger notation is simply to use the angular momentum eigenstates that correspond to the two-mode number states as follows:

$$\left| j, m \right\rangle = \left| N_a = j + m, N_b = j - m \right\rangle, \tag{33}$$

and the action of the optical elements are described by the rotation of the given angular momentum vector. In short, the unitary matrix representing the beam splitter, for example, not only becomes the same size of the reduced density matrix (left in Fig.12), but also has the same block diagonal form. The matrix elements in each block (say L^{th} block) now correspond to the ones for the lossless case with *N–L* photons. The explicit expression matrix element, $(i, j)^{\text{th}}$ component in the L^{th} block, then can be written as

$$(U_{BS})_{N,L,i,j} = e^{i(\pi/2)(m-n)}\, d^{\,j}_{m,n}(\pi/2), \tag{34}$$

where $d^{\,j}_{m,n}(\pi/2)$ is the rotation matrix element [Brink1993] and we have used change of variables as

$$j = \frac{N-L}{2}, \quad m = \frac{N-L}{2} - i, \text{ and } \quad n = \frac{N-L}{2} - j.$$

3.4 Complete Description of the Interferometer in a Lossy Environment

Finally, with the same variables the unitary matrix for the phase shifter can be written as

$$(U_{PS})_{N,L,i,j} = e^{-i\pi m}\,\delta_{i,j}, \tag{35}$$

Hence, the Eqs. 32, 34, and 35 complete the quantum mechanical description of the lossless interferometer. Now the complete description of the interferometer in lossy environment is to put all these three equations together with the loss transformation by the Eq.31. The output quantum state—that contains the information about the acquired phase shift—can now be precisely determined for any arbitrary input state of light. The remaining task is how to extract that information provided by a specific measurement scheme. Although the phase estimation needs to be performed after the output measurements, we may nevertheless be able to extract that information by investigating the off-diagonal elements of the final reduced density matrix. After all, the off-diagonal elements are responsible for the interference. In general, the detection scheme is represented by an observable, say $\hat{A}$, and the measurement outcome is given by the expectation value of $\hat{A} = Tr(\rho \hat{A})$, where the density matrix ρ is the one evaluated through Eqs. 31–35. We will then be able to test the performance of various input states and further investigate the optimal input states with specific measurement schemes as an inverse problem.

4.0 COMPUTER OPTIMIZATION OF QUANTUM LIDAR SENSOR

4.1 Introduction

This section reviews how we utilize computational approaches to address answers on theoretical performance of proposed quantum LIDAR systems. In particular, our main considerations are to provide theoretical guidelines for achieving resolution enhancement beyond classical limit. We focus on development and implementation of numerical tools and computationally obtained outcomes. Critical for the argument presented in Sec.5.0, above, the results indicate that the best strategy in the regime of very high loss due to absorption and scattering is to use two-mode coherent states and then implement a number-resolving detection scheme, which motivates the discussion in Sec.5.0, above.

One of unique features of the quantum LIDAR project under consideration can be found in the novelty of the system. The concept of using quantum states of light for LIDAR systems is new. Therefore, there should be many unknown factors and challenges we will encounter during progress of quantum LIDAR computer optimization development. Sometimes, it could significantly affect fundamentals of the problem that forces us to discard initial ideas or setup and adapt radically different new ideas. Normally, we expect that those changes will come in the middle of research progress. Having those facts in mind, we choose a modular based approach for developing numerical tools. Rather than handling a whole problem at once, we segmentize the problem. Each section of the problem is designed as a module such that it can be treated as independent problem. By combing those sections, or modules, a whole system can be constructed. Once a need for modification come up, one only focuses on specific modules under consideration to make changes. Those changes are supposed to have minimal influences to the other modules that have no relation to these changes. This approach allows us to quickly modify systems and eliminates need for rewriting an entire numerical code every time to change just one thing.

4.2 Computer Modules

An entire LIDAR system is schematically segmented as the following. To the left, a source component generates possibly entangled photons from spontaneous parametric down-conversion or even ordinary laser light. After that, the quantum photons are processed in a filtering stage to inject only a pure photon state into the next system. The pure photon state interacts with environments where photons are experiencing phase shifts and photon loss. Then, the photons are passed to photo-detectors. The final detection provides phase information and resolution. It is obvious that most critical events occur in a stage containing photon interactions with environment. The phase shift we are trying to measure comes in here. The troublesome photon losses also happen in that stage. Thus, we set a first dividing line at a point where pure state photons start interacting with environment. Figure 13 describes this segmentation of the problem. With this configuration, a big picture can be drawn in terms of how the numerical computations need to be set up, i.e., generate entangled photons, produce a pure state, and measure the phase sensitivity. In a real system, these series of events occur in the forward direction. However, we have a certain goal to achieve high phase sensitivities. Therefore, numerically, the system progresses in inverse direction, i.e., set a desired sensitivity (a minimum constraint), seek a pure state that produces such an outcome, and find a condition of the photon source generation and operation that produce that

pure state. Eventually, numerical tools we are developing become an inverse problem solver where the target physical qualities are given as an input. As we know now, it is maximum phase sensitivity. Then, optimum pure states are computed as an output for inversely arranged "Operation module". The optimum pure states become an input to inverse "Source module". To this end, first, a forward problem solver is developed for each main module. Next, an inverse problem solver is made using a forward problem solver.

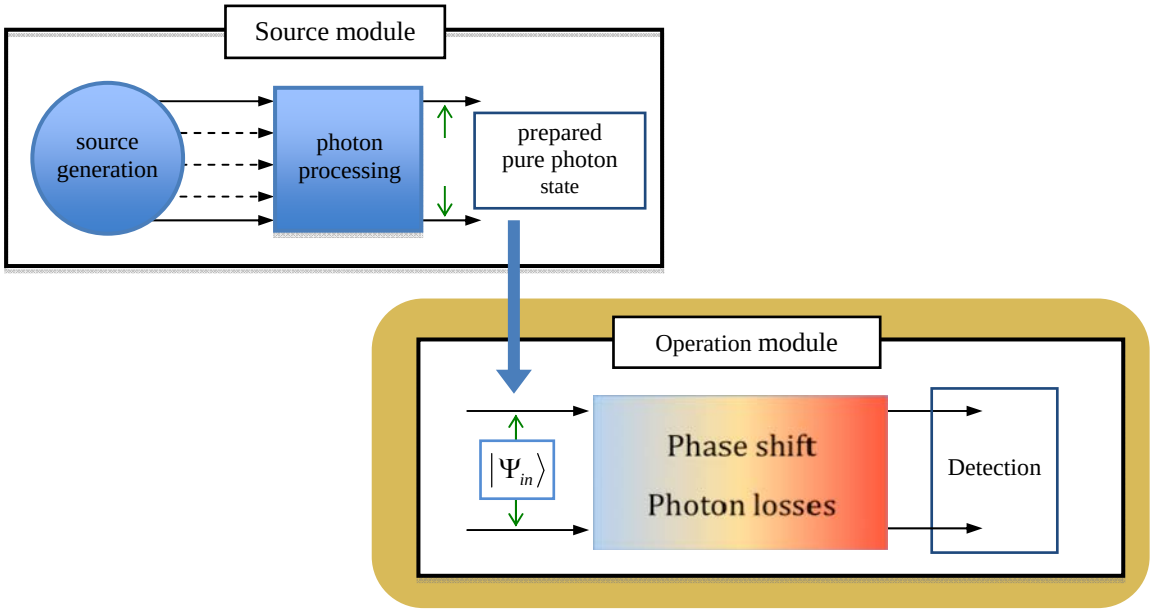

Figure 13: Workflow from Source Module into Operation Module

At the current stage, we are focusing on "Operation module" in Fig.13. In other words, we assume that a pure photon state has been produced. Numerical computation starts from having pure photon states. In the given system, photons are supposed to select two paths of propagation. One path is dedicated to detection of scattering objects where phase shifts occur, along with photon losses due to environmental factors and finite scattering cross-sections of the object. The other path is assigned for reference beam that will interfere at the detector site with photons passing through the detection path. Since the reference path is not to be disturbed by outside environment, we have full control of phase shift and losses occurring during photon propagation. What eventually we measure at the detector is the phase shift and the phase fluctuation associated with the conditions in outside environment. We measure differences in phase between photons passing through detection path and reference path. Therefore, overall phase shift can be represented by

$$\varphi = \varphi_A - \varphi_B, \tag{36}$$

where φ_A and φ_B denote phase shifts in detection and reference paths, respectively. Since φ_B is tunable, φ is also a tunable quantity. One can tune this to achieve maximum phase sensitivities.

At the detector, we also estimate phase uncertainty, $\delta\varphi$, which is inversely proportional to phase sensitivity.

This overall process is numerically implemented as a main module starting from pure photon states to detection. This main module consists of four submodules. The first submodule is for constructing density matrix of an input pure photon state. Here, the numerical code simply performs the following calculations from probability amplitudes given in the form of superposition of eigenstates, $|\Psi_{in}\rangle = \sum_{i=0}^{N} c_i |N-i,i\rangle$. We choose the eigenstate to be a *correlated Fock state*.

$$(\hat{\rho}_{in})_{m,n} = c_m c_n^* \tag{37}$$

The resulting input density matrix is passed to a phase-shift module that shifts the phase depending on state number differences.

$$(\hat{\rho}_{\varphi})_{m,n} = e^{i(m-n)\varphi}(\hat{\rho}_{in})_{m,n} \tag{38}$$

When pure states experience photon loss, the number of photons lost spans from zero to the total number of initial photons. The input pure state hence changes to a mixed state. To take that change into account, a density matrix after the loss contains all possible cases of pure density matrices with different number of photons, as discussed in Sec.6.0. It turns out that the lossy density matrix forms a block diagonal matrix where each diagonal block represents a pure density matrix with reduced total photon numbers. A generalized formulation is set up for this protocol based on photon losses by partial reflection and transmission in a beam splitter at each photon path. The resulting equation is as follows.

$$(\hat{\rho}_{loss})_{N,L,i,j} = \sum_{m=0}^{L} (c_{i+m} c^*_{j+m}) A_{i+m} B^*_{j+m} \tag{39}$$

$$A_k = \sqrt{{}_{N-k}C_{N-L-i}}\; t^{N-L-i}\, r^{L+i-k} \sqrt{{}_{k}C_{i}}\; t'^{i}\, r'^{k-i} \tag{40}$$

$$B_k = \sqrt{{}_{N-k'}C_{N-L-j}}\; t^{N-L-j}\, r^{L+j-k} \sqrt{{}_{k'}C_{i}}\; t'^{j}\, r'^{k-j} \tag{41}$$

Here, N and L denote the number of photon at input and L^{th} block, also number of photon losses ($L = 0,\ldots,N$), respectively. Here, the indices i and j are the $(i\ ,\ j)^{\text{th}}$ component of the L^{th} block. The (t, r) and (t', r') represent complex valued transmission and reflection coefficient of beam splitters in detection and reference path.

For the detection scheme, we calculate the Fisher information, F, from probabilities of coincident detection, P [Uys2007]. The Fisher information carries both super-resolution and super-sensitivity information about the state. The larger the Fisher information, the more likely the state is to be super-resolving and super-sensitive. The phase sensitivity becomes:

$$\delta\varphi^2 = \frac{1}{F\left[=\sum_{L=0}^{N}\sum_{m=0}^{N-L} P_m\left(\frac{\partial \ln P_m}{\partial\varphi}\right)^2\right]} \quad . \tag{42}$$

The overall procedure of the operation module serves as forward problem solver from which phase uncertainties are calculated by given input pure photon states. This forward problem solver is summarized in Fig.14.

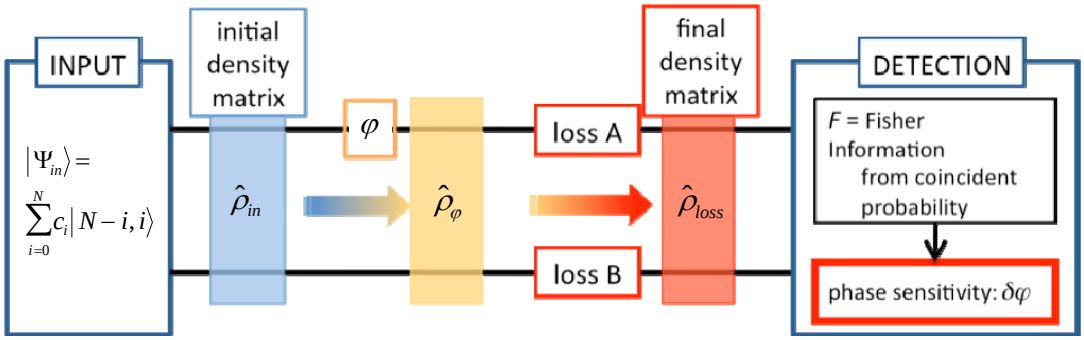

Figure 14: Schematic of Forward Problem Solver for Operation Module

For verification, the forward problem solver is implanted to obtain phase sensitivities for M&M and N00N input states [Huver2008]. Analytically calculated results are compared with the solutions of the forward problem solver. Figure 15 shows good agreements, indicating the code recovers known analytic results in the limit of low loss.

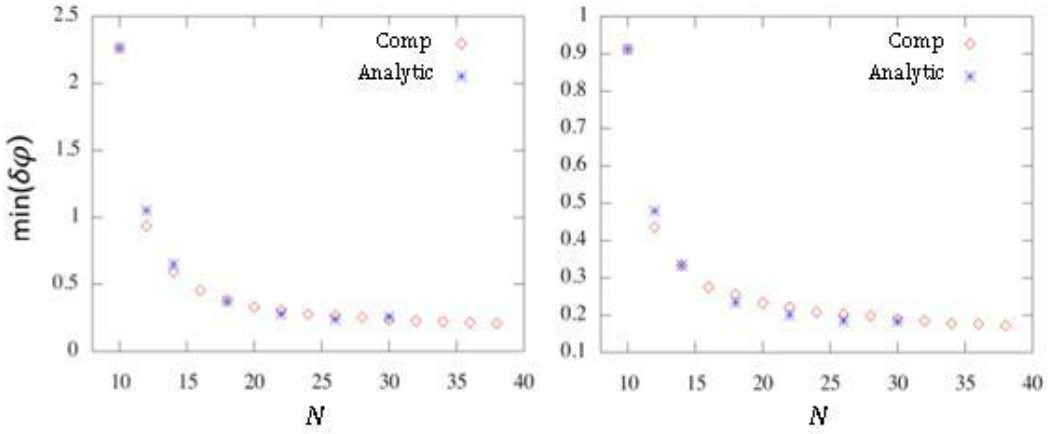

Figure 15: Minimum Phase Sensitivity for M&M State with 40% and 50% Loss

The resulting phase sensitivities depend on the configurations of the input pure state. In other words, input states need to be optimized to produce the possible minimum phase uncertainty. For this purpose, the forward problem solver needs to be converted to an inverse problem solver. There are several standardized computer routines that minimize or maximize any parameterized arbitrary functions. In our case, the forward problem solver is the function that has input state coefficients as parameters. We implement a genetic algorithm and a simulated annealing algorithm. The forward problem solver developed above is directly applied to this optimization routine; completing the inverse problem solver. A workflow chart is shown in Fig.16. In the inverse problem solver, we direct the computer program to find minimum $\delta\varphi$ for given phase shift and input state as parameters which are to be determined. Losses on both paths are treated as fixed parameters. The inverse problem solver determines optimum states for each photon loss in the following procedure: An optimization routine generates input states. The forward solver produces output. Then, the output is sent to feedback procedures where new improved input states are generated. These procedures are repeated until no further improvement in phase sensitivity is seen. After that, inverse solver returns final results that include an optimum input state and phase as well as a maximized phase sensitivity value. This optimization processes are shown in Fig.16. Eventually, the code will provide trends and characteristics of required input states for given loss values and total number of photons. Ultimate limits in phase sensitivities are obtained simultaneously.

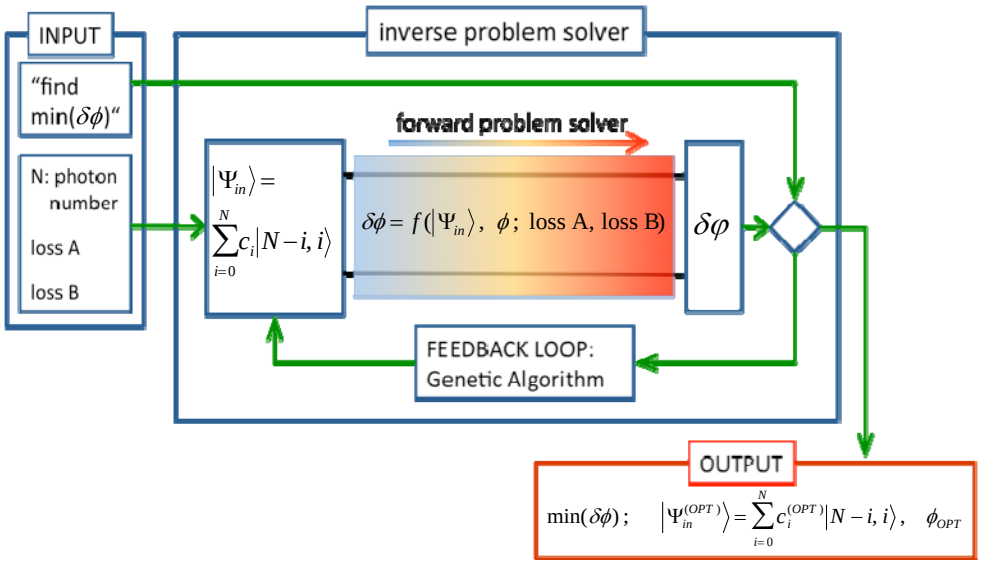

Figure 16: Schematic Workflow of Inverse Problem Solver

4.3 Optimization

We have a completed and verified forward problem solver. A genetic algorithm module is also completed and tested with lossless cases that have known solutions. The optimization code produced the results that agree well with theoretical expectation, i.e., maximum phase sensitivity at N00N state with phase fluctuations following *1/N*, i.e., Heisenberg limit. Then, the optimization code of loss cases is developed. Although robustness of the genetic algorithm is well known, we also developed another optimization program based on a simulated annealing algorithm. Then, we use those two methods in order to test the validity of optimization results obtained from both methods. For a given identical configuration, such as the same loss and photon numbers, two methods independently optimize the system. The optimization results are crosschecked with each other to see if they produce consistent results. As shown in Fig.17, minimum phase fluctuations are essentially same indicating accuracy for both methods.

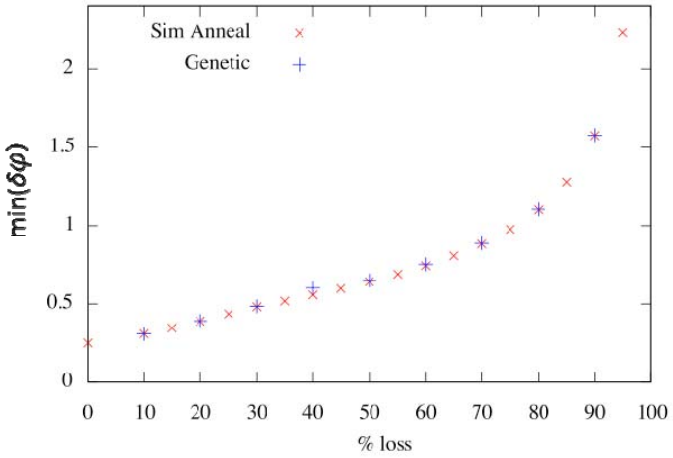

Figure 17: Comparison of Simulated Annealing and Genetic Algorithm

Next, we estimate phase sensitivities as a function of losses and compare for different input photon numbers. Figure 18 (a) and (b) show log scale plots of phase sensitivity as a function of loss in a dB scale. We choose input photon numbers N = 1, 3, 4, and 6.

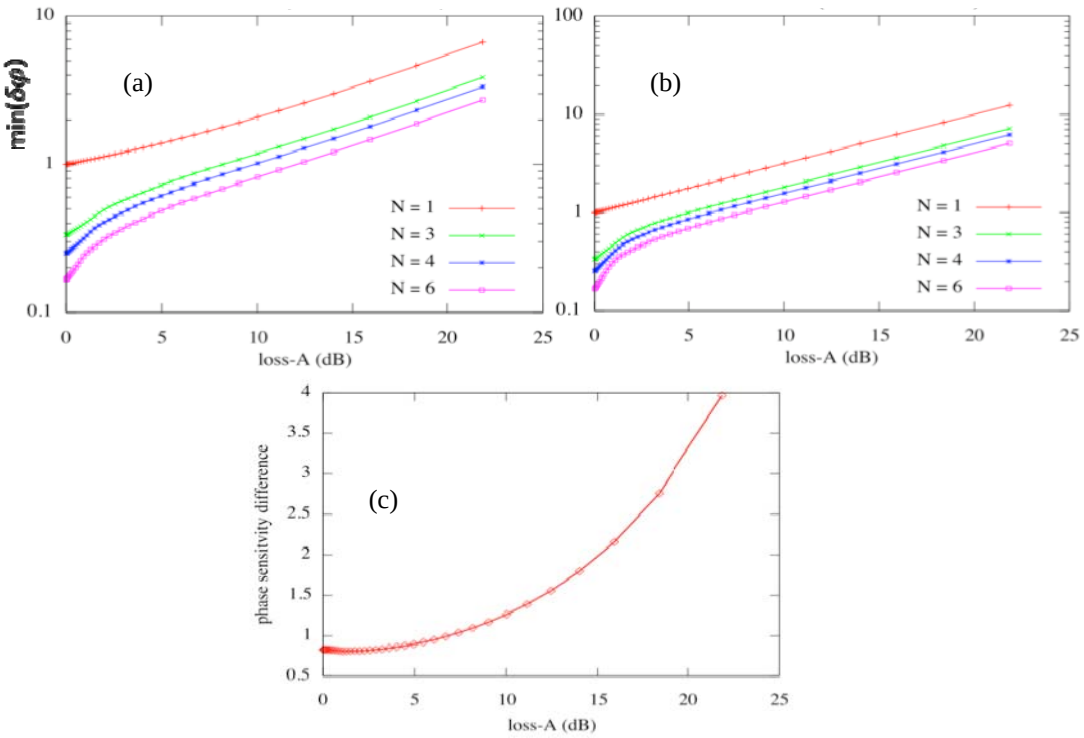

Figure 18: Minimum Phase Fluctuation for N=1,3,4,6

Two loss configurations are considered, one for loss in one photon path (Loss B = 0), Fig.18(a), and the other for the same losses in both paths (Loss A = Loss B), Fig.18(b). As expected, adding more photons improves phase sensitivity. In order to quantitatively estimate the improvements on phase sensitivity by adding more photons into the system, differences in minimum phase fluctuation between single photon and six photon cases ($= \delta\varphi_{N=1} - \delta\varphi_{N=6}$) are computed and presented in Fig.18(c). One can clearly observe that phase sensitivity improvements are more evident at a large amount of losses. It is also found that having loss in only one path produces better phase sensitivities for all N then losses in both paths.

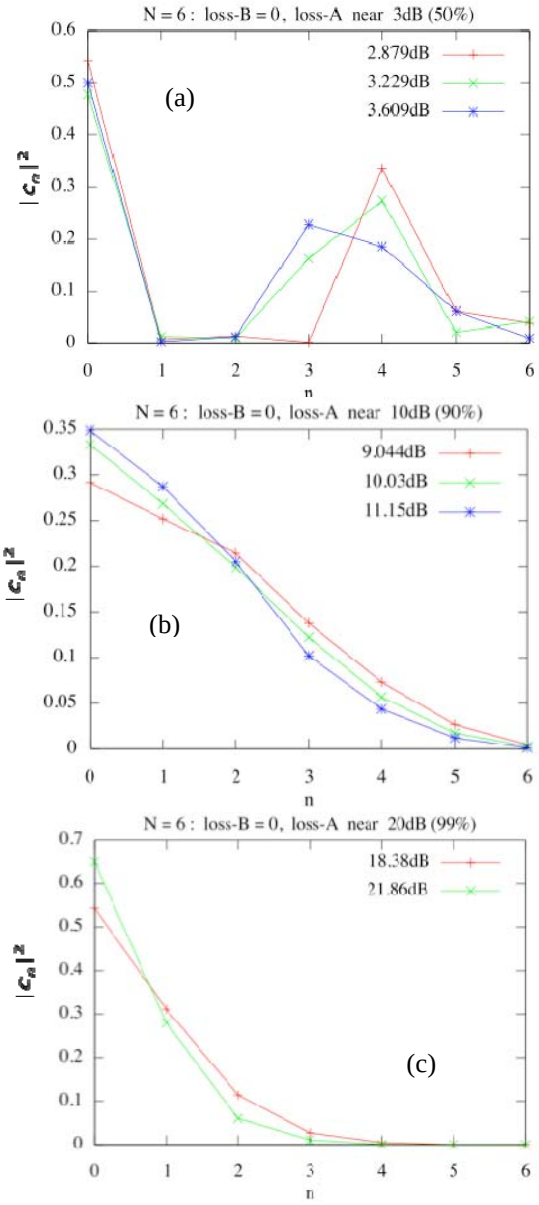

Figure 19: State Coefficient Distributions of Optimized Input Photon Configurations for N = 6 for 3dB, 10dB, and 20dB.

Another feature that the numerical code can provide is information of how input state photons are configured to produce best performance in phase measurements. This is critical when one tries to realize a quantum LIDAR system. Once we have information of the desired photon state configurations, efforts should be focused on how to generate such photon states. For the demonstration, we chose N = 6 and losses near 3 dB, 10 dB, and 20 dB. Loss is assigned in one path, specifically Loss-B = 0. Figure 19 shows a trend of optimized photon state configurations for loss increments. The squares of absolute values of the state coefficient, $|c_n|^2$, where c_n are from Eq.37, are presented. In the previous study, we have confirmed that N00N states are the optimal state for lossless case. Starting from N00N state, not shown here, population or amplitude distribution of eigenstates are moving toward $N = 0$ that corresponds to the eigenstate $|N, 0\rangle$ as loss is decreased.

4.4 Further Discussion

In Fig.18, it can be seen that phase uncertainty plots for loss-A become linear in log-log scale for high loss region (loss > 10 dB or 90% loss). The slopes of those lines also become parallel to each other. For the general comparison, we modified Eq.42 by normalizing F with the total input photon number N and then recalculate $\delta\varphi$, which we define as the normalized phase uncertainty. The results presented in Figures 20 and 21 show that the curves for different N overlap each other for losses greater than 15 dB, while low-loss cases exhibit some level of N dependency — the lossless case $\delta\varphi$ follows the Heisenberg limit, $1/N$, and this dependency gradually changes to $1/\sqrt{N}$ as loss is increased. From this, combined with Eq.42, the following equation can be derived for high loss region.

$$\delta\varphi_N \approx \frac{\delta\varphi_{N=1}}{\sqrt{N}} \quad . \tag{43}$$

One interesting observation can be noted. The factor $\delta\varphi_N$ is inversely proportional to $\sqrt{N}$, which is similar behavior seen in coherent state. The apparent difference is the fact that coherent state $\delta\varphi$ follows mean photon number $\sqrt{\overline{N}}$.

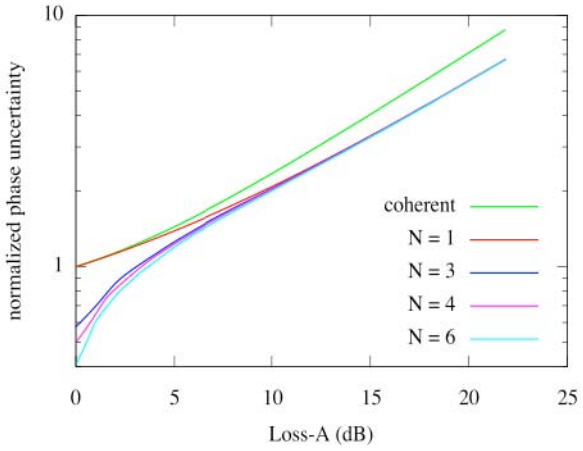

Figure 20: Log-Log Plot of Phase Sensitivity by Normalized Fisher Information

Even with its similarity, we note that it is not necessary to conclude that the same phase sensitivity between coherent state and correlated Fock state in the limit of high loss. The upper most line in Figures 20 & 21 is normalized phase uncertainty computed for coherent state. The normalized phase uncertainty presented here is based on classical homodyne LIDAR setup. For the quantitative comparison, we applied quantum theory that is correspondingly related to classical LIDAR system as follows.

In the lossless case, the coherent state exhibits the same phase uncertainty as the $N = 1$ case. Then, as loss increases, it maintains a higher slope compared to $N = 1$, but a lower slope than $N > 1$ correlated Fock states in low loss region. In the middle loss region, 7 dB ~ 10 dB, slopes are similar between coherent and $N > 1$ cases. When losses are increased further to extreme region, loss > 10 dB, the slope for coherent state becomes higher than that of correlated Fock states. *This indicates that improvement in phase sensitivity given by correlated Fock state over coherent state becomes much higher in extreme loss scenario, but that dual mode coherent state is comparable in performance.*

The Eq.43 is useful for the quick estimation of $\delta\varphi$ for high loss cases. The potential problem for this quick estimation is finding a loss region that can be considered as "high loss" to be safe to use with Eq.43. From careful observations of numerical computations, we find that the minimum bound of a high loss region increases as N increased. For example, 15 dB for $N = 6$ changes to 20 dB for $N = 20$ with 99% convergence to exact solutions. Depending on desired accuracy, this minimum loss bound can be applied more generously. We note that, even for the high loss region, the rigorous computations are still needed to acquire optimized input state, see Fig.19 for example, for use in the source module or input photon preparation.

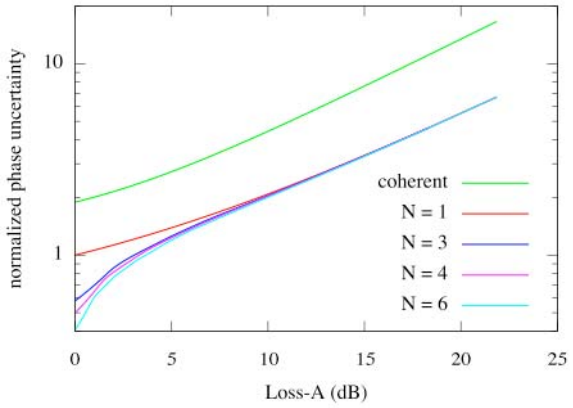

Figure 21: Log-Log plot of Phase Sensitivity by Normalized Fisher Information (Coherent State: 28% Photodetector Efficiency is Assumed)

Now, we have a complete numerical code for the operation module. We have chosen a modular based coding approach for the numerical code development. Thus, this code is highly mutable such that, if any, better systems of ideas can easily be adopted that can occur in future research progress. Currently, this numerical tool was successfully applied to analyze phase sensitivities under lossy environments in the quantum LIDAR system utilizing correlated Fock states. We provided the system performance on the total input photon number and losses. From the analysis, we found that adding more numbers of photons improves the phase sensitivities dramatically. The phase sensitivity of the lossless system shows $1/N$ dependency. As loss increased, the dependency deviates from $1/N$, and then it slowly changes into $1/\sqrt{N}$ for high loss. Additional work shows that for high-loss the two mode coherent state performs with the same scaling law as the dual Fock state. The numerical code also provides optimized input state configurations. This will provide critical information on how photons need to be processed in the source stage. For further work, the numerical method for the source module will continue to be developed. Upon having a full numerical package, the overall research will be expedited and transformation from theory to design and fabrication of real tangible devices will become easier.

5.0 MIE SCATTERING AND PHOTON NUMBER RESOLVING DETECTORS

5.1 Introduction

In Sec.2.0, above, we outline a protocol for quantum LIDAR that is super-resolving, shot-noise limited, and shows a huge signal-to-noise discrimination for determining a phase shift. This scheme relies crucially on the properties of number-resolving detectors. A simple experimental proof of principle using such detectors was carried out by our team members and the group of Alan Migdall at NIST, Gaithersburg, where such detectors have been in use for some time now.

5.2 Mie-Scattering and Photon-Number Resolving Detection

Based on the Gedanken experiment about Mie scattering presented at the QSP Park City program review meeting, we were able to work out the details for quantum Mie scattering and turn the original question into a promising quantum sensor. We replaced the classical three-dimensional Mie scattering problem by a one-dimensional Fabry-Perot transmission calculation that is carried out fully quantum mechanical. From our quantum Mie scattering model we infer, that single-mode quantum states of light such as Fock states, exhibit the same transmission functions as single mode laser light, if an ordinary intensity measurement is carried out. However, *if a photon-number resolving measurement is carried out instead*, we observe narrower transmission functions than for the classical case. This feature results in a higher resolution of the Fabry-Perot interferometer. *We also show that the sensitivity for measuring a length change, or equivalently an unknown phase shift, of the interferometer is improved.* The theoretical study has been written up in form of a manuscript and has been submitted for publication after DARPA has been approved the work for public release.

5.3 Interferometry with a Transition Edge Sensor

In collaboration with the optical technology laboratory of A. Migdall at the National Institute for Standards and Technology in Gaithersburg, MD, we have been working on an experimental verification of our proposed sensor. At NIST we have access to a Transition Edge Sensor (TES), which allows us to implement the photon number resolving detection scheme with a quantum efficiency of approximately 95%. In a first step we confirmed our theoretical model for weak coherent light incident on a Michelson as well as on a Fabry-Perot interferometer. We verified experimentally the photon-number resolved statistics with a weak coherent laser beam incident on a Michelson interferometer (Fig.22), and Fabry-Pérot interferometer (FPI) (Fig.23).

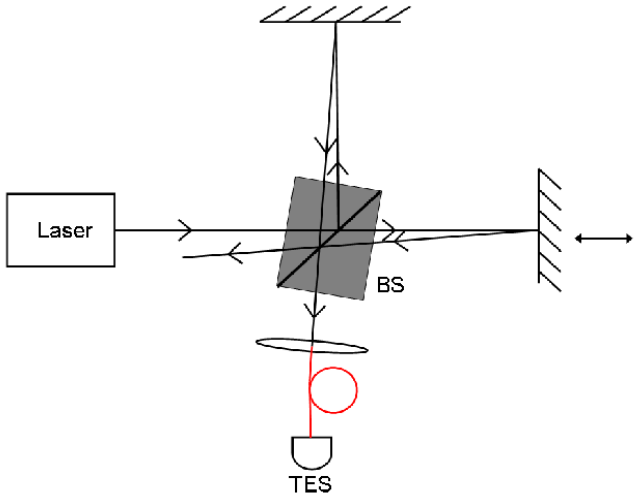

Figure 22: Setup for the Michelson Interferometer with TES Detector

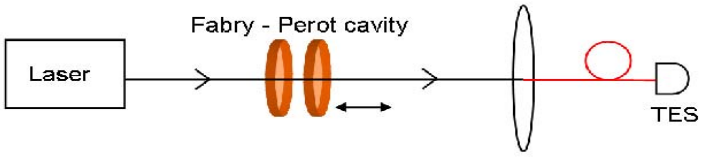

Figure 23: Setup for the Fabry-Pérot Transmission Experiment

A coherent laser beam at λ=850 *nm*, a repetition rate of 50 kHz, and a pulse duration of 50 ps is attenuated to have the average photon number to be ≈4 as detected by our photon-number resolving TES detector [Lita2008]. As can be seen in Fig.24, our preliminary results agree with the theory and also confirm a previous investigation by Khoury *et al.* who also used coherent light, but a polarization Mach-Zehnder interferometer, and a visible light photon counter (VLPC) [Khoury2006].

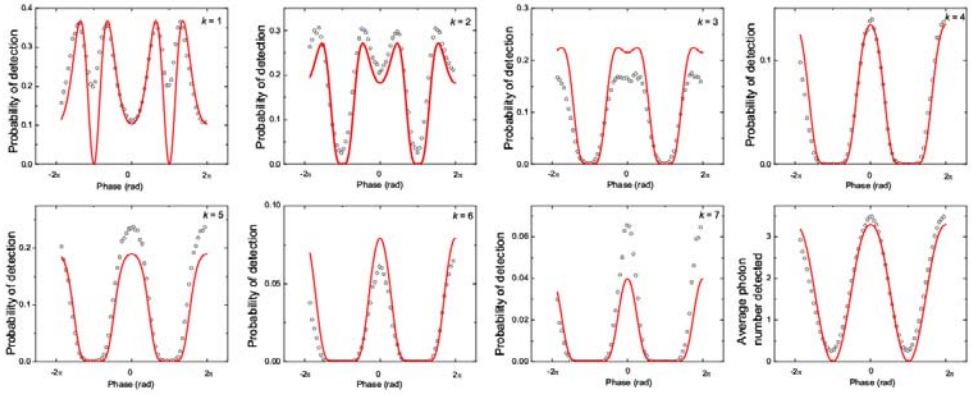

Figure 24: Measurement of the photon-number resolved interference fringes for a weak coherent state with $|\alpha|^2 \approx 4$

Similar features to the one observed with the MI may be obtained for a weak coherent laser beam incident on a Fabry-Pérot interferometer. The number resolved output of the FPI shows narrower transmission functions than for the average photon-number detection. (Fig.25.)

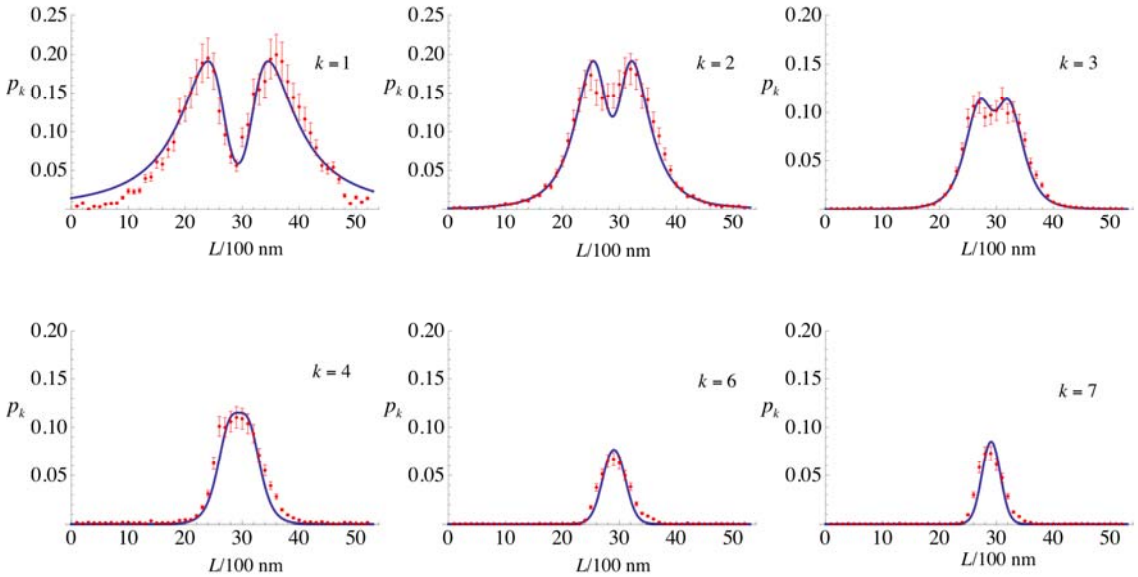

Figure 25: Measurement of the Photon-Number Resolved Transmission Probabilities p_k for a Weak Coherent State with $|\alpha|^2 \approx 4$

However, the compression of the interference fringes does not improve the sensitivity of the device since it amounts to just taking the N^{th} power of the light intensity, which is basically equivalent to a classical post-processing of the data [Giovannetti2008]. To obtain an improved resolution and sensitivity of the interferometer, we need to either send nonclassical light through the FPI or keep the classical input, but enable a complicated entangling measurement [Resch2007].

We follow the first approach and show that sending *N*-photon states through the FPI and observing the *N*-photon resolved transmitted light, results in beating the standard quantum (shot noise) limit. To calculate the transmission functions for quantum states of light, we use a fully quantized approach for the FPI. Loudon first considered a quantum theory of the FPI in the context of high-resolution length measurements [Ley1987]. We show that Loudon's results can be nicely related to an effective beam splitter transformation. The two incoming and two outgoing modes of the FPI can be quantized as displayed in Figs. 27 and 28.

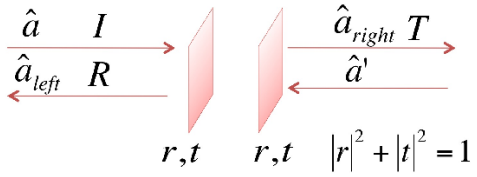

Figure 26: Fabry-Pérot Mirrors with Complex Amplitudes i, r, and t, for Incoming, Reflected and Transmitted Modes, Respectively

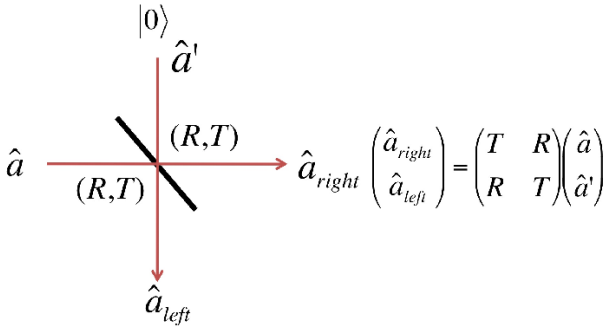

Figure 27: Effective Beam Splitter for the Fabry-Pérot Cavity with Complex Amplitudes I, R, and T, for Incoming, Reflected and Transmitted Modes, Respectively

It is now seen that the modes as described in Figs. 27 and 28 are transformed by an effective beam splitter transformation. Figure 29 shows the theoretical results for a weak coherent state with average photon number $|\alpha|^2=2$ and a two-photon state $|2\rangle$ compared to the classical transmission function.

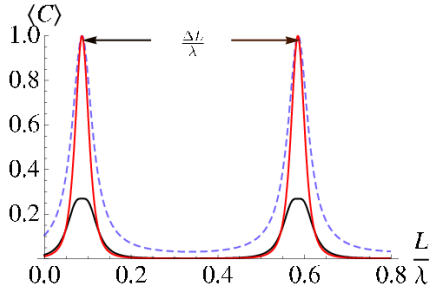

Figure 28: Transmission Function for a Single-Mode Coherent State and an Ordinary Intensity Measurement (Dashes).

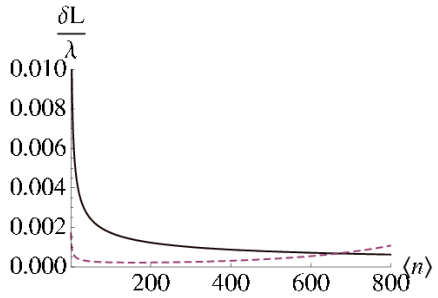

Figure 29: Comparison of the Sensitivity δL/λ for a Coherent State (Solid Line) Versus an N-Photon State with N-Photon Resolving Measurement as a Function of the Photon Number

The results for the sensitivity of a coherent state versus an *n*-photon state incident on the FPI (Fig.29) show that a length measurement with *n*-photon states instead of coherent states provides us with a much smaller uncertainty δL in the few photon limit. Hence, the sensitivity of the FPI is increased. However, for large photon numbers the coherent state outperforms *n*-photon states with *n*-photon detection. The experimental verification of this effect is currently in progress.

The proposed Fabry-Perot interferometer with quantum states of light and a photon number resolving detection scheme may find applications for high precision length measurements as, e.g., at the laser interferometer gravitational wave observatory (LIGO) or on space based platforms, where only a limited amount of loss is present. We are also investigating different quantum states and adaptive measurement schemes to compensate for larger loss. We determine the possible ranges for stand-off applications of this quantum sensor.

6.0 THEORY OF QUANTUM STATE PROPAGATION THROUGH ATMOSPHERE

6.1 Overview

Work at MathSense Analytics (MSA) has concentrated on analytical and modeling studies of the propagation and target interaction of non-classical photon states, and the mathematical analysis of optimization techniques to single out the "best" class of light states for various end-result performance goals.

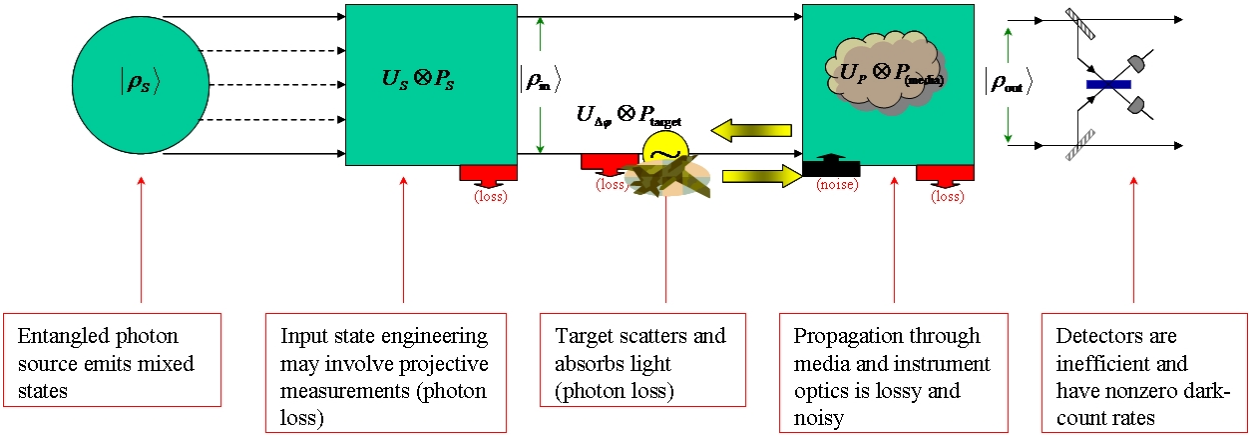

Figure 30: An Overview of the Various Quantum-State-Engineering Problems Studied by the LSU Team During Phase I

Specifically, the mathematical analysis of the reflection and scattering of general entangled pure states of light by the target has been carried out. We developed models of absorption and reflection of dual-channel entangled light states by the propagation medium and the target. This effort was coordinated with the OPA-driven input-state production work undertaken by the LSU group. In particular, realistic N00N-like states produced by OPAs coupled to number-resolving detectors (via projective measurement) are more complicated, and have to be subjected to the same loss models developed for the propagation and target interaction of pure N00N states. A sufficiently realistic model of the photon states as well as the target-surface characteristics will ultimately allow an examination of the extent to which non-classical features can be expected to be resilient to loss. MSA has also examined the question of which quantum states are optimally robust against degradation due to loss via target reflection and scattering processes. This optimization work was then coupled with the question of optimizing the ultimate sensitivity (or signal-to-noise) of the quantum sensor at the detector end. Eventually, these techniques will have to be generalized to treat mixed states, and the mathematical framework has being developed with sufficient generality to handle this extension. In addition, the mathematical techniques which so far in Phase I have been restricted to single or dual-mode photon propagation will have to be extended to multi-mode propagation to model realistic, finite-sized beams of non-classical light with physical (e.g. Gaussian) beam characteristics. The groundwork for this extension has also been established in Phase I.

6.2 Beer-Lambert Law for Lossy Propagation of Non-Classical Light

Starting from first principles, we derived the lossy propagation law (generalization of the Beer-Lambert law for classical radiation loss through the atmosphere or fiber) for non-classical, dual-mode entangled states.

We investigated the behavior of loss as a function of propagation distance for various classes of entangled states. Focus was on loss of coherence and loss of entanglement during propagation. The final results are expressed in terms of classical characteristics of the propagation medium such as the Beer-Lambert loss coefficient μ.

The lossy propagation law (generalization of Lambert-Beer's law for classical radiation loss) for non-classical, dual-mode entangled states is derived from first principles, using an infinite-series of beam splitters to model continuous photon loss, as depicted in Figure 31. This model is general enough to accommodate stray-photon noise along the propagation, as well as photon loss. An explicit analytical expression for the density matrix as a function of propagation distance is obtained, not only for specific input states such as N00N and *m*-and-*m* states, but also for a completely general input where the only restriction is that the maximum photon number in each mode is limited to *N*.

The result is analyzed numerically for various examples of input states. For N00N state input, the loss of coherence is super exponential as predicted by a number of previous studies. However, for generic input states, where the coefficients are generated randomly, the decay of coherence is very different; in fact no worse than the classical Beer-Lambert law. More surprisingly, there is a plateau at a mid-range interval in propagation distance where the loss is in fact sub-classical, following which it resumes the classical rate.

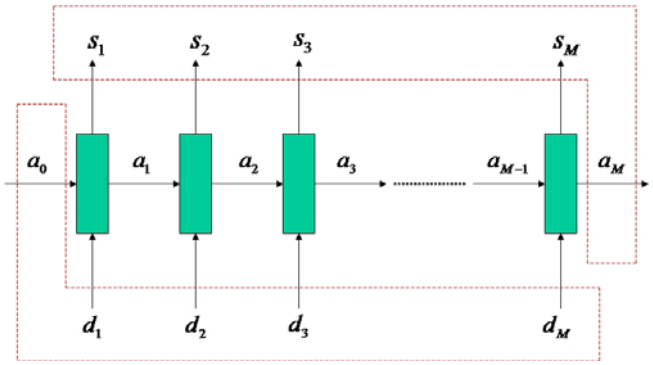

Figure 31: The Infinite-Series-of-Beam-Splitters Model for the Analysis of Lossy Propagation of Non-Classical Light States

These preliminary results indicate that the super-exponential loss behavior of N00N states is highly non-generic, and not likely to be shared by generic entangled states in the larger Hilbert space of the dual photon channel. Assuming even part of the coherence of a generic state can be utilized to produce super-classical phase sensitivity using an appropriate detection scheme, there appear to be many candidate states which are both robust against decoherence and non-classical enough to achieve the DARPA criteria for quantum sensors. This is consistent with and a generalization of previous results involving M&M states.

The basic model is described in Figure 31. We assume that the input modes are $a_0, d_1, d_2, \ldots, d_M$, and the output modes are $a_M, s_1, s_2, \ldots, s_M$. Unitarity at each fictitious beam splitter *k* requires:

$$\left.\begin{aligned} a_k &= Ta_{k-1} + Ld_k \\ s_k &= La_{k-1} + Td_k \end{aligned}\right\} \quad k = 1, 2, \ldots, M \qquad \begin{aligned} |L|^2 + |T|^2 &= 1 \\ L\overline{T} + T\overline{L} &= 0 \end{aligned}$$

In terms of the creation operators a_k^+, d_k^+, s_k^+, we can write this in the form

$$\left.\begin{aligned} a_k^+ &= \overline{T}a_{k-1}^+ + \overline{L}d_k^+ \\ s_k^+ &= \overline{L}a_{k-1}^+ + \overline{T}d_k^+ \end{aligned}\right\} \quad k = 1, 2, \ldots, M$$

The in and out modes are then connected by an overall unitary matrix:

$$\begin{bmatrix} a_0^+ \\ d_1^+ \\ d_2^+ \\ d_3^+ \\ \vdots \\ d_M^+ \end{bmatrix} = U \begin{bmatrix} a_M^+ \\ s_1^+ \\ s_2^+ \\ s_3^+ \\ \vdots \\ s_M^+ \end{bmatrix} \qquad U^+U = I$$

Furthermore, unitarity relations at each beam splitter uniquely determine the form of the large $(M+1)\times(M+1)$ unitary matrix *U*:

$$\begin{bmatrix} a_0^+ \\ d_1^+ \\ d_2^+ \\ d_3^+ \\ \vdots \\ d_M^+ \end{bmatrix} = U \begin{bmatrix} a_M^+ \\ s_1^+ \\ s_2^+ \\ s_3^+ \\ \vdots \\ s_M^+ \end{bmatrix} \qquad U = \begin{bmatrix} T^M & L & LT & LT^2 & \cdots & LT^{M-1} \\ LT^{M-1} & T & L^2 & L^2T & \cdots & L^2T^{M-2} \\ LT^{M-2} & 0 & T & L^2 & \cdots & L^2T^{M-3} \\ LT^{M-3} & 0 & 0 & T & \cdots & L^2T^{M-4} \\ \vdots & \vdots & \vdots & \vdots & \ddots & \vdots \\ L & 0 & 0 & 0 & \cdots & T \end{bmatrix}$$

One can check explicitly that

$$\left.\begin{array}{l} |L|^2 + |T|^2 = 1 \\ L\overline{T} + T\overline{L} = 0 \end{array}\right\} \qquad \Rightarrow \qquad U^+U = I$$

Since

$$a_0^+ = T^M a_M^+ + Ls_1^+ + LTs_2^+ + LT^2 s_3^+ + \cdots + LT^{M-1} s_M^+$$

An input Fock number state

$$|\psi_{\text{in}}\rangle = |N\rangle = \frac{1}{\sqrt{N!}} (a_0^+)^N |0\rangle$$

leads to the output state

$$|\psi_{\text{out}}\rangle = \frac{1}{\sqrt{N!}} \left(T^M a_M^+ + Ls_1^+ + LTs_2^+ + LT^2 s_3^+ + \cdots + LT^{M-1} s_M^+ \right)^N |0\rangle$$

from which the final density matrix output should be calculated by tracing out the loss degrees of freedom:

$$\rho_{\text{out}} = \text{Tr}_{\{s_1,\ldots,s_M\}} |\psi_{\text{out}}\rangle\langle\psi_{\text{out}}|$$

This calculation gives

$$\rho_{\text{out}} = \text{Tr}_{\{s_1,\ldots,s_M\}} |\psi_{\text{out}}\rangle\langle\psi_{\text{out}}|$$

$$= \sum_{\left\{ \begin{array}{c} n_0,\ldots,n_M = 0 \\ \sum n_\alpha = N \end{array} \right\}}^{N} \frac{N!}{n_0! n_1! \ldots n_M!} |T|^{2n_0 M} |T|^{2\sum_{i=1}^{M}(i-1)n_i} |L|^{2\sum_{i=1}^{M} n_i} |n_0\rangle_{s_0} \langle n_0|_{s_0}$$

where we adopted the notation $s_0 \equiv a_M \quad \Rightarrow s_0^+ = a_M^+; \quad |k\rangle_{s_0} \equiv |k\rangle_M$. This result can be manipulated combinatorially to yield the expression

$$\rho_{\text{out}} = \sum_{n_0=0}^{N} \frac{N!}{n_0!(N-n_0)!} \left|n_0\right\rangle_{s_0} \left\langle n_0\right|_{s_0} \sum_{\left\{\sum_{k=1}^{M} n_k = N-n_0\right\}}^{N-n_0} \frac{(N-n_0)!}{n_1! n_2! \ldots n_M!} |T|^{2n_0 M} |T|^{2\sum_{i=1}^{M}(i-1)n_i} |L|^{2\sum_{i=1}^{M} n_i}$$

The Beer Limit:

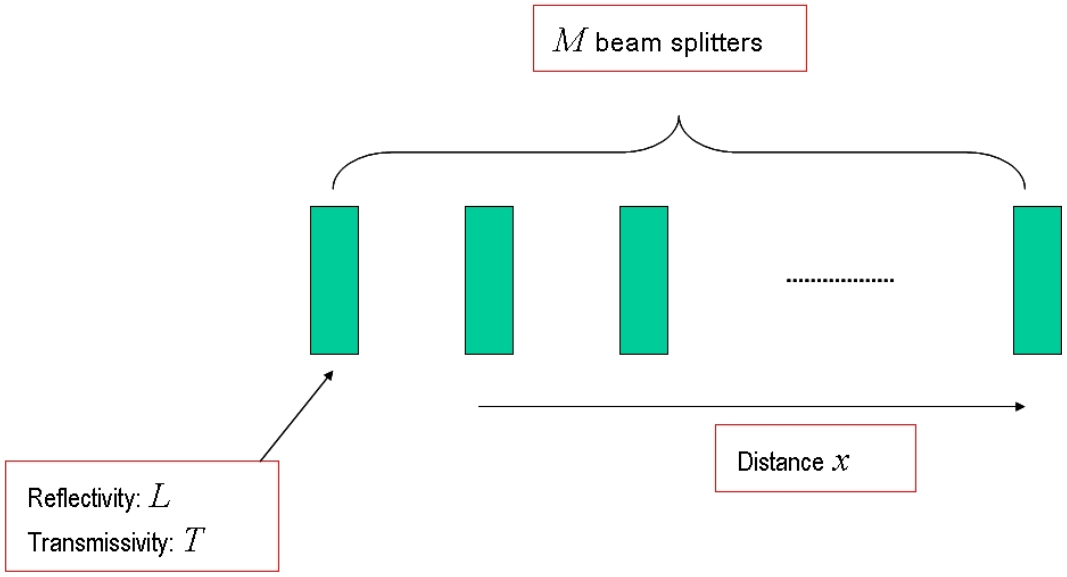

Figure 32: The Beer Limit for the Infinite-Chain-of-Beam-Splitters Model

To implement the Beer limit (transition to the continuum limit), we use the following schemes: For the modulus (amplitude) as a function of propagation distance

Modulus

$$\begin{cases} M \to \infty \\ L \to 0 \\ |L|^2 \dfrac{M}{x} \quad \to \quad \text{constant} \equiv \mu \\ |T|^{2M} = (1-|L|^2)^M \to \left(1 - \dfrac{\mu x}{M}\right)^M \to e^{-\mu x} \end{cases}$$

For the phase (of the complex transmission coefficient) as a function of propagation distance

$$\text{Phase} \begin{cases} M \to \infty \\ T = |T| e^{i\eta_0} \\ \eta_0 \to 0 \\ \eta_0 \dfrac{M}{x} \;\; \to \;\; \text{constant} \equiv \eta \\ T^M = |T|^M \; e^{i\eta x} \end{cases}$$

The Beer limit turns

$$\rho_{\text{out}} = \sum_{n_0=0}^{N} \frac{N!}{n_0!(N-n_0)!} \left| n_0 \right\rangle_{s_0} \left\langle n_0 \right|_{s_0} \sum_{\left\{ \substack{n_1,\ldots,n_M=0 \\ \sum_{k=1}^{M} n_k = N-n_0} \right\}}^{N-n_0} \frac{(N-n_0)!}{n_1! n_2! \ldots n_M!} |T|^{2n_0 M} |T|^{2\sum_{i=1}^{M}(i-1)n_i} |L|^{2\sum_{i=1}^{M} n_i}$$

into the x-dependent output density matrix resulting from an input Fock number state with N photons given by

$$\rho_{\text{out}}(x) = \sum_{n=0}^{N} \binom{N}{n} e^{-n\mu x} (1 - e^{-n\mu x})^{N-n} \left| n \right\rangle \left\langle n \right|$$

This is our final result for the lossy propagation of single-mode number states.

6.3 Beer's Law for the Propagation of Dual-Mode Entangled N00N States

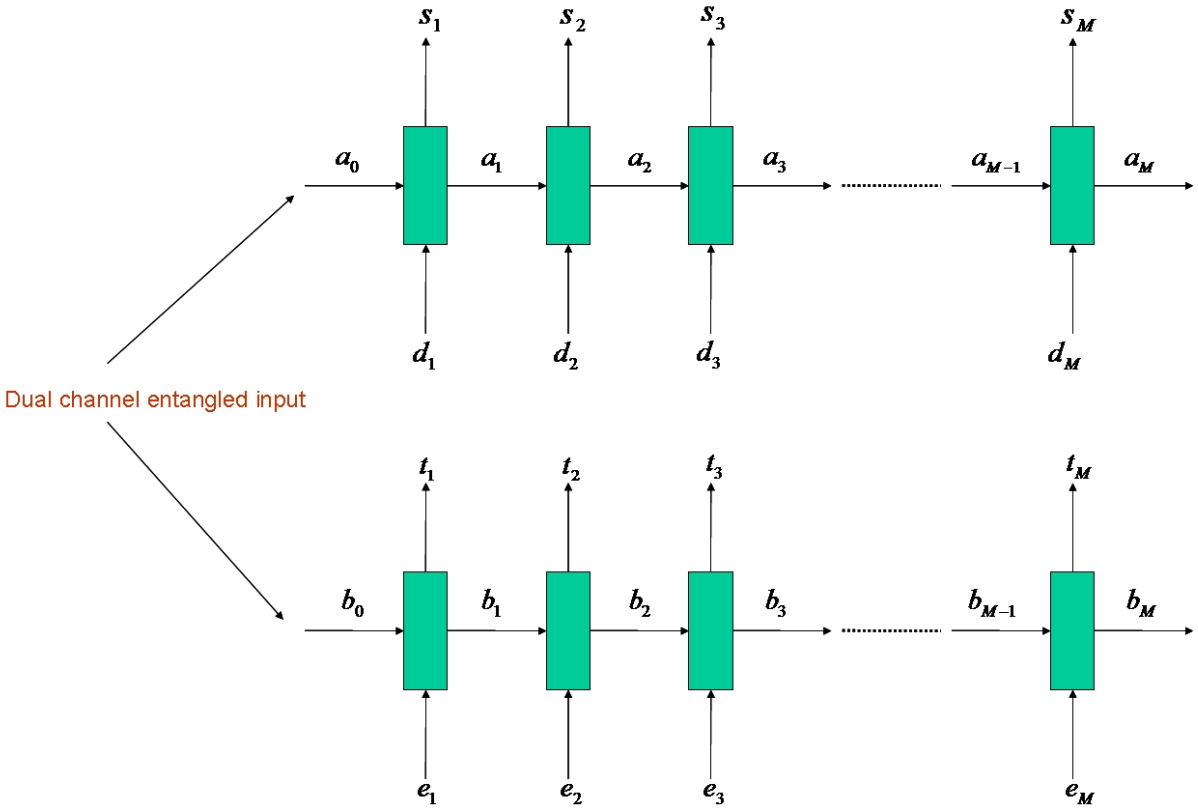

Figure 33: The Infinite-Series-of-Beam-Splitters Model for the Analysis of Lossy Propagation of Non-Classical Dual-Mode Entangled Photon States

In the dual mode case, we proceed similarly to the above and notice

$$a_0^{+} = T_a^{M} a_M^{+} + L_a s_1^{+} + L_a T_a s_2^{+} + L_a T_a^{2} s_3^{+} + \cdots + L_a T_a^{M-1} s_M^{+}$$

$$b_0^{+} = T_b^{M} b_M^{+} + L_b t_1^{+} + L_b T_b t_2^{+} + L_b T_b^{2} t_3^{+} + \cdots + L_b T_b^{M-1} t_M^{+}$$

which means an input N00N state of the form

$$|\psi_{\text{in}}\rangle = \frac{1}{\sqrt{2}}\left(|N\rangle_a|0\rangle_b + |0\rangle_a|N\rangle_b\right) = \frac{1}{\sqrt{2N!}}\left[(a_0^{+})^N + (b_0^{+})^N\right]|0\rangle_a|0\rangle_b$$

leads to the output state given by

$$|\psi_{\text{out}}\rangle = \frac{1}{\sqrt{2N!}}\Big[\Big(T_a{}^M a_M{}^+ + L_a s_1{}^+ + L_a T_a s_2{}^+ + L_a T_a{}^2 s_3{}^+ + \cdots + L_a T_a{}^{M-1} s_M{}^+\Big)^N$$
$$+ \Big(T_b{}^M b_M{}^+ + L_b t_1{}^+ + L_b T_b t_2{}^+ + L_b T_b{}^2 t_3{}^+ + \cdots + L_b T_b{}^{M-1} t_M{}^+\Big)^N\Big]|0\rangle_a|0\rangle_b$$

and the final output density matrix is given by tracing over all output loss modes

$$\rho_{\text{out}} = \text{Tr}_{\{s_1,\ldots,s_M,t_1,\ldots,t_M\}}|\psi_{\text{out}}\rangle\langle\psi_{\text{out}}|$$

Implementing the Beer limit on both channels of propagation as above, leads to the following final result for N00N states:

$$\rho_{\text{out}}(x) = \frac{1}{2}\Bigg[\sum_{n=0}^{N}\binom{N}{n}\Big(e^{-n\mu_a x}(1-e^{-n\mu_a x})^{N-n}|n\rangle_a|0\rangle_b\langle n|_a\langle 0|_b + e^{-n\mu_b x}(1-e^{-n\mu_b x})^{N-n}|0\rangle_a|n\rangle_b\langle 0|_a\langle n|_b\Big)$$
$$+ e^{-\frac{N}{2}(\mu_a+\mu_b)x}\Big(e^{i(\eta_a-\eta_b)x}|N\rangle_a|0\rangle_b\langle 0|_a\langle N|_b + e^{-i(\eta_a-\eta_b)x}|0\rangle_a|N\rangle_b\langle N|_a\langle 0|_b\Big)\Bigg]$$

6.4 Beer's Law for the Propagation of Arbitrary Entangled Dual-Mode Photon States

We now consider the most general dual-mode entangled input state (with at most N photons in each mode a and b) given by

$$|\psi_{\text{in}}\rangle = \sum_{l,m=0}^{N}\frac{\alpha_{lm}}{\sqrt{l!m!}}(a_0{}^\dagger)^l(b_0{}^\dagger)^m|0\rangle_a|0\rangle_b\ ,$$

$$\sum_{l,m=0}^{N}|\alpha_{lm}|^2 = 1\ .$$

It is cumbersome but straightforward to derive the generalized Beer-Lambert law of propagation for these general states from first principles using the same techniques as above. Assuming μ_a and μ_b are the loss coefficients, and η_a and η_b are the phase rotation rates along each mode of propagation a and b, the final result is

$$\rho_{\rm out}(x) = \sum_{p,\,q,\,p',\,q'=0}^{N} |p\rangle_a |q\rangle_b \langle p'|_a \langle q'|_b \times$$
$$\times\ e^{-\frac{1}{2}(p+p')\mu_a x} e^{-\frac{1}{2}(q+q')\mu_b x} e^{i(p-p')\eta_a x} e^{i(q-q')\eta_b x} \times$$
$$\times \sum_{l,\,m=0}^{N} \frac{\alpha_{lm}\overline{\alpha_{l+p'-p\ m+q'-q}}}{(l-p)!(m-q)!} \left(\frac{l!(l+p'-p)!\, m!(m+q'-q)!}{p!\, q!\, p'!\, q'!} \right)^{\frac{1}{2}} \times$$
$$\times\ (1-e^{-\mu_a x})^{l-p} (1-e^{-\mu_b x})^{m-q} \quad .$$

6.5 Generic Entangled States are Far More Robust Against Decoherence than N00N

For generic entangled states, we calculated the decay of coherence and entanglement numerically using the above formalism. The main result can be summarized by the following four plots (Figs. 34–37). For all plots, we assume N = 10, $\mu_a = \mu_b = \mu = 0.2$ km^{-1}, and $\eta_a = \eta_b = 1$ km^{-1}.

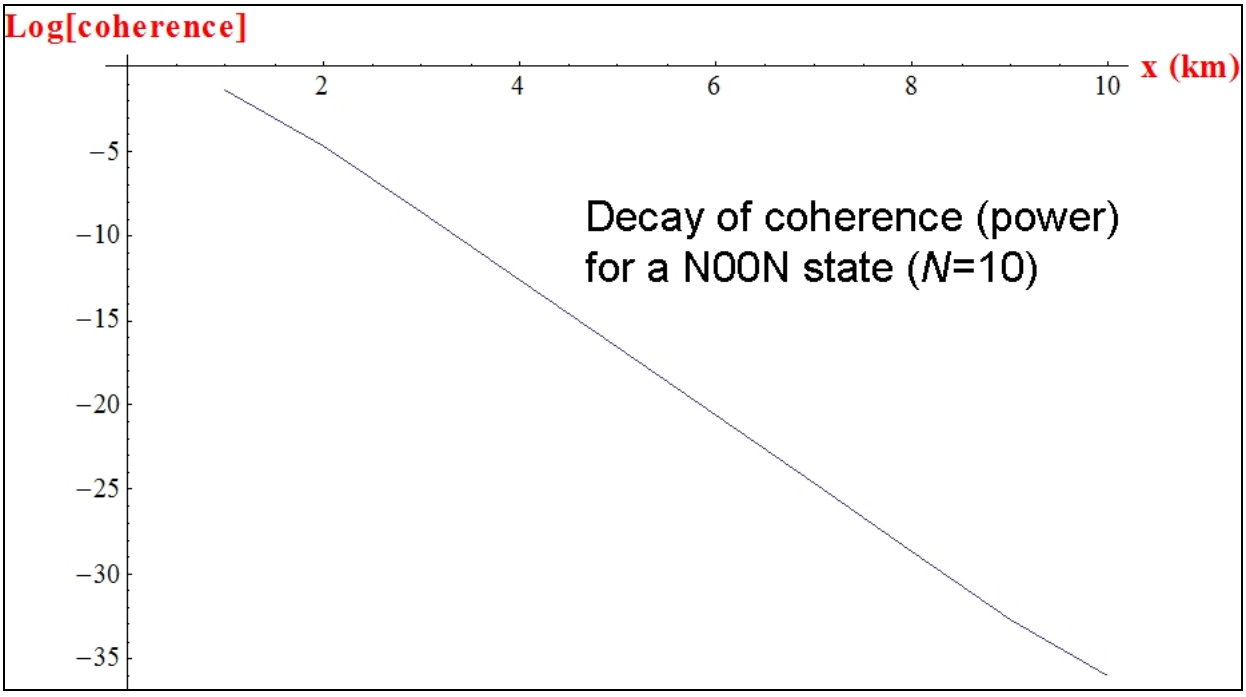

Figure 34: Decay of Coherence for A N00N State (N=10) as a Function of Propagation Distance

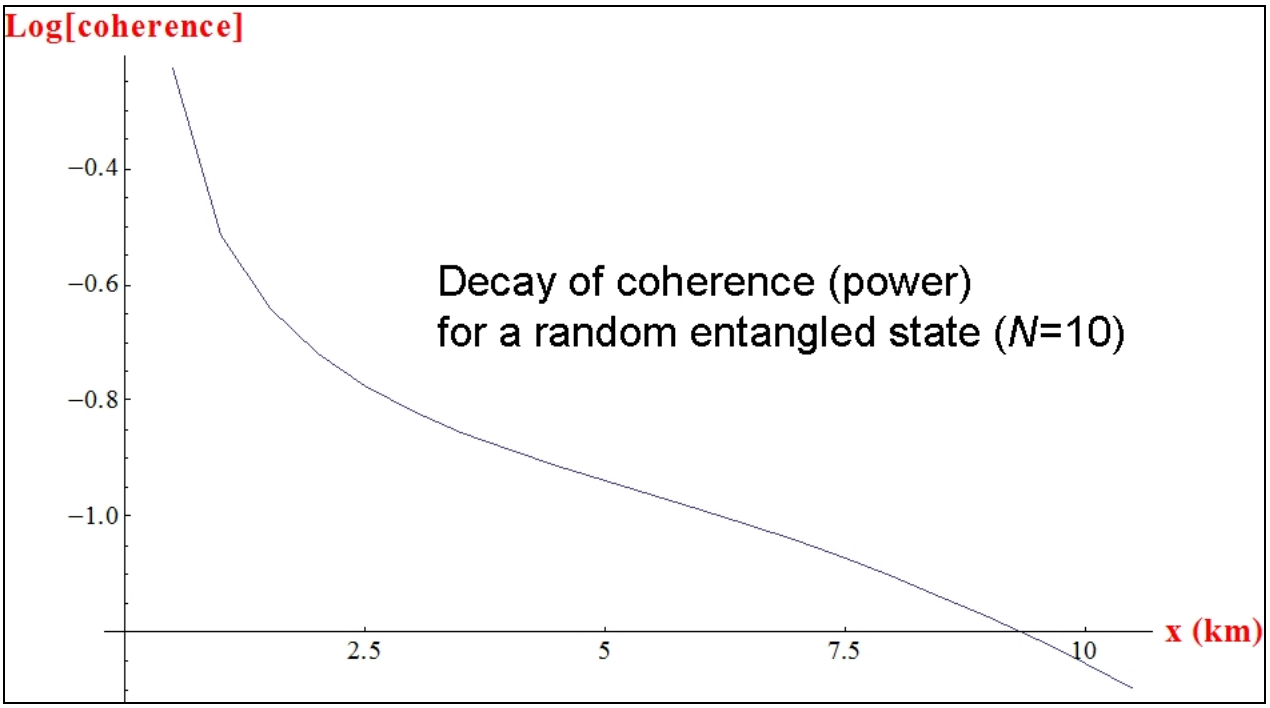

Figure 35: Decay of Coherence for a Random Entangled State (N=10) as a Function of Propagation Distance (Up To 10 km)

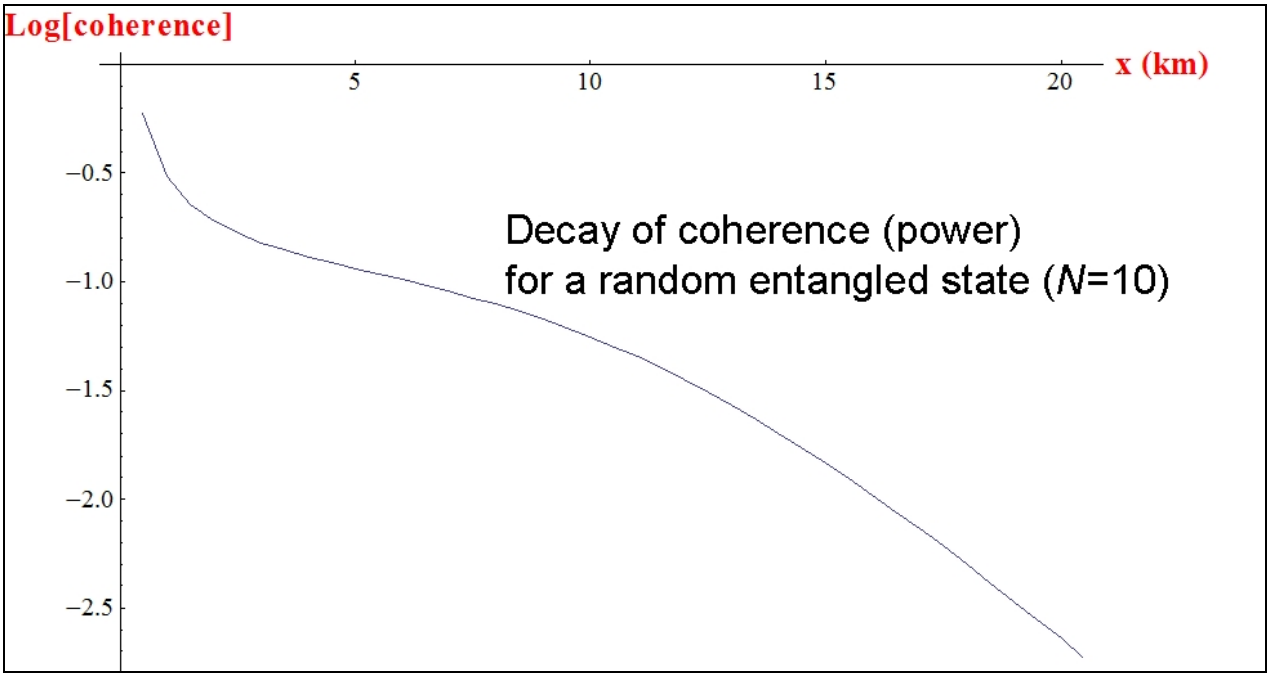

Figure 36: Decay of Coherence for a N00N State (N=10) as a Function of Propagation Distance (Up To 20 km)

For the Noon state, in Fig. 34, coherence power decays super exponentially like *exp*(-2Nμx), as expected. For a random entangled input state, in Fig. 35, coherence decays no faster that the classical loss rate *exp*(-2μx). Note that there is a mid-range plateau in loss, where decay is sub-classical, after which the classical decay rate resumes. This feature is present for generic entangled state inputs. How much of the surviving generic coherence is useful for super-classical resolution is currently under investigation.

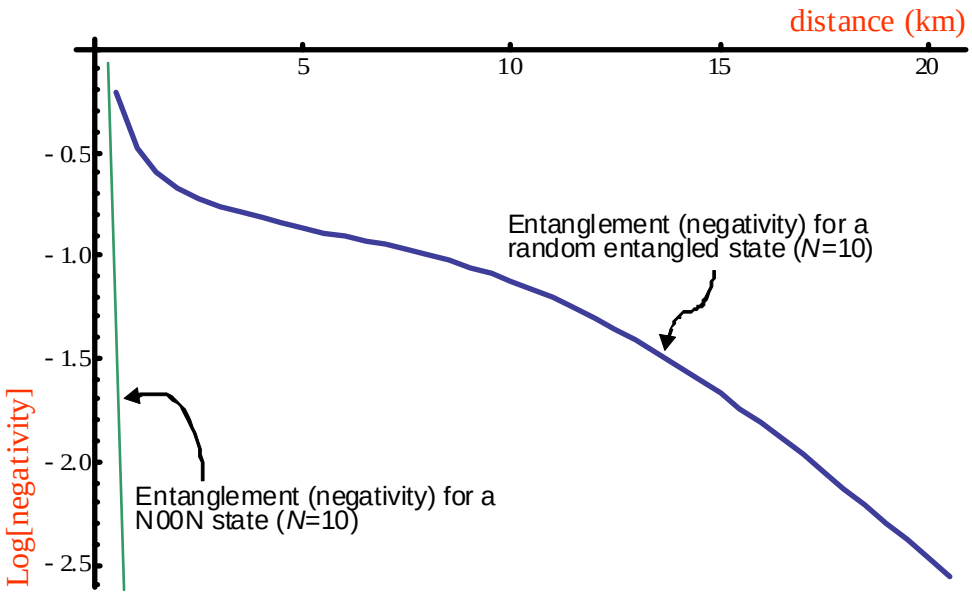

Figure 37: Decrease of Entanglement for a N00N State and a Random Entangled State (N=10) in Terms of Negativity as a Function of Propagation Distance

This last plot above (Fig. 37) is a preliminary result from very recent work and should be considered tentative.

6.6 Conclusions

The quantum-state engineering work carried out by MSA in collaboration with the rest of the LSU team shows that optimizing entangled input quantum states for a fixed detection scheme already yields sufficient super-classical resolution capabilities to satisfy the DARPA Phase I criteria for the QSP program for near to intermediate range applications (less than 10 km). It is also apparent that by cleverly redesigning the detection scheme alongside the state optimization (via transferring some of the quantum resources to the detection stage), one can alleviate propagation losses even further. While this makes the design problem even more "DARPA-hard" than the Phase I objectives, it is worth pursuing for the large payoff in potential applications.

7.0 SYSTEM ENGINEERING OF ATMOSPHERIC STATE PROPAGATION

7.1 Introduction

As discussed in the overview of Sec.5.0, above, we have finalized on a Type-II sensor proposal, which propagates classical coherent states through the atmosphere, and then implements a quantum detection scheme with number resolving detectors. In this protocol the propagation of the light through the atmosphere is entirely classical. In this context Raytheon provides well-developed classical models of LIDAR propagation, including the effects of loss by scattering and absorption, and effects of turbulence.

7.2 Gaussian Beam Propagation through Turbulent Atmosphere

Here we consider a LADAR system with an airborne transmitter and sensor located at the same position an altitude h above the ground. The transmitter produces a Gaussian beam which illuminates a perfectly reflecting target on the ground a distance R from the transmitter/sensor (Fig. 38). The beam propagates though a turbulent atmosphere. The effect of turbulence is to produce random fluctuations in the refractive index of the atmosphere, which in turn produces random modulations of the intensity and phase of the optical field. A Matrix Laboratory (MATLAB) program was written to calculate the intensity and phase profiles of the beam returned to the sensor. Since the turbulent fluctuations are random, the result of the calculation corresponds to one statistical realization of a turbulent atmosphere.

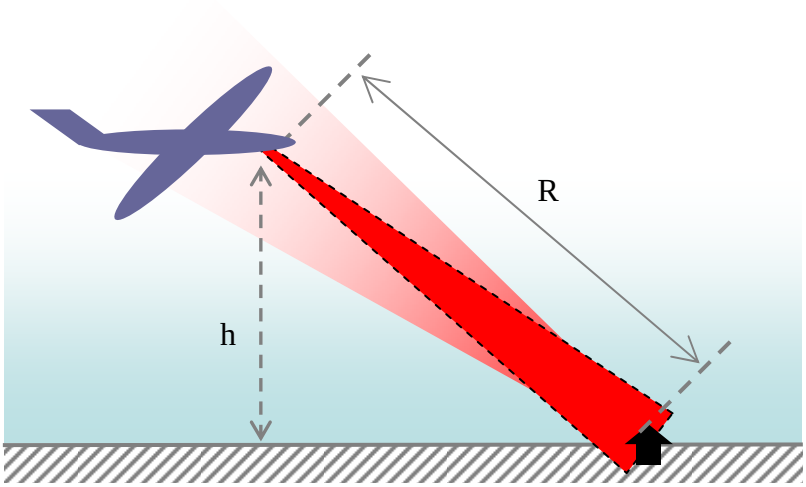

Figure 38: Schematic of an Airborne LADAR System and a Target on the Ground

The geometry of the equivalent problem modeled in MATLAB is shown below (Fig. 39). A split step method was used to propagate the field, where the full path is broken up into several short steps of length Δz, and the effects of diffraction and turbulence are calculated separately at each step.

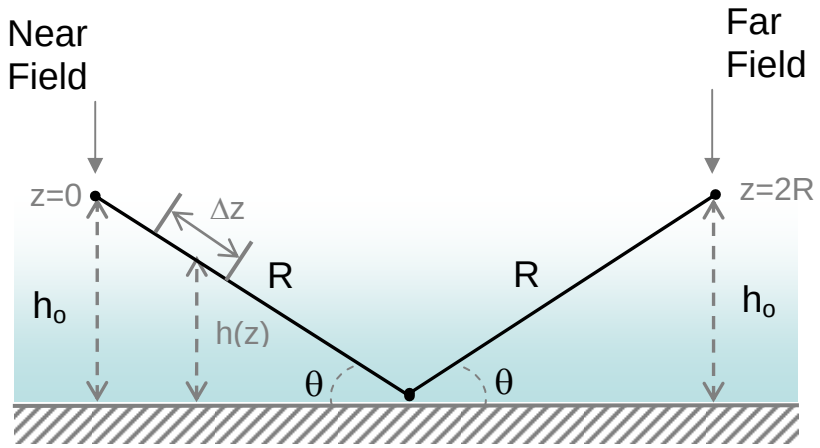

Figure 39: Geometry of the Equivalent Problem Modeled In MATLAB

Given a field distribution $E(x_1,y_1)$ at the input plane, the Fresnel diffraction integral specifies the field $E(x_2,y_2)$ on the output plane a distance Δz from the input. The (x_i,y_i) are Cartesian spatial coordinates in the plane transverse to the direction of propagation.

$$E(x_2,y_2)=\int_{-\infty}^{\infty}\int_{-\infty}^{\infty}E(x_1,y_1)\frac{e^{ik\Delta z}}{i\lambda\Delta z}e^{i\frac{k}{2\Delta z}\left[(x_2-x_1)^2+(y_2-y_1)^2\right]}dx_1dy_1$$

The Fresnel diffraction integral is a two dimensional convolution. It is computationally more efficient to evaluate the convolution integral using Fast Fourier transforms (FFT). This technique is known as the Fresnel angular spectrum propagator.

$$E(x_2,y_2)=FFT^{-1}\left\{FFT\left[E(x_1,y_1)\right]\cdot e^{ik\Delta z}e^{-i\pi\lambda(f_x^{\,2}+f_y^{\,2})\Delta z}\right\}$$

Here f_x and f_y are spatial frequencies of the plane waves whose superposition give the field distribution. Because Fourier transforms are used to evaluate the integral, the field E is seen as periodic in space. A portion of the field that diffracts outward beyond the computational grid edge will then enter the computational grid from the opposite edge, so as to conserve energy. For this reason apodization is used to attenuate the field as it diffracts toward the grid edge, which is equivalent to a loss of energy as the field diffracts off the grid.

After accounting for the effects of diffraction over the propagation distance Δz, the effects of turbulence over the propagation distance Δz are applied to the field. Turbulence imposes a random phase shift upon the field at each point in the transverse plane.

$$E'(x_2,y_2)=E(x_2,y_2)\cdot e^{i2\pi\cdot\Delta n(x_2,y_2)}$$

Here $\Delta n(x,y)$ is the change in refractive index at each point in the transverse plane, and is a matrix of random numbers which is generated by taking the inverse Fourier transform of it's power spectral density function $\Phi_n(\boldsymbol{\kappa})$, where $\boldsymbol{\kappa}$ is a spatial angular frequency vector. The spectral density used to model turbulence induced refractive index fluctuations of the atmosphere is called the *modified atmospheric spectrum* [Andrews1998].

$$\Phi_n(\kappa) = 0.033 \cdot C_n^2 \cdot \left[1 + 1.802 \frac{\kappa}{\kappa_\ell} - 0.254 \left(\frac{\kappa}{\kappa_\ell} \right)^{7/6} \right] \frac{e^{-(\kappa/\kappa_\ell)^2}}{\left(\kappa^2 + \kappa_o^2 \right)^{11/6}}$$

The Φ_n is isotropic and only depends on κ, the magnitude of $\boldsymbol{\kappa}$. The κ_l is the inner scale of turbulence, which introduces a roll off at the high frequency end of the spectrum, and is related to the shortest distance over which turbulent cells form. The κ_o is the outer scale of turbulence, which limits power in the low frequency end of spectrum and corresponds to longest distance over which turbulent cells form. The Φ_n has an approximate $\kappa^{-11/3}$ dependence on spatial angular frequency between the inner and outer scales (Fig. 40).

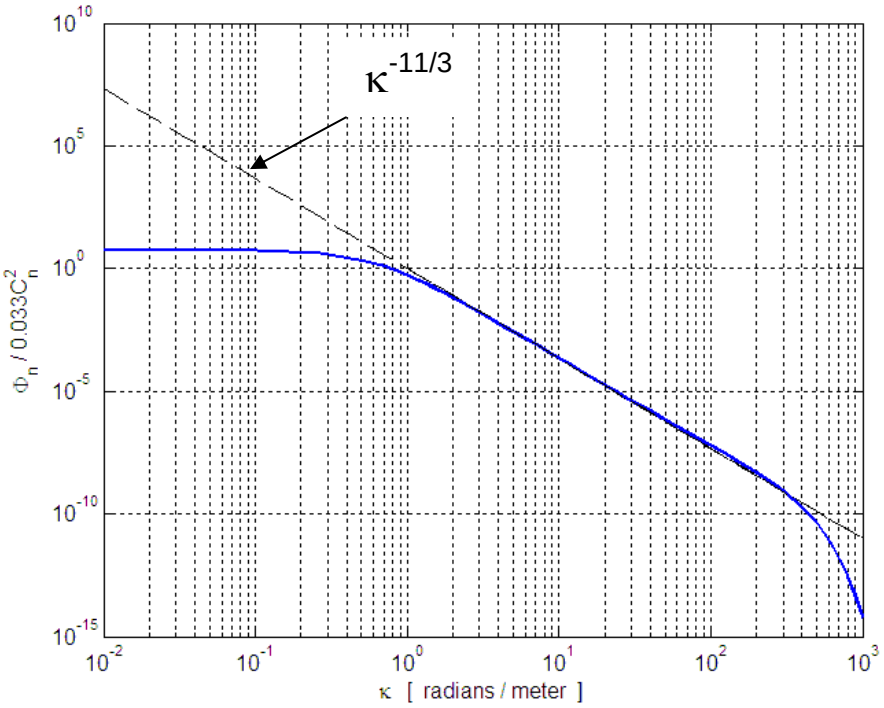

Figure 40: Spatial Power Spectral Density of Refractive Index Fluctuations

The parameter C_n^2 is called the refractive index structure constant and it determines the strength of turbulence [Hardy1998]. The C_n^2 is a function of altitude h, is large near the ground (corresponding to strong turbulence), and decreases with altitude (corresponding to progressively weaker turbulence). The C_n^2 profile used in the following calculations is a modified Hufnagel-Valley model [Schmitt1996].

$$C_n^2(h) = 8.2 \cdot 10^{-56} w^2 h^{10} e^{-h/1000} + 2.7 \cdot 10^{-16} e^{-h/1500} + A \cdot h^{-4/3} e^{-h/100}$$

Here w is the rms wind speed between 5 and 20 km above ground and A is the value of C_n^2 one meter above ground. A plot of C_n^2 vs. altitude shows that C_n^2 decreases by two orders of magnitude between 1 and 20 meters, decreases by another two orders of magnitude between 20 and 1000 meters, and quickly becomes negligible above 25 km (Fig. 41).

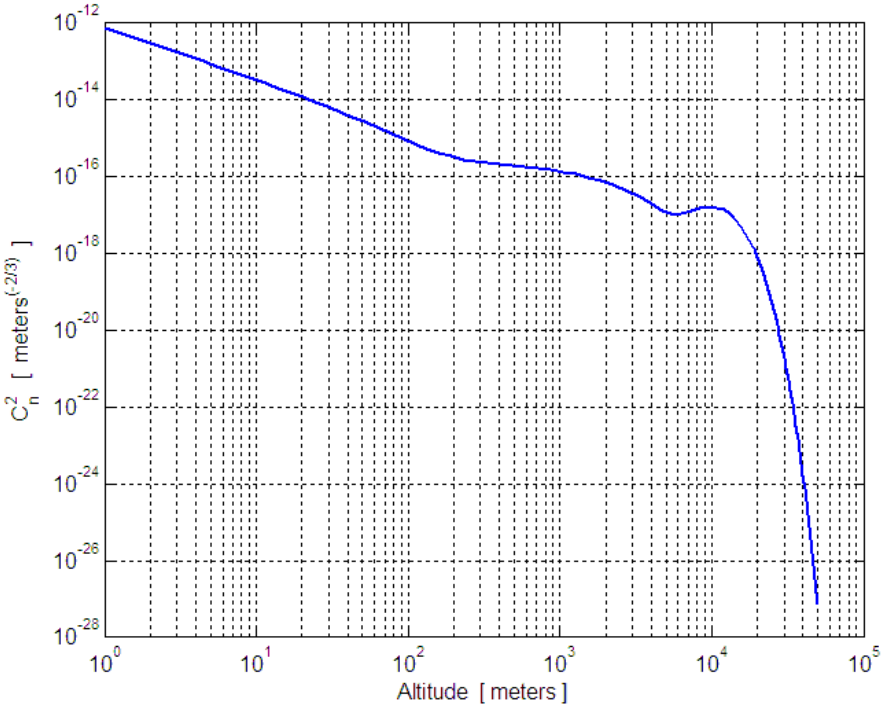

Figure 41: Strength of Turbulence vs. Altitude

The initial field launched from the transmitter was a planar wave front Gaussian beam with a $1/e^2$ diameter of 1 cm and wavelength of 1.5 μm (shown in Fig. 42). This corresponds to a Rayleigh range of 52 meters. The equivalent problem modeled in MATLAB propagates the beam a distance R towards the ground at an angle of 45°, passes through a 1 meter diameter aperture, and then propagates towards the sensor at an angle of 45° where it is received by a 30 cm diameter aperture (Fig. 43).

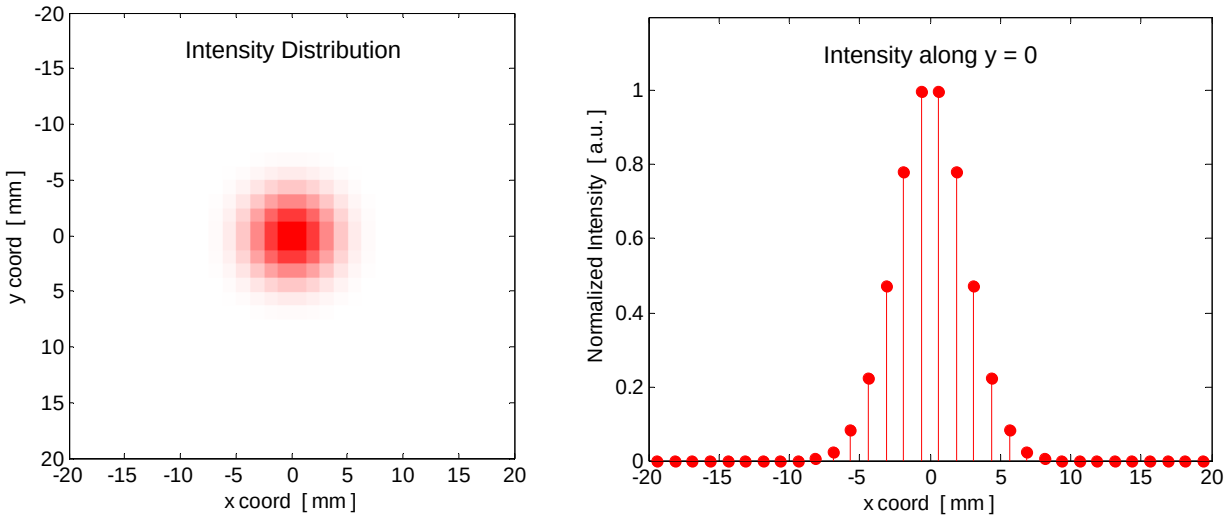

Figure 42: Intensity Distribution of the Initial Field Launched from Transmitter

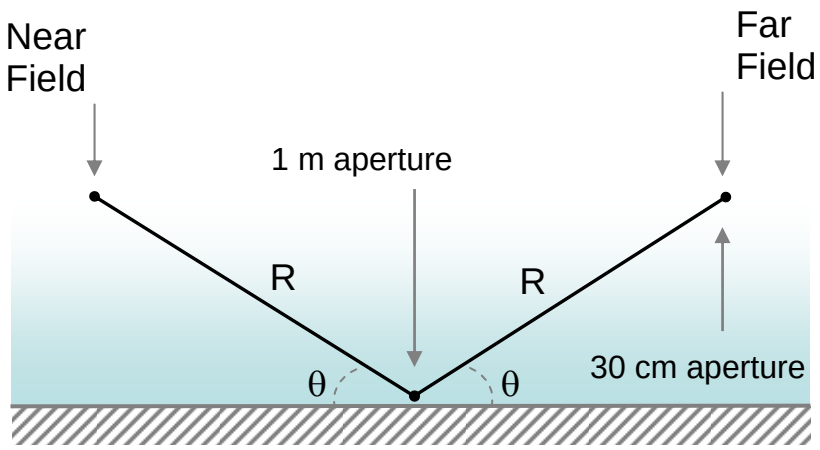

Figure 43: Parameters Used in the MATLAB Program

The following plots (Figs. 44–46) show the intensity and phase of the received field for ranges of 1, 5, and 10 km. The phase distribution is shown after correcting for field curvature by focusing with a lens of focal length *2R*. In the absence of turbulence, this would produce a plane wave front. The two dimensional phase distributions are not unwrapped, therefore pure black and pure white on this plot correspond to the same phase. The phase profiles along the y = 0 coordinate have been unwrapped. Where the field amplitude is zero, the phase is not well defined and can take on arbitrary values. This causes the unwrapped phase to take on large values where the field amplitude is negligible. In all cases the attenuation coefficient for scattering and absorption due to the atmosphere was taken to be 0.155 km^{-1}, corresponding to the attenuation of 1.5 μm light at sea level on a clear day [RCA1974].

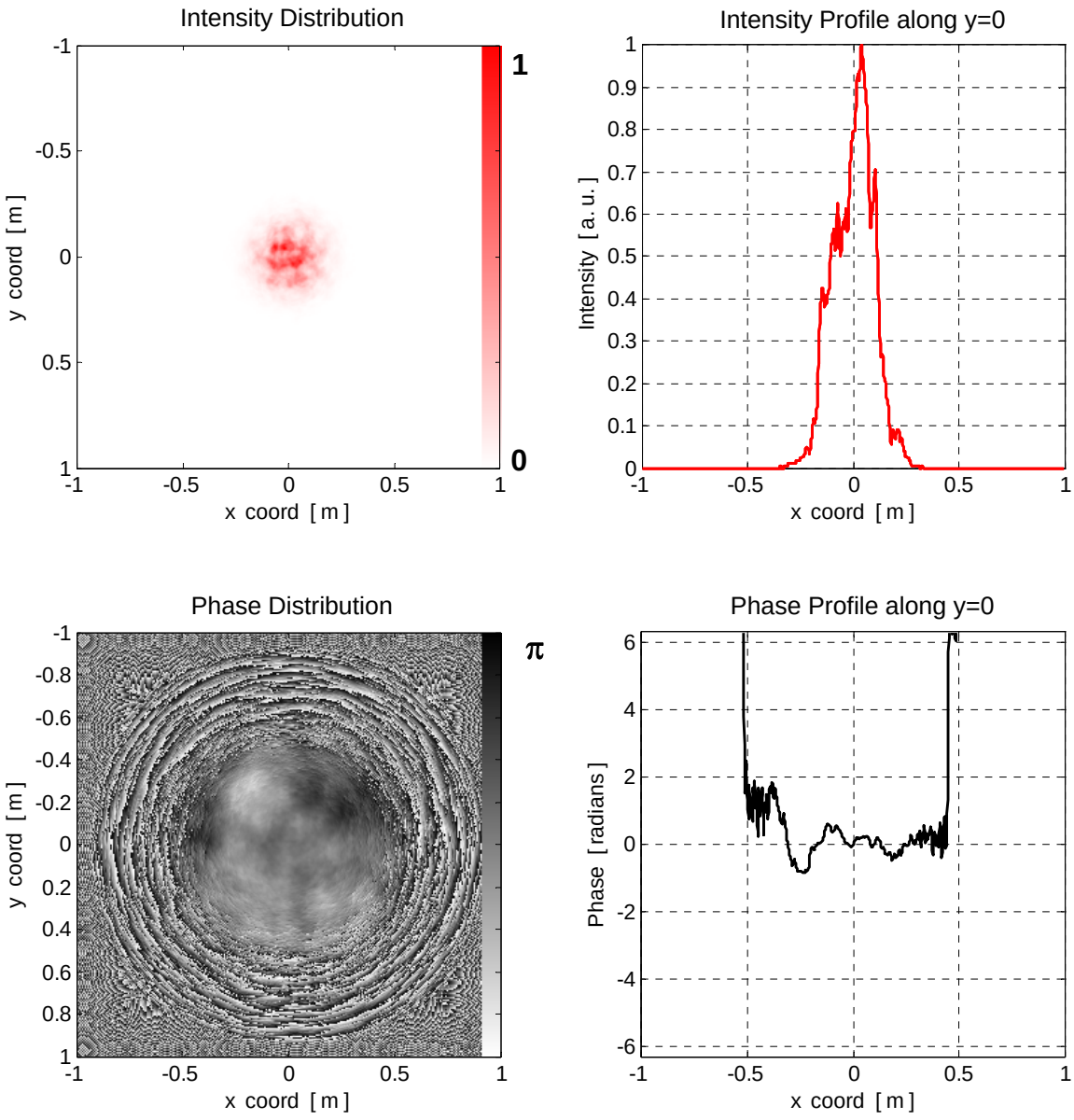

Power along path of propagation

1.0000 launched
0.8564 reached target
0.8564 reflected from target
0.7334 returned to sensor
0.5318 at receiving aperture

Total loss is 2.74 dB

Figure 44: Intensity Returned to Sensor, *R* = 1 km

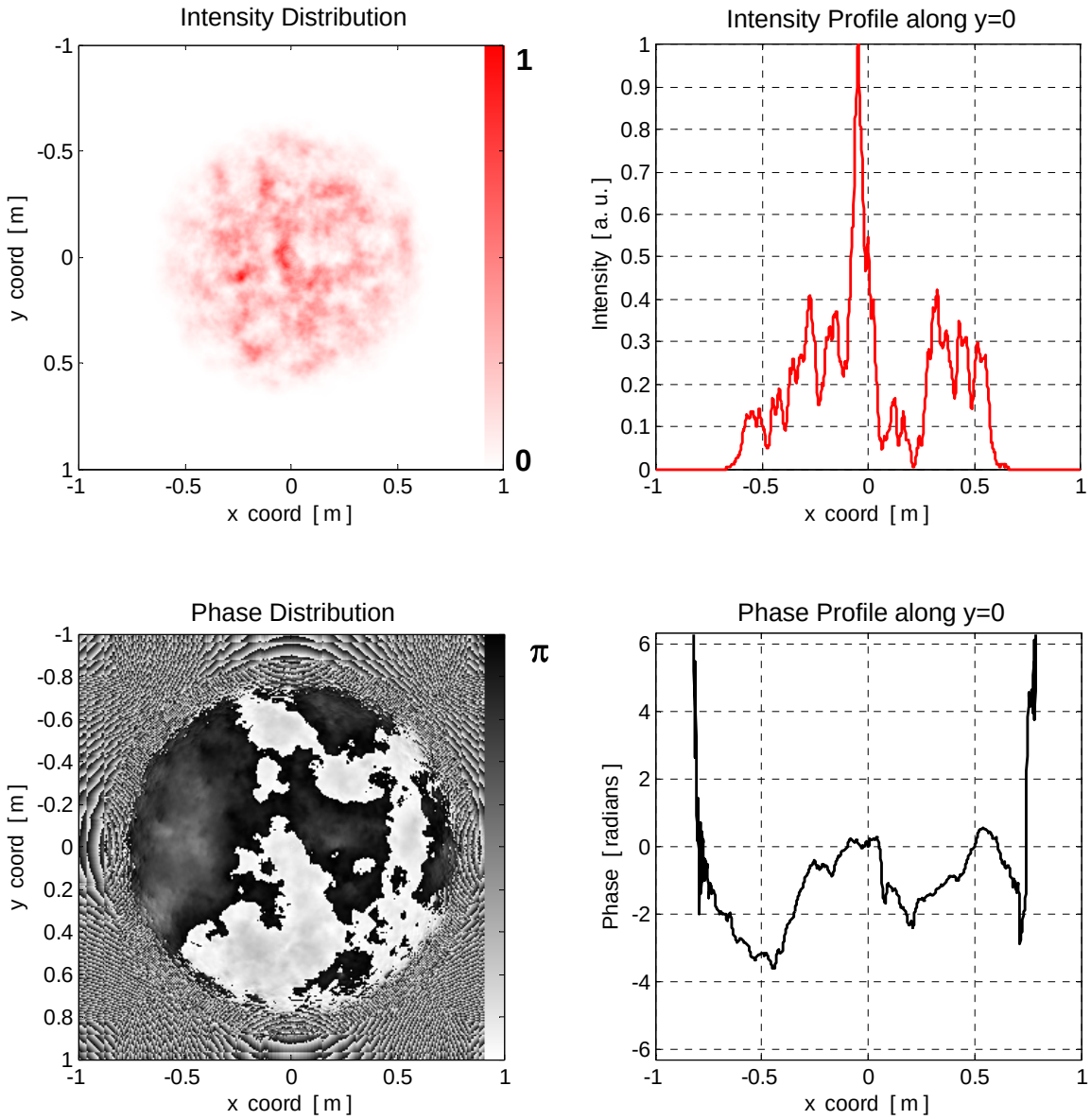

Power along path of propagation

1.0000 launched
0.4368 reached target
0.4068 reflected from target
0.1061 returned to sensor
0.0108 at receiving aperture

Total loss is 19.6 dB

Figure 45: Intensity Returned to Sensor, *R* = 5 km

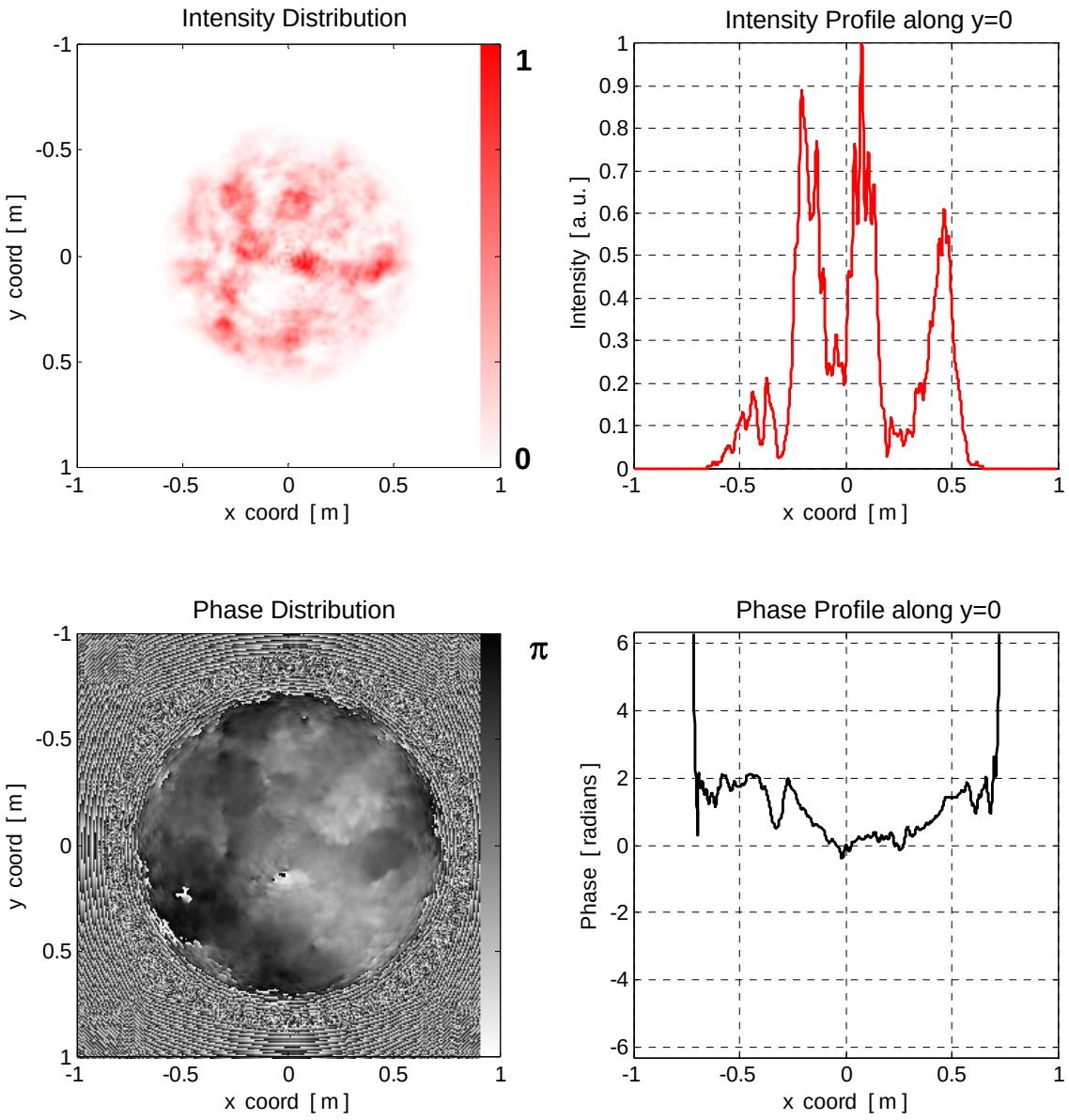

Power along path of propagation

1.0000 launched
0.1064 reached target
0.0876 reflected from target
0.0062 returned to sensor
0.0006 at receiving aperture

Total loss is 32.2 dB

Figure 46: Intensity Returned to Sensor, *R* = 10 km

7.3 Atmospheric Attenuation and Background Count Rate as a Function of Altitude

A MODerate resolution atmospheric TRANsmission (MODTRAN) code was used to calculate the atmospheric attenuation coefficient and the background count rate of an airborne photodetector as a function of altitude. The MODTRAN code is part of a larger software package called SAMM (Super Harvard Architecture Single-chip Computer (SHARC) and MODTRAN Merged), which is run through a graphical user interface called PLEXUS (Phillips Laboratory Expert-assisted User Software) [Berk1999, Ip2003, Sharma1996]. The following calculations use atmospheric conditions for a clear day with a meteorological range of 23 km.

MODTRAN was used to calculate the spectral transmission for a vertical path through the atmosphere, from ground level to an altitude of 10 km. The uppermost line in the plot below shows the transmission from the ground to an altitude of 100 meters (Fig. 47). The line below it shows the transmission from ground to an altitude of 200 meters, etc. Taking a vertical cut through the above plot gives the atmospheric transmission as a function of altitude for a particular wavelength, shown below for 1.55 μm (see Fig. 48 below).

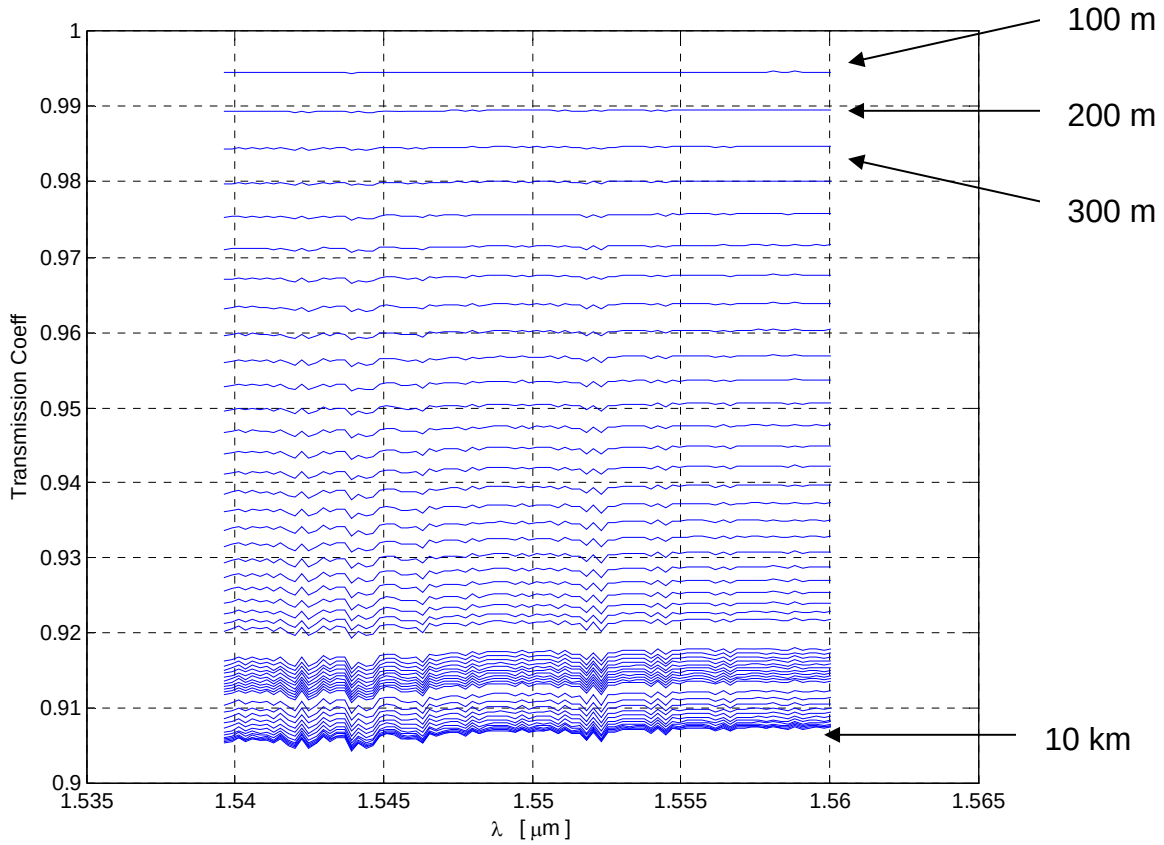

Figure 47: Spectral Transmission Calculated by MODTRAN

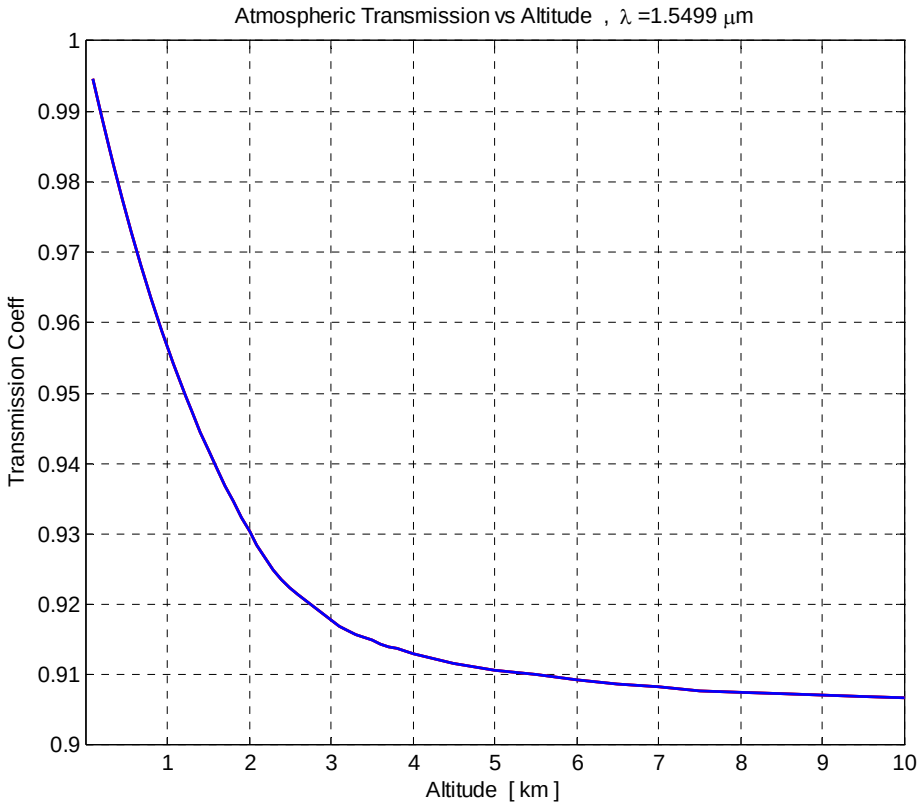

Figure 48: Atmospheric Transmission vs Altitude

We can calculate the atmospheric attenuation coefficient from transmission data in the following way. Assume that the transmission decreases exponentially, with an attenuation coefficient that varies with altitude:

$$P(z) = P(0) \cdot \exp\left[-\alpha(z_1)\Delta z_1\right] \cdot \exp\left[-\alpha(z_2)\Delta z_2\right] \cdots \exp\left[-\alpha(z_n)\Delta z_n\right]$$

$$P(z) = P(0) \cdot \exp\left[-\sum_k \alpha(z_k)\Delta z_k\right]$$

$$P(z) = P(0) \cdot \exp\left[-\int_0^z \alpha(\xi)d\xi\right]$$

The atmospheric transmission *T(z)* is then given by:

$$T(z) = \frac{P(z)}{P(0)} = \exp\left[-\int_0^z \alpha(\xi)d\xi\right]$$

The attenuation coefficient $\alpha(z)$ is related to the atmospheric transmission by the expression:

$$\alpha(z) = \alpha(0) - \frac{d}{dz}\left[\ln\left(T(z)\right)\right]$$

The data points from the transmission plot above were used to generate values for atmospheric attenuation coefficient as a function of altitude, shown in Fig. 49 below.

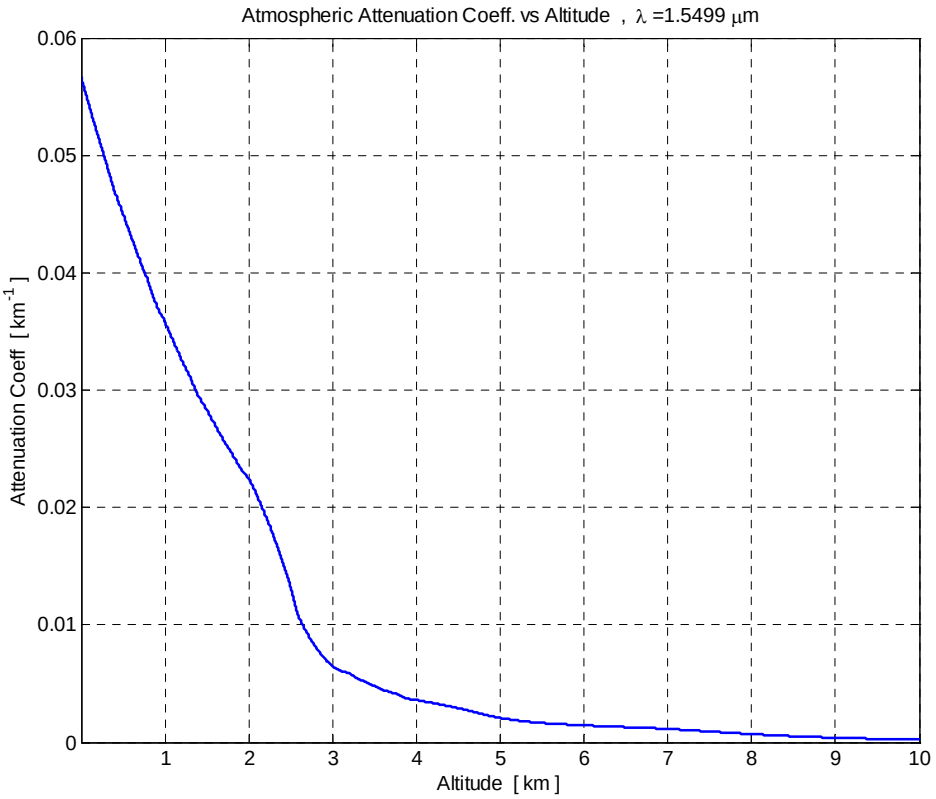

Figure 49: Atmospheric Attenuation Coefficient vs Altitude

Fig. 49 shows that the attenuation coefficient decreases significantly with altitude and asymptotically approaches zero. This dependence is expected since the attenuation is due to absorption and scattering by atmospheric gasses, whose density decreases approximately exponentially with altitude.

To estimate the background count rate of the sensor, we need to know the area of the sensor's receiving aperture, the sensor's angular field of view, and the spectral radiance incident upon the sensor. Figure 50 below shows the sensor's field of view (FOV) filled with sunlight reflected from the Earth. Because sunlight contributes to background radiance, the position of the sun relative to the sensor/target line of sight is important. For these calculations the time of day is 8:00 am.

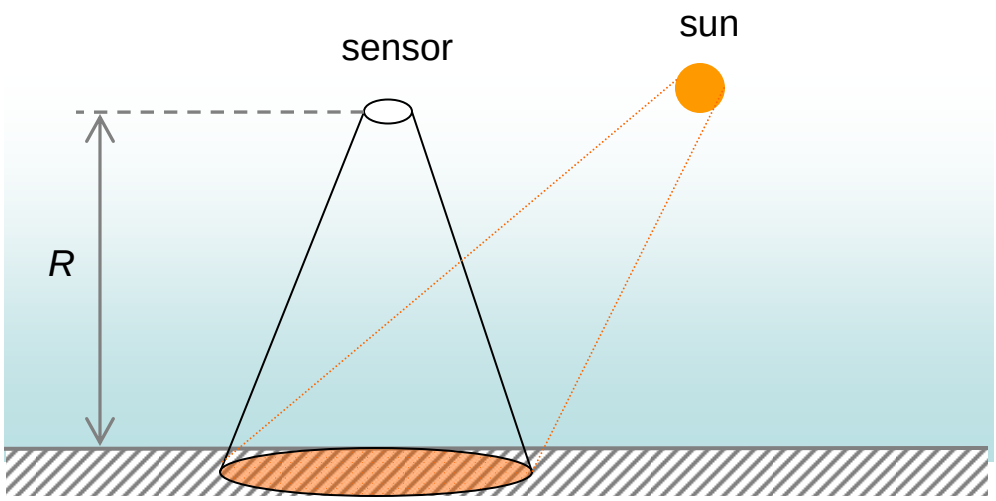

Figure 50: Sensor's Field of View (FOV) Filled with Reflected Sunlight

The sensor's field of view θ_{FOV} is determined by the receiving lens focal length f and the detector size d, but cannot be less than the diffraction limit λ/D, where D is the lens diameter (Fig. 51).

$$\theta_{FOV} = \max\left(\frac{d}{f}, \frac{\lambda}{D}\right)$$

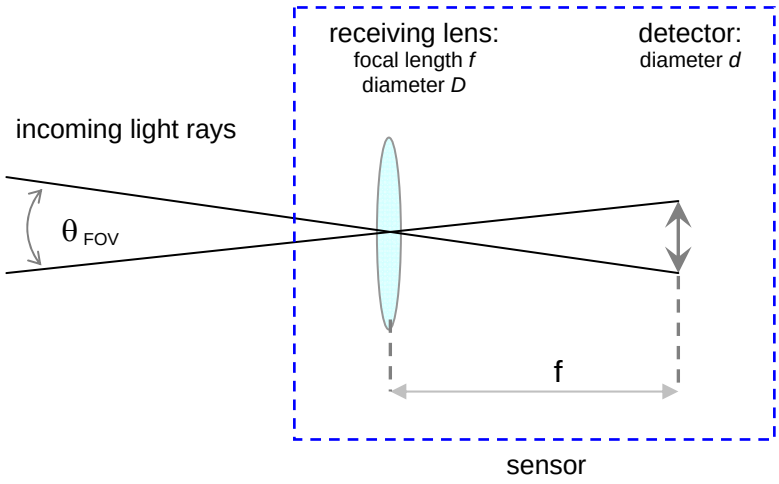

Figure 51: Sensor's Field of View (FOV)

The solid angle Ω associated with the sensor's field of view is the ratio of the ground area viewed by the sensor to the square of the sensor range. This gives a solid angle Ω, which is constant over range and only depends on field of view (see Fig. 52 below):

$$\Omega = \frac{A}{R^2} = \frac{\pi}{4} \cdot \theta_{FOV}^2$$

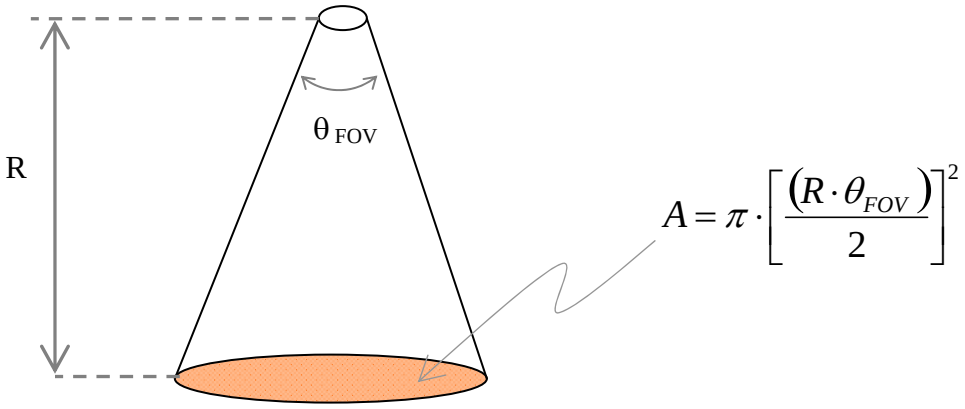

Figure 52: Solid Angle Associated with Sensor's Field of View (FOV)

Assuming a 30 cm diameter for the receiving lens, the diffraction limited field of view is $\frac{1.55\mu m}{30cm} = 5.2\mu rad$. Assuming a detector diameter of 25 μm and an *f/3* lens (90 cm focal length), the field of view is $\frac{25\mu m}{90cm} = 28\mu rad$. Going to a *f/10* lens (3 m focal length) gives a field of view $\frac{25\mu m}{3m} = 8\mu rad$, near the diffraction limit. MODTRAN was also used to calculate the spectral radiance *S* incident upon an airborne sensor looking downward towards the ground. Spectral radiance quantifies the amount of light reaching the detector due to sunlight reflected from the Earth into the sensor's field of view, sunlight scattered into the sensor's field of view, and blackbody radiation from atmospheric gasses. Spectral radiance has units of Watts / cm^2 / sr / μm. MODTRAN calculates the radiance per inverse centimeter (wavenumber spectrum). To convert this to radiance per micron (wavelength spectrum), use:

$$S_{W/cm^2/sr/\mu m} = \frac{10^4}{\lambda_{\mu m}^2} \cdot S_{W/cm^2/sr/cm^{-1}}$$

A plot of spectral radiance is shown in Fig. 53 below. The bottom line shows the spectral radiance for a sensor 100 m above the ground. The line above it shows spectral radiance at 200 m above the ground, etc. Taking a vertical cut through the above plot gives the radiance as a function of altitude for a particular wavelength, shown below for 1.55 μm (Fig. 54).

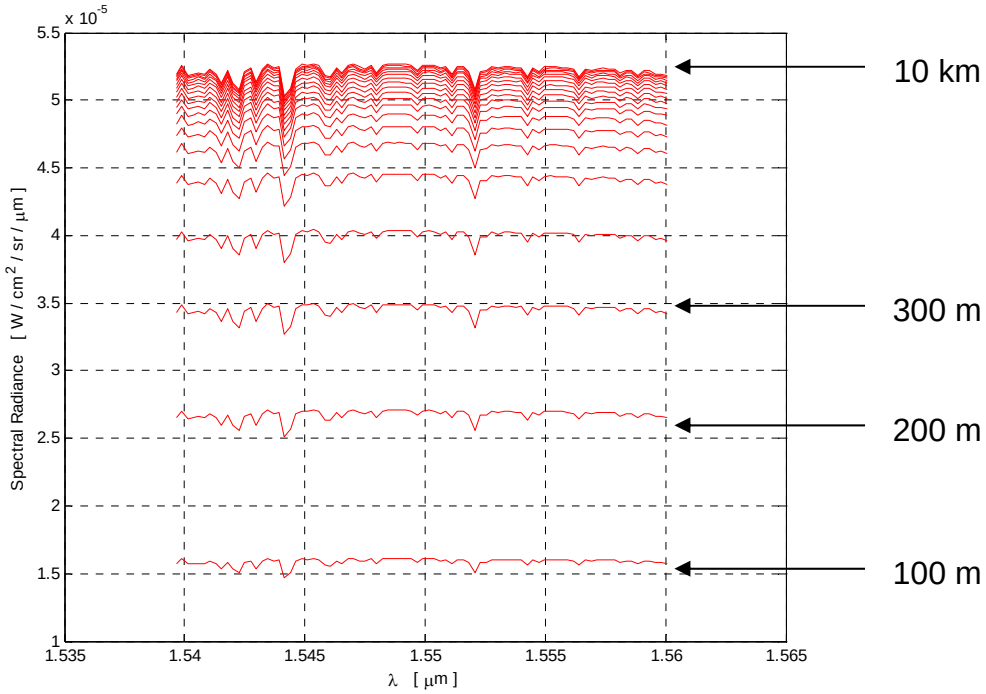

Figure 53: Spectral Radiance vs Wavelength

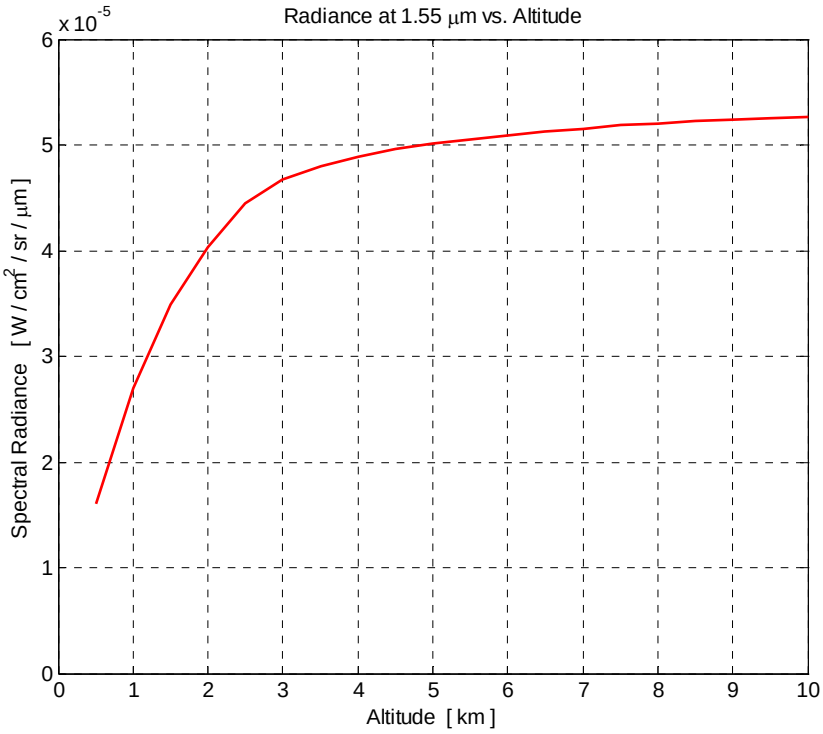

Figure 54: Spectral Radiance vs Altitude at λ = 1.55 μm

To obtain information on background counts arriving at a detector, we need to specify the laser wavelength, target range, optical bandwidth, and detector area. Then the background power in Watts, $P_{BG,\,Watts}$, that reaches the sensor is:

$$\underbrace{P_{BG,Watts}}_{\text{background power}} = \underbrace{S_{W/cm^2/sr/\mu m}}_{\text{spectral radiance}} \cdot \underbrace{\pi\left(\frac{D_{cm}}{2}\right)^2}_{\text{detector area}} \cdot \underbrace{\left(\frac{\pi}{4}\cdot\theta_{FOV}^2\right)}_{\text{solid angle}} \cdot \underbrace{BW_{\mu m}}_{\text{optical bandwidth}}$$

Where S is spectral radiance, D_{cm} is the diameter of the receiving aperture in centimeters, θ_{FOV} is the angular field of view in radians, and $BW_{\mu m}$ is the bandwidth of the optical filter in microns. Then,

$$P_{BG,Watts} = S_{W/cm^2/sr/\mu m}\cdot\frac{\pi^2}{16}\cdot D_{cm}^2\cdot\theta_{FOV}^2\cdot BW_{\mu m}$$

If the detector is gated so that it only operates for a time interval $T_{\mu s}$ microseconds, then the number of background photons N_{BG} detected during each gate is:

$$\underbrace{N_{BG}}_{\text{number of background photons}} = P_{BG,Watts}\cdot\frac{\overbrace{T_{\mu s}\cdot 10^{-6}\,\frac{s}{\mu s}}^{\text{gate time}}}{\underbrace{E_{eV}\cdot(1.6\cdot 10^{-19})\,\frac{J}{eV}}_{\text{photon energy}}}$$

The resulting formula for conversion between spectral radiance and number of background photon counts is:

$$N_{BG} = (3.1\cdot 10^{12})\cdot S_{W/cm^2/sr/\mu m}\cdot D_{cm}^2\cdot\theta_{FOV}^2\cdot BW_{\mu m}\cdot T_{\mu s}\cdot\lambda_{\mu m}$$

The background photon count as a function of altitude is shown in Fig. 55, for a 30.5 cm diameter receiving aperture, 28 μrad field of view, 1 nm optical filter, 1 μs gate length, and 1.55 μm wavelength.

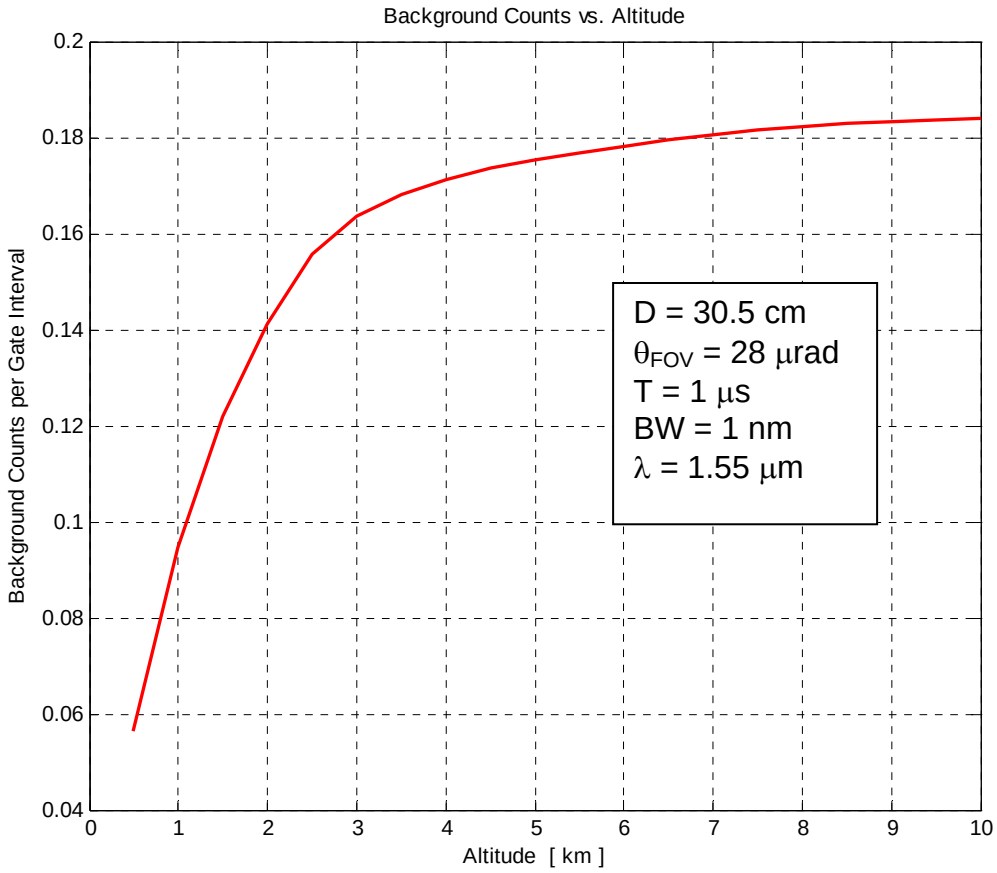

Figure 55: Background Photon Counts vs Altitude

7.4 Packaging Capability

Raytheon's MTS-A offers state of the art EO/IR and laser sensor capabilities, including seven fields of view, color TV, electronic zoom, three modes of automated video tracking, fused imagery, designation/range-finding and illumination, and analog and digital video outputs (Fig. 56). Multi-capable, the AN/AAS-52 comes fully loaded for multiple mission applications in intelligence, surveillance and Reconnaissance on manned and unmanned aircraft.

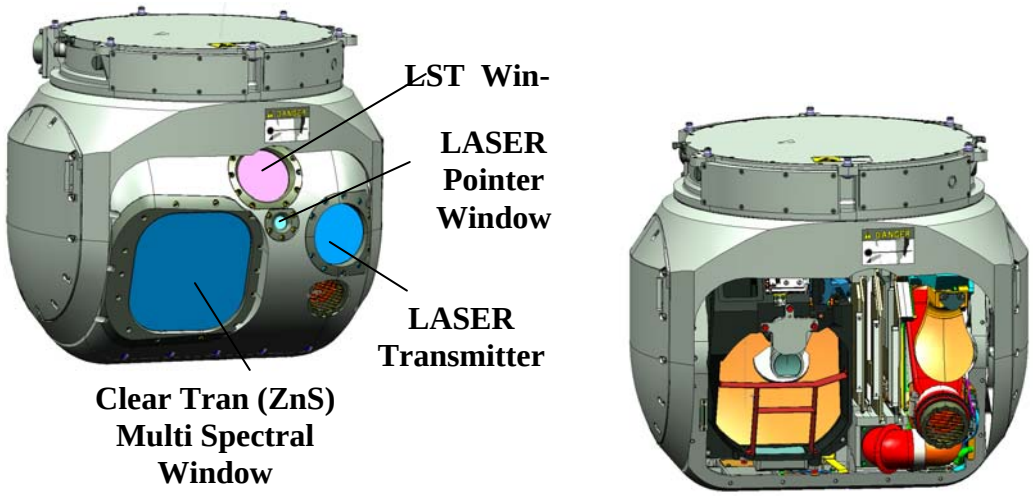

Figure 56: Schematic of Packaging

The MTS-B provides accurate detecting, ranging, and tracking for the U.S. Air Force Predator B and for today's military forces worldwide. Using state-of-the-art digital architecture, this advanced system provides long-range surveillance, high-altitude target acquisition, tracking, rangefinding, and laser designation for the Heliborne Laser Fire & Forget Missile System (HELLFIRE) missile and for all tri-service and North Atlantic Treaty Organization (NATO) laser-guided munitions. The MTS and variants are available to support domestic and international user missions for rotary-wing, unmanned airborne vichecle (UAV), and fixed-wing platforms. The MTS-B provides detecting, ranging, and tracking for the U.S. Air Force Predator B and for today's military forces worldwide. Using state-of-the-art digital architecture, this advanced system provides long-range surveillance, high-altitude target acquisition, tracking, rangefinding, and laser designation for the HELLFIRE missile and for all tri-service and NATO laser-guided munitions.

The MTS and variants are available to support domestic and International user missions for rotary-wing, UAV, and fixed-wing platforms. The AN/AAS-52 MTS-A provides superior ranging, detecting and tracking capabilities through high performance EO/IR and laser designation/ illumination system attributes. Additionally, Raytheon's MTS-A gives customer's configuration options without platform modification, and mission system integration remains a cornerstone feature of the AN/AAS-52 due to common technology aspects of its turret components and system electronics unit.

Raytheon's AN/ZSQ-2(V) turret is based from the Airborne Electro-optical Special Operation Payload (AESOP), and is shown in Fig. 57. This turret is mounted on the Blackhawk helicopter, the Northrop Grumman Fire Chief, and other platforms. Typical to most of the ball turrets that Raytheon makes, it has sensing, ranging and designation capabilities.

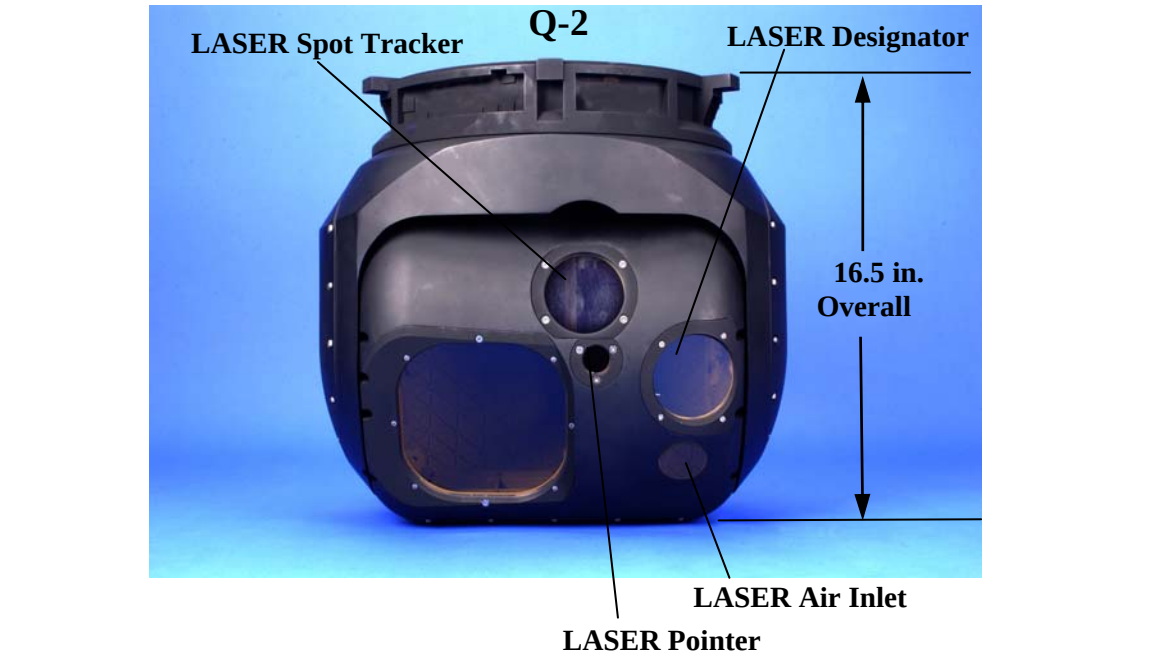

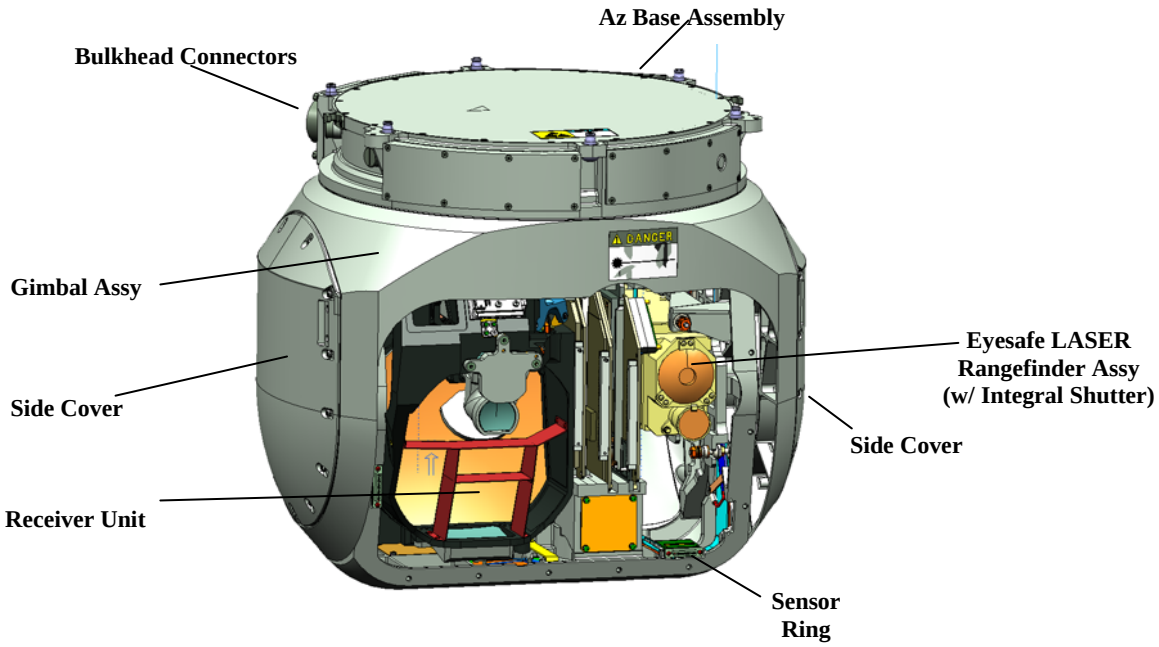

Figure 57: Schematic of Raytheon's AN/ZSQ-2

The latest turret that Raytheon has made is the Common Sensor Platform (CSP) turret. It is named as such because it can be effectively used on a variety of platforms, including helicopters, UAV's and even stationary post-mount applications.

8.0 BIBLIOGRAPHY

[Abouraddy2002] Abouraddy AF, Saleh BEA, Sergienko AV, et al., Entangled-photon Fourier optics, Journal Of The Optical Society Of America B-Optical Physics 19 (5): 1174–1184 May 2002.

[Agarwal2007] Agarwal, GS; Chan, KW; Boyd, RW; et al. Quantum states of light produced by a high-gain optical parametric amplifier for use in quantum lithography JOURNAL OF THE OPTICAL SOCIETY OF AMERICA B-OPTICAL PHYSICS, 24 (2): 270-274 FEB 2007.

[Andrews1998] Andrews, LC; Phillips, RL; *Laser Beam Propagation through Random Media*, The Society of Photo-Optical Instrumentation Engineers, 1998.

[Berk1999] Berk, A; et al.; *MODTRAN4 User's Manual*, Air Force Research Laboratory, 1999.

[Berry2000] Berry, DW; Wiseman, HM Optimal states and almost optimal adaptive measurements for quantum interferometry PHYSICAL REVIEW LETTERS, 85 (24): 5098-5101 DEC 11 2000.

[Beskrovnyy2005] Beskrovnyy VN, Kolobov MI, Quantum limits of super-resolution in reconstruction of optical objects, Physical Review A 71 (4): Art. No. 043802 Apr 2005.

[Bialkowski1996] Bialkowski SE, Sub-shot-noise light sources: A quiet revolution in light control, Critical Reviews In Analytical Chemistry 26 (2–3): 101-147 1996.

[Bogdanov2004] Bogdanov YI, Chekhova MV, Kulik SP, Maslennikov GA, Zhukov AA, Oh CH, Tey MK, Qutrit State Engineering with Biphotons, Physical Review Letters Vol 93 (230503), 1 December 2004.

[Bollinger1996] Bollinger, JJ; Itano, WM; Wineland, DJ; et al. Optimal frequency measurements with maximally correlated states PHYSICAL REVIEW A, 54 (6): R4649-R4652 DEC 1996.

[Booth2004] Booth MC, DiGiuseppe G, Saleh BEA, et al., Polarization-sensitive quantum-optical coherence tomography, Physical Review A, 69 (4): Art. No. 043815 Apr 2004.

[Boto2000] Boto AN, Kok P, Abrams DS, Williams CP, Braunstein SL, Dowling JP, Quantum interferometric optical lithography: Exploiting entanglement to beat the diffraction limit, Physical Review Letters, 85 (13): 2733–2736 Sep 25 2000.

[Bouwmeester2004] Bouwmeester D, Quantum physics — High N00N for photons, Nature, 429 (6988): 139 May 13 2004.

[Brink1993] Brink, DM; Satchler, GR; *Angular Momentum*, 3rd ed. (Clarendon Press, Oxford, UK, 1993).

[Campos2003] Campos, RA; Gerry, CC; Benmoussa, A Optical interferometry at the Heisenberg limit with twin Fock states and parity measurements PHYSICAL REVIEW A, 68 (2): Art. No. 023810 AUG 2003.

[Carmichael1993] Carmichael HJ, Quantum trajectory theory for cascaded open systems, Physical Review Letters 70 (15): 2273–2276 Apr 12 1993.

[Caves1981] Caves CM, Quantum-Mechanical Noise In An Interferometer, Physical Review D 23 (8): 1693–1708 1981.

[Chruvelli2008] Chiruvelli, A; Lee, H; Canonical Phase Measurements in the Presence of Photon Loss; (submitted to Phys. Rev. A) e-print: quant-ph/0811.2780 (2008).

[Chruvelli2009] Chiruvelli, A; Lee, H; Parity Measurement in Quantum Optical Metrology; (submitted to Phys. Rev. A) e-print: quant-ph/0901.4395 (2009).

[Dowling1991] Dowling JP, A Quantum State Of Ultra-Low Phase Noise, Optics Communications, 86 (2): 119–122 Nov 1 1991.

[Dowling1994] Dowling JP, Agarwal GS, Schleich WP, Wigner distribution of a general angular-momentum state — Applications to a collection of 2-level atoms, Physical Review A 49 (5): 4101–4109 Part B May 1994.

[Dowling1998] Dowling JP, Correlated input-port, matter-wave interferometer: Quantum-noise limits to the atom-laser gyroscope, Physical Review A, 57 (6): 4736–4746 Jun 1998.

[Dowling2008] Dowling, JP; Quantum optical metrology - the lowdown on high-N00N states; CONTEMPORARY PHYSICS, 49 (2): 125-143 2008.

[Durkin2007] Durkin, GA; Dowling, JP; Local and global distinguishability in quantum interferometry, PHYSICAL REVIEW LETTERS, 99 (7): Art. No. 070801 AUG 17 2007.

[Fischer1977] Fischer R, Kulevsky LA, Optical Parametric Light Oscillators (Review Article), Kvantovaya Elektronika 4 (2): 245–289 1977.

[Fitch2002] Fitch MJ, Franson JD, Dispersion cancellation and nonclassical noise reduction for large-photon-number states Physical Review A, 65 (5): Art. No. 053809 Part B May 2002.

[Franson1992] Franson JD, Nonlocal cancellation of dispersion, Physical Review A, 45 (5): 3126–3132 Mar 1 1992.

[Frehlich1996] Frehlich R, Coherent Doppler Lidar Measurements of Wings, in *Trends in Optics: Research, Developments, and Applications,* Anna Consortini, Ed., Academic Press, 1996.

[Gao2008] Gao, Y; Lee, H Sub-shot-noise quantum optical interferometry: a comparison of entangled state performance within a unified measurement scheme Journal Of Modern Optics, 55 (19-20): 3319-3327 2008.

[Gerry2000] Gerry, CC; Heisenberg-limit interferometry with four-wave mixers operating in a nonlinear regime; Physical Review A, 61 (4): Art. No. 043811 APR 2000.

[Gerry2001] Gerry, CC; Campos, RA; Generation of maximally entangled photonic states with a quantum-optical Fredkin gate; Physical Review A, 64 (6): Art. No. 063814 DEC 2001.

[Gerry2005] Gerry, CC; Knight, PL, *Introductory Quantum Optics;* (Cambridge University Press, Cambridge, UK, 2005).

[Gilbert2008a] Gilbert, G; Hamrick, M; Weinstein, YS; Use of maximally entangled N-photon states for practical quantum interferometry; Journal Of The Optical Society Of America B-Optical Physics, 25 (8): 1336-1340 AUG 2008.

[Gilbert2008b] Gilbert, G; Weinstein, YS; Aspects of practical remote quantum sensing, JOURNAL OF MODERN OPTICS, 55 (19-20): 3283-3291 2008.

[Gingrich2003] Gingrich RM, Kok P, Lee H, et al., All linear optical quantum memory based on quantum error correction, Physical Review Letters, 91 (21): Art. No. 217901 Nov 21 2003.

[Giovanetti2001a] Giovannetti V, Lloyd S, Maccone L, Quantum-enhanced positioning and clock synchronization Nature, 412 (6845): 417–419 Jul 26 2001.

[Giovanetti2002a] Giovannetti V, Lloyd S, Maccone L, Positioning and clock synchronization through entanglement, Physical Review A, 65 (2): Art. No. 022309 Feb 2002.

[Giovannetti2001b] Giovannetti V, Lloyd S, Maccone L, et al., Clock synchronization with dispersion cancellation, Physical Review Letters, 87 (11): Art. No. 117902 Sep 10 2001.

[Giovannetti2002b] Giovannetti V, Lloyd S, Maccone L, et al., Limits to clock synchronization induced by completely dephasing communication channels, Physical Review A, 65 (6): Art. No. 062319 Jun 2002.

[Giovannetti2004] Giovannetti V, Lloyd S, Maccone L, Quantum-enhanced measurements: Beating the standard quantum limit, Science, 306 (5700): 1330–1336 Nov 19 2004.

[Giovannetti2008] Giovannetti, V; et al.; Sub-Rayleigh Quantum Imaging; e-print arXiv:quant-ph/0804.2875v1, 2008.

[Hardy1998] Hardy, JW; *Adaptive Optics for Astronomical Telescopes*, Oxford University Press, 1998.

[Helstrom1976] Helstrom, CW; *Quantum Detection and Estimation*; Academic Press. New York, 2000.

[Higgens2007] Higgins, BL; Berry, DW; Bartlett, SD; et al.; Entanglement-free heisenberg-limited phase estimation; NATURE, 450 (7168): 393-U5 NOV 15 2007.

[Holland1993] Holland, MJ; Burnett, K; Interferometric Detection Of Optical-Phase Shifts At The Heisenberg Limit; Physical Review Letters, 71 (9): 1355-1358 AUG 30 1993.

[Hong1987] Hong CK, Ou ZY, Mandel L, Measurement of subpicosecond time intervals between 2 photons by interference, Physical Review Letters 59 (18): 2044–2046 Nov 2 1987.

[Huver2008] Huver, SD; Wildfeuer, CF; Dowling, JP; Entangled Fock states for robust quantum optical metrology, imaging, and sensing, Physical Review A 78, 063828 DEC 01 2008.

[Ip2003] Ip, P; Myers, TM; Noah, M; *PLEXUS Release 3.0, Version2.0 Phillips Laboratory Expert-assisted User Software User's Manual*, Air Force Research Laboratory, 2003.

[Jozsa2000] Jozsa R, Abrams DS, Dowling JP, Williams CP, Quantum clock synchronization based on shared prior entanglement, Physical Review Letters, 85 (9): 2010–2013 Aug 28 2000.

[Kapale2005] Kapale KT, Didomenico LD, Lee H, Kok P, Dowling JP, Quantum Interferometric Sensors, Concepts in Physics, 2: 225–240 (2005).

[Kawabe2007] Kawabe, Y; Fujiwara, H; Okamoto, R; et al.; Quantum interference fringes beating the diffraction limit; Optics Express, 15 (21): 14244-14250 OCT 17 2007.

[Khoury2006] Khoury, G; Eisenberg, HS; Fonseca, EJS; et al. Nonlinear interferometry via state-state projection; Physical Review Letters, 96 (20): Art. No. 203601 MAY 26 2006.

[Kim1998] Kim T, Pfister O, Holland MJ, et al., Influence of decorrelation on Heisenberg-limited interferometry with quantum correlated photons, Physical Review A 57 (5): 4004–4013 May 1998.

[Kingston1995] Kingston RH, *Optical Sources, Detectors and Systems: Fundamentals and Applications*, Academic Press, San Diego, 1995.

[Kok2000] Kok P, Boto AN, Abrams DS, Williams CP, Dowling JP, Quantum-interferometric optical lithography: Towards arbitrary two-dimensional patterns, Physical Review A 63 (6): Art. No. 063407 Jun 2001.

[Kok2002] Kok P, Lee H, Dowling JP, Creation of large-photon-number path entanglement conditioned on photodetection, Physical Review A 65 (5): Art. No. 052104 Part A May 2002.

[Kok2004] Kok P, Braunstein SL, Dowling JP, Quantum lithography, entanglement and Heisenberg-limited parameter estimation, Journal of Optics B — Quantum and Semiclassical Optics, 6 (8): S811–S815 Sp. Iss. SI Aug 2004.

[Kok2004] Kok, P; Braunstein, SL; Dowling, JP; Quantum lithography, entanglement and Heisenberg-limited parameter estimation; Journal Of Optics B-Quantum And Semiclassical Optics, 6 (8): S811-S815 Sp. Iss. SI AUG 2004.

[Kok2007] Kok, P; Munro, WJ; Nemoto, K; et al.; Linear optical quantum computing with photonic qubits, Reviews Of Modern Physics, 79 (1): 135-174 JAN-MAR 2007.

[Kolobov1999] Kolobov MI, The spatial behavior of nonclassical light, Reviews Of Modern Physics 71 (5): 1539–1589 Oct 1999.

[Kuzmich1998] Kuzmich A, Mandel L, Sub-shot-noise interferometric measurements with two-photon states, Quantum and Semiclassical Optics, 10 (3): 493–500 Jun 1998.

[Kwiat1993] Kwiat PG, Steinberg AM, Chiao RY, High-visibility interference in a bell-inequality experiment for energy and time, Physical Review A 47 (4): R2472–R2475 Part A Apr 1993.

[Kwiat1995] Kwiat PG, Mattle K, Weinfurter H, et al., New high-intensity source of polarization-entangled photon pairs, Physical Review Letters 75 (24): 4337–4341 Dec 11 1995.

[Lamas-Linares2001] Lamas-Linares A, Howell JC, Bouwmeester D, Stimulated emission of polarization-entangled photons, Nature, 412 (6850): 887–890 Aug 30 2001.

[LeeHW2002a] Lee H, Kok P, Cerf NJ, Dowling JP, Linear optics and projective measurements alone suffice to create large-photon-number path entanglement, Physical Review A 65 (3): Art. No. 030101 Part A Mar 2002.

[LeeHW2002b] Lee H, Kok P, Dowling JP, A quantum Rosetta stone for interferometry, Journal Of Modern Optics 49 (14–15): 2325–2338 Sp. Iss. Si Nov–Dec 2002.

[LeeHW2009] Lee, H; McCracken, SB; and Lee, TW; Heisenberg-limited optical interferometry: A density matrix formalism; (in preparation).

[LeeTW2004] Lee, TW; Hagness, SC; Pseudospectral time-domain methods for modeling optical wave propagation in second-order nonlinear materials; Journal Of The Optical Society Of America B-Optical Physics, 21 (2): 330-342 FEB 2004.

[LeeTW2001] Lee, TW; Hagness, SC; Zhou, DL; et al., Modal characteristics of Arrow-type vertical-cavity surface-emitting lasers, IEEE Photonics Technology Letters, 13 (8): 770-772 AUG 2001.

[Ley1987] Ley, M; Loudon, R; Quantum Theory Of High-Resolution Length Measurement With A Fabry-Perot-Interferometer; Journal Of Modern Optics, 34 (2): 227-255 FEB 1987.

[Li1999] Li YQ, Guzun D, Xiao M, Sub-shot-noise-limited optical heterodyne detection using an amplitude-squeezed local oscillator, Physical Review Letters 82 (26): 5225–5228 Jun 28 1999.

[Lidar1999] Lidar DA, Bacon D, Whaley KB, Concatenating decoherence-free subspaces with quantum error correcting codes, Physical Review Letters 82 (22): 4556-4559 May 31 1999.

[Lita2008] Lita, AE; Miller, AJ; Nam, SW Counting near-infrared single-photons with 95% efficiency OPTICS EXPRESS, 16 (5): 3032-3040 MAR 3 2008.

[Liu2008] Liu, BH; Sun, FW; Gong, YX; et al.; Demonstration of the three-photon de Broglie wavelength by projection measurement; Physical Review A, 77 (2): Art. No. 023815 FEB 2008.

[Loudon2000] Loudon, R; *The Quantum Theory of Light;* Oxford University Press, Oxford, UK, 2000.

[Mitchell2004] Mitchell, MW; Lundeen, JS; Steinberg, AM; Super-resolving phase measurements with a multiphoton entangled state; NATURE, 429 (6988): 161-164 MAY 13 2004.

[Nagasako2001] Nagasako EM, Bentley SJ, Boyd RW, Agarwal GS, Nonclassical two-photon interferometry and lithography with high-gain parametric amplifiers, Physical Review A 64, 043802 (2001).

[Nagata2007] Nagata, T; Okamoto, R; O'Brien, JL; et al.; Beating the standard quantum limit with four-entangled photons; Science, 316 (5825): 726-729 MAY 4 2007.

[Nasr2004] Nasr MB, Saleh BEA, Sergienko AV, et al., Dispersion-cancelled and dispersion-sensitive quantum optical coherence tomography, Optics Express, 12 (7): 1353–1362 Apr 5 2004.

[Okamoto2008] Okamoto, R; Hofmann, HF; Nagata, T; et al.; Beating the standard quantum limit: phase super-sensitivity of N-photon interferometers; New Journal Of Physics, 10: Art. No. 073033 JUL 18 2008.

[Pe'er2004] Pe'er A, Dayan B, Vucelja M, Silberberg Y, Friesem A, Quantum lithography by coherent control of classical light pulses, Optics Express Vol. 12 No. 26, 27 December 2004

[Pezze2006] Pezze, L; Smerzi, A Phase sensitivity of a Mach-Zehnder interferometer Physical Review A, 73 (1): Art. No. 011801 JAN 2006.

[Ralph2000] Ralph TC, Can signal-to-noise be improved by heterodyne detection using an amplitude squeezed local oscillator? Physical Review Letters 85 : 677 2000.

[RCA1974] *Electro-Optics Handbook*, Radio Corporation of America, 1974

[Resch2001] Resch KJ, Lundeen JS, Steinberg AM, Nonlinear optics with less than one photon, Physical Review Letters 87 (12): Art. No. 123603 Sep 17 2001.

[Resch2003] Resch KJ, Lundeen JS, Steinberg AM, Practical creation and detection of polarization Bell states using parametric downconversion, The Physics of Communication, Proceedings of the XXII Solvay Conference on Physics, Antoniou, Sadovnichy, and Walther eds., World Scientific (2003), pp 437–451.

[Resch2007] Resch, KJ; Pregnell, KL; Prevedel, R; et al.; Time-reversal and super-resolving phase measurements; PHYSICAL REVIEW LETTERS, 99 (6): Art. No. 069902 AUG 10 2007.

[Rubin2006] Rubin MA, Kaushik S, Squeezing the local oscillator does not improve signal-to-noise ratio in heterodyne laser radar, quant-ph/0610230.

[Rubin2007a] Rubin MA, Kaushik S, Notes on Signal-to-Noise Ratio in Squeezed-Light Laser Radar, quant-ph/0701245.

[Rubin2007b] Rubin, MA; Kaushik, S; Loss-induced limits to phase measurement precision with maximally entangled states; PHYSICAL REVIEW A, 75 (5): Art. No. 053805 MAY 2007.

[Sanders1995] Sanders, BC; Milburn, GJ; Optimal Quantum Measurements For Phase Estimation; Physical Review Letters, 75 (16): 2944-2947 OCT 16 1995.

[Santori2002] Santori C, Fattal D, Vuckovic J, Solomon GS, Yamamoto Y, Indistinguishable photons from a single-photon device, Nature Vol 419: 594–597, 10 October 2002.

[Schleich1991] Schleich WP, Dowling JP, Horowicz RJ, Exponential decrease in phase uncertainty, Physical Review A, 44 (5): 3365–3368 Sep 1 1991.

[Schmitt1996] Schmitt, M., McVey, B, Cooke, B., Busch, G.; Comprehensive System Model for CO_2 DIAL; *Proceedings of SPIE,* **2702**, 95, 1996.

[Sciarrino2008] Sciarrino, F; Vitelli, C; De Martini, F; et al., Experimental sub-Rayleigh resolution by an unseeded high-gain optical parametric amplifier for quantum lithography, Physical Review A, 77 (1): Art. No. 012324 JAN 2008.

[Scully1993] Scully MO, Dowling JP, Quantum-noise limits to matter-wave interferometry, Physical Review A, 48 (4): 3186–3190 Oct 1993.

[Scully1997] Scully. MO; Zubairy, MS; *Quantum Optics;* Cambridge University Press, Cambridge, UK, 1997.

[Shapiro1993] Shapiro, JH; Phase Conjugate Quantum Communication with Zero Error Probability at Finite Average Photon Number; Phys. Scripta, T48, 105–112, 1993.

[Shapiro1995] Shapiro, JH; Phase Conjugate Quantum Communication with Optical Heterodyne Detection, Opt. Lett., 20, 1059–1061, 1995.

[Sharma1996] Sharma, RD; et al.; *User's Manual for SAMM, SHARC and MODTRAN Merged*, PL-TR-96-2090, ERP, No. 1190, Philips Laboratory/GPOS, 1996.

[Simon2003] Simon C, Bouwmeester D, Theory of an entanglement laser, Physical Review Letters, 91 (5): Art. No. 053601 Aug 1 2003.

[Spedalieri2006] Spedalieri FM, Lee H, Dowling JP, High-fidelity linear optical quantum computing with polarization encoding, Physical Review A, 73 (1): Art. No. 012334 Jan 2006.

[Steinberg1992a] Steinberg AM, Kwiat PG, Chiao RY, Dispersion cancellation in a measurement of the single-photon propagation velocity in glass, Physical Review Letters 68 (16): 2421–2424 Apr 20 1992.

[Steinberg1992b] Steinberg AM, Kwiat PG, Chiao RY, Dispersion cancellation and high-resolution time measurements in a 4th-order optical interferometer, Physical Review A 45 (9): 6659–6665 May 1 1992.

[Steinberg1993] Steinberg AM, Kwiat PG, Chiao RY, Measurement of the single-photon tunneling time, Physical Review Letters 71 (5): 708–711 Aug 2 1993.

[Strekalov2002] Strekalov DV, Dowling JP, Two-photon interferometry for high-resolution imaging, Journal of Modern Optics, 49 (3–4): 519–527 Mar 10 2002.

[Sun2006] Sun, FW; Liu, BH; Huang, YF; et al.; Observation of the four-photon de Broglie wavelength by state-projection measurement; Physical Review A, 74 (3): Art. No. 033812 SEP 2006.

[Suzuki2006] Suzuki S, Yonezawa H, Kannari F, et al., 7 dB quadrature squeezing at 860 nm with periodically poled KTiOPO4, Applied Physics Letters 89 (6): Art. No. 061116 Aug 7 2006.

[Toussaint2004] Toussaint KC, DiGiuseppe G, Bycenski KJ, et al., Quantum ellipsometry using correlated-photon beams, Physical Review A, 70 (2): Art. No. 023801 Aug 2004.

[Tsang2009] Tsang M, Quantum imaging beyond the diffraction limit by optical centriod measurements," arXiv:0901.4817 (2009).

[Uys2007] Uys H, Meystre P, Quantum states for Heisenberg limited interferometry, quant-ph/0702170.

[Valencia2004] Valencia A, Scarcelli G, Shih YH, Distant clock synchronization using entangled photon pairs, Applied Physics Letters 85 (13): 2655–2657 Sep 27 2004.

[VanMeter2007] VanMeter, NM; Lougovski, P; Uskov, DB; et al. General linear-optical quantum state generation scheme: Applications to maximally path-entangled states Physical Review A, 76 (6): Art. No. 063808 DEC 2007.

[Walther2004] Walther, P; Pan, JW; Aspelmeyer, M; et al.; De Broglie wavelength of a non-local four-photon state, Nature, 429 (6988): 158-161 MAY 13 2004.

[Wildfeuer2007] Wildfeuer, CF; Lund, AP; Dowling, JP Strong violations of Bell-type inequalities for path-entangled number states; Physical Review A, 76 (5): Art. No. 052101 NOV 2007.

[Wildfuer2009] Wildfeuer, CF; Pearlman, AJ; Chen, J; Fan, JY; Migdall, A; Dowling JP; Interferometry with a photon number resolving detector; SPIE, Presented at Photonics West, San Jose, CA, 24–29 January 2009.

[Wu2007] Wu Z, VanMeterNM, Lougovski P, Uskov DB, Lee H, Dowling JP, Genetic Algorithm Approach to Quantum State Design, arXiv:0708.1498, 2007.

[Yuen1986] Yuen, HP; Generation, Detection, And Application Of High-Intensity Photon-Number-Eigenstate Fields; Physical Review Letters, 56 (20): 2176-2179 MAY 19 1986.

[Yurke1986] Yurke, B; McCall, SL; Klauder, JR; SU(2) And SU(1,1) Interferometers Physical Review A, 33 (6): 4033-4054 JUN 1986.

[Yurtsever2002] Yurtsever U, Dowling JP, Lorentz-invariant look at quantum clock-synchronization protocols based on distributed entanglement, Physical Review A, 65 (5): Art. No. 052317 Part A May 2002.

[Yurtsever2003] Yurtsever U, Strekalov D, Dowling JP, Interferometry with entangled atoms, European Physical Journal D, 22 (3): 365–371 Mar 2003

9.0 ACRONYMS/GLOSSARY

AESOP	Airborne Electro-optical Special Operation Payload
AMCOM	Aviation and Missile Command
CCT	Center for Computation and Technology
CONOPS	Control Operations
CSP	Common Sensor Platform
DARPA	Defense Advanced Research Projects Agency
DII	Director's Innovation Initiative
DoD	Department of Defense
ECE	Electrical and Computer Engineering
EO/IR	Electro-Optical/Infra-Red
EPL	entangled photon laser
FFT	fast Fourier transforms
FOV	field of view
FPI	Fabry-Pérot interferometer
HELLFIRE	Heliborne Laser Fire & Forget Missile System
HITP	Hearne Institute for Theoretical Physics
HL	Heisenberg limit
JPL	Jet Propulsion Laboratory
LIDAR	Light Detection and Ranging
LIGO	Laser Interferometer Gravitational wave Observatory
LONI	Louisiana Optical Network Initiative
LSU	Louisiana State University
MATLAB	Matrix Laboratory
MSA	MathSense Analytics
MODTRAN	MODerate resolution atmospheric TRANsmission
NASA	National Aeronautics and Space Administration
NATO	North Atlantic Treaty Organization
NIST	National Institute of Standards and Technology
NRD	number-resolving detections
NRO	National Reconnaissance Office
OPA	optical parametric amplifier
OPO	optical parametric oscillator
P&A	Physics and Astronomy
PLEXUS	Phillips Laboratory EXpert-assisted User Software
QuLidar	Quantum Light Detection and Ranging
QSP	Quantum Sensors Program
QST	Quantum Science and Technologies
RAM	random-access memory
RF	Radio Frequency
RHEL	Red Hat Enterprise Linux
SAMM	SHARC And MODTRAN Merged
SAS	Space and Airborne Systems
SHARC	Super Harvard Architecture Single-chip Computer

SNL	shot-noise limit
SNR	Signal to Noise Ratio
SOW	Statement of Work
SPDC	spontaneous parametric down conversion
TES	transition edge sensor
UAV	Unmanned Airborne Vichecle
VLPC	visible light photon counter

APPENDIX: REPRINTS AND PREPRINTS

Following papers produced as deliverables for this grant:

[Cable2009] Cable, H; Vyas, R; Singh, S; Dowling, JP; Theoretical investigation of a non-degenerate optical parametric oscillator as a high-flux source for quantum lithography, in preparation (to be submitted to Physical Review).

[Chiruvell2008] Chiruvelli, A; Lee, H; Parity Measurements in Quantum Optical Metrology; arXiv:0901.4395 (to be submitted to Physical Review).

[Chiruvell2009] Chiruvelli, A; Lee, H; Canonical Phase Measurements in the Presence of Photon Loss; arXiv:0811.2780 (to be submitted to Physical Review).

[Dowling2008] Dowling, JP; Quantum optical metrology — the lowdown on high-N00N states; CONTEMPORARY PHYSICS, 49 (2): 125-143 2008.

[Gao2008] Gao, Y; Lee, H; Sub-shot-noise quantum optical interferometry: a comparison of entangled state performance within a unified measurement scheme; JOURNAL OF MODERN OPTICS, 55 (19-20): 3319-3327 2008.

[Gao2009] Gao, Y; Wildfeuer, CF; Lee, H; Dowling, JP; Super-Resolution at the Shot-Noise Limit with Coherent States and Photon-Number-Resolving Detectors, in preparation (to be submitted to Physical Review).

[Glasser2008] Glasser, RT; Cable, H; Dowling, JP; Entanglement-seeded, dual, optical parametric amplification: Applications to quantum imaging and metrology; PHYSICAL REVIEW A, 78 (1): Art. No. 012339 JUL 2008.

[Huver2008] Huver, SD; Wildfeuer, CF; Dowling, JP; Entangled Fock states for robust quantum optical metrology, imaging, and sensing; PHYSICAL REVIEW A, 78 (6): Art. No. 063828 Part B DEC 2008.

[LeeTW2009] Lee, TW; Huver, SD; Lee, H; Kaplan, L; McCracken, SB; Min, C; Uskov, D; Wildfeuer, CF; Veronis, G; Dowling JP; Optimization of quantum interferometric metrological sensors in the presence of photon loss, in preparation (to be submitted to Physical Review).

[Sciarrino2008] Sciarrino, F; Vitelli, C; De Martini, F; et al., Experimental sub-Rayleigh resolution by an unseeded high-gain optical parametric amplifier for quantum lithography, PHYSICAL REVIEW A, 77 (1): Art. No. 012324 JAN 2008.